THREE DIMENSIONAL (3D) PRINTING OF BIO-POLYMERS FROM AGRICULTURAL WASTES

A THESIS SUBMITTED TO
THE GRADUATE SCHOOL OF NATURAL AND APPLIED SCIENCES
OF
MIDDLE EAST TECHNICAL UNIVERSITY

BY

EYLÜL GÖKÇE BAHÇEGÜL

IN PARTIAL FULFILLMENT OF THE REQUIREMENTS
FOR
THE DEGREE OF DOCTOR OF PHILOSOPHY
IN
POLYMER SCIENCE AND TECHNOLOGY

AUGUST 2022

Approval of the thesis:

THREE DIMENSIONAL (3D) PRINTING OF BIO-POLYMERS FROM AGRICULTURAL WASTES

submitted by **EYLÜL GÖKÇE BAHÇEGÜL** in partial fulfillment of the requirements for the degree of **Doctor of Philosophy** i**n Polymer Science and Technology, Middle East Technical University** by,

Prof. Dr. Halil Kalıpçılar
Dean, Graduate School of **Natural and Applied Sciences** _____

Prof. Dr. Necati Özkan
Head of the Department, **Polymer Science and Technology** _____

Prof. Dr. Necati Özkan
Supervisor, **Polymer Science and Technology, METU** _____

Asst. Prof. Dr. Cemal Merih Şengönül
Co-Supervisor, **Manufacturing Engineering, Atılım University** _____

Examining Committee Members:

Prof. Dr. Cevdet Kaynak
Metallurgical and Materials Engineering, METU _____

Prof. Dr. Necati Özkan
Polymer Science and Technology, METU _____

Prof. Dr. Göknur Bayram
Chemical Engineering, METU _____

Prof. Dr. Eda Ayşe Aksoy
Basic Pharmaceutical Sciences, Hacettepe University _____

Prof. Dr. Pınar Yılgör Huri
Biomedical Engineering, Ankara University _____

Date: 08.08.2022

I hereby declare that all information in this document has been obtained and presented in accordance with academic rules and ethical conduct. I also declare that, as required by these rules and conduct, I have fully cited and referenced all material and results that are not original to this work.

Name Last name : Eylül Gökçe Bahçegül

Signature:

ABSTRACT

THREE DIMENSIONAL (3D) PRINTING OF BIO-POLYMERS FROM AGRICULTURAL WASTES

Bahçegül, Eylül Gökçe
Doctor of Philosophy, Polymer Science and Technology
Supervisor : Prof. Dr. Necati Özkan
Co-Supervisor: Asst. Prof. Dr. Cemal Merih Şengönül

August 2022, 183 pages

Lignocellulosic biomass, which is a composite structure made up of cellulose, hemicellulose and lignin biopolymers, is the most abundant biopolymer resource on earth. Among the biopolymers found in lignocellulosic agricultural wastes, hemicellulose and lignin receive significantly less attention compared to cellulose for material applications despite the fact that these two biopolymers constitute almost a half of a given biomass. In this context, three novel strategies were developed that render hemicellulose and lignin 3D printable. Corn cobs (CCs) were used as the lignocellulosic resource in which hemicellulosic pastes and CC extracts in the form of thermoreversible cold-setting gels with different formulations were obtained following different extraction approaches and parameters. Water and NaOH contents as well as the extraction parameters such as KOH concentration coupled to the correct 3D printing parameters including printing temperature and speed, extrusion multiplier and layer height was the key to render the pastes and extracts 3D printable. Hemicelluloses containing lignin were rendered 3D printable for the first time without any chemical modifications and without using auxiliary polymers or additives by determining the very narrow process window that enables 3D printability. A blending strategy that relies on thermoplasticity, which involves mixing hemicellulose and lignin with polyvinyl alcohol via solvent casting, was also

developed in order to obtain filaments for 3D printing, which allow for the 3D printing of more complex shapes. Thermal, mechanical, chemical, complex and apparent viscosities, morphological and printability properties of the polymers and the 3D printed materials were characterized by different methods.

Keywords: 3D printing, hemicellulose, lignin, lignocellulosic biomass, xylan

ÖZ

TARIMSAL ATIKLARDAN ELDE EDİLEN BİYOPOLİMERLERİN ÜÇ BOYUTLU (3B) BASKISI

Bahçegül, Eylül Gökçe
Doktora, Polimer Bilim ve Teknolojisi
Tez Yöneticisi: Prof. Dr. Necati Özkan
Ortak Tez Yöneticisi: Dr. Öğr. Üyesi Cemal Merih Şengönül

Ağustos 2022, 183 sayfa

Selüloz, hemiselüloz ve ligninden oluşan kompozit bir yapı olan lignoselülozik biyokütle dünyadaki en bol bulunan biyopolimer kaynaklarından bir tanesidir. Lignoselülozik tarımsal atıklarda bulunan biyopolimerler arasında, hemiselüloz ve lignin, biyokütlenin neredeyse yarısını oluşturmasına rağmen, malzeme uygulamaları için selüloza kıyasla daha az ilgi görmektedir. Bu kapsamda, hemiselüloz ve ligninin 3B baskı teknolojilerinde baskı malzemesi olarak kullanımını sağlayacak üç yeni strateji geliştirilmiştir. Farklı formülasyonlara sahip hemiselülozik pastalar ve jel formundaki mısır koçanı özütleri farklı özütleme yaklaşımları ve parametreleri denenerek ve lignoselülozik biyokütle kaynağı olarak mısır koçanlarının kullanılması ile elde edilmiştir. KOH konsantrasyonu gibi özütleme parametrelerinin yanı sıra su ve NaOH içerikleri ile birlikte baskı sıcaklığı ve hızı, ekstrüzyon çarpanı ve katman yüksekliği gibi doğru 3B baskı parametrelerinin uygulanması hemiselüloz ve lignin temelli pasta ve özütlerin 3B yazdırılmasıda önemli rol oynamaktadır. Lignin içeren hemiselülozlar, malzemenin 3B yazdırılabilir olduğu dar bir işlem penceresi belirlenerek, herhangi bir kimyasal değişiklik yapılmadan ve yardımcı polimerler veya katkı maddeleri kullanılmadan ilk kez 3B yazdırılabilir hale getirilmiştir. Ayrıca, hemiselüloz ve ligninin çözücü

döküm yöntemiyle PVA ile karıştırılmasını içeren bir harmanlama stratejisi, daha karmaşık şekillerin 3B yazıcı ile üretilmesini sağlayan filament formunda baskı malzemelerini elde etmek amacıyla geliştirilmiştir. Çalışma kapsamında polimerlerin ve polimerden 3B baskı ile elde edilen malzemelerin ısısal, mekanik, kimyasal, reolojik, morfolojik ve yazdırılabilirlik özellikleri karakterize edilmiştir.

Anahtar Kelimeler: 3B baskı, hemiselüloz, lignin, lignoselülozik biyokütle, ksilan

Anneme, babama ve kardeşime

ACKNOWLEDGMENTS

I would like to thank my supervisor Prof. Dr. Necati Özkan for his valuable contributions and for his continuous support throughout my studies.

I also would like to thank my co-supervisor Asst. Prof. Dr. Cemal Merih Şengönül and to my thesis progress committee members, Prof. Dr. Cevdet Kaynak and Prof. Dr. Eda Ayşe Aksoy for their valuable comments and suggestions related to my work.

I acknowledge the technical assistance provided by Ali Güzel from METU Central Laboratory related to tensile testing measurements and by Burak Yurdakul related to the 3D printer. 3D4E is acknowledged for their contributions related to the design and manufacturing of the 3D printer used in the study. I would also like to thank Burcu Sarı for her friendship and support throughout my studies. METU Central Laboratory staff is acknowledged for the support they have provided during the characterization of materials.

Finally, I would like to thank my parents and my sister for their patience and for their endless support.

TABLE OF CONTENTS

ABSTRACT v
ÖZ vii
ACKNOWLEDGMENTS x
TABLE OF CONTENTS xi
LIST OF TABLES xiv
LIST OF FIGURES xv
LIST OF ABBREVIATIONS xxi
LIST OF SYMBOLS xxiii
CHAPTERS
1 INTRODUCTION 1
1.1 Lignocellulosic biomass 1
1.1.1 Cellulose 2
1.1.2 Hemicellulose 2
1.1.3 Lignin 4
1.2 3D printing 4
1.2.1 3D printing process steps 5
1.2.2 Printing materials 6
1.2.3 3D printing technologies used for biomass and biomass derived materials 8
1.3 Objective of the study 13
2 LITERATURE REVIEW 15
2.1 3D printing of hemicellulose 15
2.2 3D printing of lignin 18
2.3 3D printing of entire lignocellulosic biomass with all of its components 27
3 MATERIALS AND METHODS 35
3.1 Materials 35
3.2 Biopolymer extraction from CCs 35
3.3 Preparation of hemicellulosic pastes 36

3.4 Preparation of CC gel extracts 36
3.5 Preparation of blends containing hemicellulosic pastes or CC extracts together with PVA 37
3.6 Desalting the hemicellulosic paste 38
3.7 Filament fabrication from blends containing hemicellulosic pastes and CC extracts together with PVA 39
3.8 3D printing of hemicellulosic pastes, CC extracts and filaments containing PVA 39
3.9 Rheological characterizations 42
3.10 Determination of mechanical properties 42
3.11 Water content determination 43
3.12 Scanning electron microscopy (SEM) 43
3.13 Fourier-transform infrared spectroscopy (FT-IR) 44
3.14 Thermo gravimetric analysis (TGA) 44
3.15 Determination of PVA molecular weight 44
3.16 Determination of hydrolysis degree of PVA 46
4 3D PRINTING OF HEMICELLULOSIC PASTES 49
4.1 Preliminary studies on the general factors influencing the 3D printability of extracted hemicellulosic biopolymers 49
4.2 Viscosity studies of the hemicellulosic pastes 58
4.3 Effect of water content and process parameters on 3D printability of hemicellulosic pastes 64
4.4 3D printing of a scaffold prototype 75
4.5 The mechanical properties of 3D printed models from hemicellulosic pastes 81
4.6 SEM analysis of the 3D printed models from hemicellulosic pastes 82
5 3D PRINTING OF CC EXTRACTS CONTAINING HEMICELLULOSE AND LIGNIN 85
5.1 Preliminary studies on the general factors influencing the 3D printability of CC extracts containing hemicellulose and lignin 86

5.2 Effect of 3D printing parameters and water content on 3D printability of CC extracts 96
5.3 Effect of performing the alkaline extraction with lower KOH concentration on the 3D printability of CC extracts 100
5.4 Chemical and thermogravimetric properties related to CC extracts in comparison with the hemicellulosic pastes 103
5.5 Mechanical properties of the CC extract 113
5.6 Rheological properties of CC extracts 113
5.7 SEM analysis of the 3D printed models from CC extract 117
6 3D PRINTING OF FILAMENTS OBTAINED FROM HEMICELLULOSIC PASTES AND CC EXTRACTS TOGETHER WITH PVA 121
6.1 Preparation of blends containing hemicellulosic pastes and CC extracts together with PVA 122
6.2 Fabrication of filaments used in 3D printing 126
6.2.1 Viscosities of samples used for filament fabrication 131
6.3 3D printing of filaments 133
6.4 Mechanical properties of 3D printed and solvent cast dog bone shaped samples with different water contents 142
6.5 Thermogravimetric analysis of filaments with different formulations . 153
7 CONCLUSIONS 157
8 FUTURE STUDIES 163
REFERENCES 165
APPENDICES
A. Mechanical properties of 3D printed HP/PVA, d-HP/PVA and CC extract/PVA blends 179
B. 1st derivative weight graphs for filaments with different formulations 181
CURRICULUM VITAE 183

LIST OF TABLES

TABLES

Table 3.1 Results of measurements made for the calculation of PVA molecular weight. 45
Table 3.2 Molecular weight calculated from the corresponding Mark-Houwink constants. 46
Table 4.1 Printability, cell area and % target area values for models printed at different EMs and printing speeds at 80°C. 74
Table 4.2 Mechanical property data including TS, %eb, and E for materials obtained from CC hemicellulosic polymers by different polymer processing techniques. 81
Table 5.1 The values of k′, n′ and η* at 10 rad/s for the samples with a water content of 68% and 83% at various temperatures ranging from 35°C to 55°C. 114
Table 6.1 Diameters of filaments fabricated from different blends. 131
Table 6.2 3D printing parameters of the paste and the extract containing filaments. 133
Table 6.3 Moisture uptake values of different filaments conditioned at a RH of 37 ± 3% at 22°C for 14 days. 137
Table 6.4 Printability values calculated from the gird models 3D printed from different blends. 139
Table 6.5 Mechanical properties of 3D printed, and solvent cast dog bone shaped specimens obtained following the conditioning of the samples at a RH of 47 ± 3%. 148
Table 6.6 Mechanical properties of 3D printed, and solvent cast dog bone shaped specimens obtained following the conditioning of the samples at a RH of 15 ± 1%. 150
Table 6.7 Mechanical properties of 3D printed, and solvent cast dog bone shaped specimens obtained following the conditioning of the samples at in the oven at 40°C. 152

LIST OF FIGURES

FIGURES

Figure 3.1 Chopped PVA filament (A) and storage container used for blend films, filaments and printed 3D models (B). 37
Figure 3.2 Appearance of the 3D printer with the standard extruder head attached for filament printing (A). Standard extruder head in more detail (B). Appearance of the 3D printer with the syringe printing head attached for paste and gel printing (C). Polypropylene (D) and stainless-steel syringes with to different inner diameters (E) that can fit into the barrel of the syringe printing head. 40
Figure 3.3 Data points obtained from Huggins and Kraemer equations for determining the intrinsic viscosity of PVA. 45
Figure 4.1 Print-preview and the first layer of the 3D printed model obtained during the one of the first preliminary experiments with the hemicellulosic paste. 51
Figure 4.2 Print-preview and the model printed right after and after 24 hours of the printing process. 52
Figure 4.3 Print-preview and the actual printing process of 40 x 30 x 10 mm rectangular model. 53
Figure 4.4 Printed grids of two crossing layers with seven different printing speeds. Images taken right after the printing process. 54
Figure 4.5 Printed grids of two crossing layers with 5 different printing speeds. Top to bottom: hemicellulose + 6 ml DI water, hemicellulose + 6 ml 1 wt.% NaOH solution, hemicellulose + 6 ml 2.5 wt.% NaOH solution, hemicellulose + 6 ml 3 wt.% NaOH solution and hemicellulose + 6 ml 5 wt.% NaOH solution. Images taken right after the 3D printing process (pastes contain 75-80% water content). 56
Figure 4.6 Parallel plate measurements of hemicellulosic pastes (A) with NaOH addition and (B) without NaOH addition at different water contents. 59
Figure 4.7 K value as a function of water content for the hemicellulosic paste+DI water, hemicellulosic paste+2.5 wt.% NaOH solution and hemicellulosic paste+5 wt. % NaOH solution. 61

Figure 4.8 Effect of temperature on viscosity of the hemicellulosic paste containing 1 wt.% NaOH solution. 62
Figure 4.9 Influence of water content on the apparent viscosity of hemicellulosic pastes at 60°C and influence of temperature on the apparent viscosity of hemicellulosic pastes with a water content of 57%. 63
Figure 4.10 3D printing of hemicellulosic paste with 62% water content at different temperatures. 65
Figure 4.11 3D printing of hemicellulosic paste with 65% water content. 66
Figure 4.12 3D printing of hemicellulosic paste with 68% water content. 66
Figure 4.13 Hemicellulosic pastes with a water content of 62% printed at 80°C at five different EM values. 68
Figure 4.14 Appearance of three-layered models printed from hemicellulosic pastes with a water content of 65% (A) and 68% (B) at 80°C by using five different EM values between 1.0–2.0. 69
Figure 4.15 3D printing of hemicellulosic paste at 90°C. 70
Figure 4.16 Appearance of three-layered grid structure upon drying. 70
Figure 4.17 A hollow cube printed from hemicellulosic paste and its appearance upon drying. 71
Figure 4.18 A hollow cube printed from hemicellulosic paste and its appearance upon drying. Appearance of the hollow cube right after the printing process while it was wet (top row) and after drying at ambient conditions for 24 h (bottom row). . 72
Figure 4.19 A 3D daisy figure printed from hemicellulosic paste. 73
Figure 4.20 3D printing of three-layered scaffold prototypes with intended dimensions of 15 mm x 15 mm x 2.43 mm from hemicellulosic paste with 62% water content. Scaffold prototypes printed at (A) three different printing speeds with an EM value of 1.25, (B) two different EM values at 100 mm/min printing speed (C) Top print preview of designed scaffold prototype. 76
Figure 4.21 Three-layered scaffold prototypes printed at (A) 300 mm/min and (B) 100 mm/min printing speed in 1.0-1.5 EM value ranges. 77

Figure 4.22 Three-layered scaffold prototype printed at 300 mm/min and a layer height of 0.81 mm. Printing with (A) 1.0 and (B) 1.1 EM values. Appearance of scaffold prototype upon drying (C). 78
Figure 4.23 Three-layered scaffold prototype printed with five different layer heights (LH) at 300 mm/min printing speed and 60°C. 79
Figure 4.24 (A) Top print preview of designed three-layered scaffold prototype. (B) Appearance of 3D printed three-layered scaffold prototype right after the printing process and after drying at ambient conditions for 24 h (C) Print preview of designed ten-layered scaffold prototype. (D) Appearance of 3D printed ten-layered scaffold prototype after drying at ambient conditions for 24 h. 80
Figure 4.25 (A) Cross-section SEM images of a dog bone shaped model and (B) cross-section, (C) surface SEM images of the dried grid model printed from the hemicellulosic paste at two different magnifications. 83
Figure 5.1 Trials to print 40 x 40 mm three- layered grid structure printed with (A) 200 mm/min, 0.68 mm layer height (B) 200 mm/min, 0.54 mm layer height. 87
Figure 5.2 3D models printed from wheat bran extracts by the addition of the solvent after printing (A) and simultaneously during printing (B). 88
Figure 5.3 Appearance of grid models from partially concentrated CC extracts printed at room temperature at different EM values. 90
Figure 5.4 Appearance of 40 x 40 mm three-layered grid structure printed with nozzle tip with 1.23 mm inner diameter (A) as printed (B) after washing with acetic acid-ethanol solution (C) after washing only with ethanol. 91
Figure 5.5 Six layered grid models printed from partially concentrated CC extracts washed by different antisolvents. 92
Figure 5.6 Effect of different antisolvent formulations the appearance of grid models printed from CC extract. Models were immersed in antisolvent baths prepared with (A) ethanol (B) 5% acetic acid - ethanol solution (C) 10% acetic acid-ethanol solution. 94
Figure 5.7 Appearance of the 4 x4 cm grid model printed from the gel extract at 50°C following the addition of ethanol as the antisolvent. 95

Figure 5.8 Four-layered 2 x 2 cm models printed with CC gel extract with (A) 76.82% water content in the temperature range of 50-65°C and 0.68 mm nozzle tip (B) 79.18 % water content in the temperature range of 45-55°C and 0.54 mm nozzle tip. (C) Appearance of the models printed at 50 and 55°C after being removed from the build platform following ethanol washing. 97
Figure 5.9 Four-layered 32 x 32 models printed from CC extract with (A) 76% (B) 83% and (C) 86 % water contents at different temperatures. 99
Figure 5.10 A four-layered 20 x 20 mm model printed from the CC extract obtained following the extraction with 3% KOH solution printed with an EM of 1.2 (A) and 1.5 (B) The appearance of the model after immersion into the ethanol bath is given in (C). 101
Figure 5.11 Appearance of the gel obtained from the alkaline extracts of CC. 102
Figure 5.12 IR spectrum of CCs before and after alkaline extraction. 105
Figure 5.13 IR spectrum of reference xylan from birchwood, hemicellulosic paste and gel extract. 107
Figure 5.14 IR spectrum of KAc. 107
Figure 5.15 Weight loss curves for cellulose, hemicellulose and lignin obtained by TGA. 109
Figure 5.16 Weight loss curves for CC before and after alkaline extraction obtained by TGA. 111
Figure 5.17 Weight loss curves for gel extracts and hemicellulosic paste obtained by TGA. 112
Figure 5.18 (A) Complex viscosity against frequency for the CC extract gel samples containing 68% and 83% water at various temperatures ranging from 35°C to 55°C. Solid symbols represents the results for 68% water content and open symbols represents results for 83% water content. (B) Complex viscosity at 10 rad/s against temperature for the gel samples containing 68% and 83% water. 115
Figure 5.19 tan δ versus frequency for the CC extract gel samples at various temperatures containing (A) 68% water and (B) 83% water. 116

Figure 5.20 Appearance of the wet and dry models 3D printed from the CC gel extract with a water content of 83% at four different printing temperatures. 118
Figure 6.1 HP/PVA films with 15% (A), 25% (B) and 40% (C) HP concentrations. 123
Figure 6.2 CC extract/PVA films with 25% (A) and 40% (B) extract concentration. 124
Figure 6.3 Appearance of dry 25% d-HP/PVA, 40% d-HP/PVA and 40% HP/PVA films. 125
Figure 6.4 Films obtained from low viscosity (A) and high viscosity (B) d-HP/PVA solutions containing 40% d-HP..... 126
Figure 6.5 Appearance of HP/PVA filaments with 15% (A), 25% (B) and 40% (C) HP concentrations. 127
Figure 6.6 Appearance of 40% HP/PVA filament (A), defects and bulbous structures on the filament surface (B), voids inside the filament (C). 25% d-HP/PVA filament (D), 25% CC extract/PVA filament (E), 40% CC extract/PVA filament (F). 128
Figure 6.7 Appearance of filaments containing HP and CC extract fabricated with a drying step performed at 170°C for 20 minutes prior to processing with the capillary rheometer. 130
Figure 6.8 Apparent viscosity at a shear rate of 10 s-1 against water content for PVA and HP/PVA filament materials..... 132
Figure 6.9 Five layered grid models printed from different HP/PVA and d-HP/PVA filaments..... 134
Figure 6.10 Inside view of the 3D printer's extruder head that shows a broken filament in contact with the gear that forces the filament into the hot end up to the nozzle. 135
Figure 6.11 Water contents of different filaments with respect to time as they were conditioned at a RH of 37 ± 3% at 22°C for 14 days..... 136
Figure 6.12 Nozzle jam (A) and twisted, spring like filament removed from the jammed nozzle (B). 138

Figure 6.13 Appearance of grid models printed from filaments that contain CC extract together with PVA. 138
Figure 6.14 Print preview and intended dimensions (A), printing process (B) and printed recycling symbol (C) printed with 15% HP/PVA at 180°C (C). 140
Figure 6.15 A daisy model consisting of 20 layers printed at 180°C with 25% d-HP/PVA filament. 140
Figure 6.16 Left to right: intended model dimensions, print preview of the models to be printed and 3D models printed with 25% d-HP/PVA filament at 180°C. 141
Figure 6.17 Tensile strength of 3D printed samples from PVA and HP/PVA blends with respect to different water contents. Lines represents power law fittings. 143
Figure 6.18 Elastic modulus of 3D printed samples from PVA and HP/PVA blends with respect to different water contents. Lines represents power law fittings. 144
Figure 6.19 Elongation at break values of 3D printed samples from PVA and HP/PVA blends with respect to different water contents. Lines represents power law fittings. 144
Figure 6.20 The tensile strength of PVA and HP/PVA blends with respect to different water contents. 145
Figure 6.21 The elastic modulus of PVA and HP/PVA blends with respect to different water contents. 146
Figure 6.22 The elongation at break of PVA and HP/PVA blends with respect to different water contents. 146
Figure 6.23 Thermograms with respect to temperature and time for filaments with different formulations. 155
Figure 6.24 Thermograms for pure hemicellulose (xylan from birchwood) and alkali lignin. 156
Figure A1 Mechanical properties of 3D printed samples from PVA, 15% HP/PVA, 25% HP/PVA, 40% HP/PVA at various water contents. 179
Figure B1 1st derivative weight graphs with respect to temperature for filaments with different formulations. 181

LIST OF ABBREVIATIONS

3D: Three dimensional

4D: Four dimensional

ABS: Acrylonitrile butadiene styrene

AM: Additive manufacturing

CAD:Computer-aided design

CC: Corn cob

CLP: Colloidal lignin nanoparticles

CMC: Carboxy methyl cellulose

CNC: Cellulose nanocrystal

CNF: Cellulose nanofiber

DCW: Direct cryo writing

DIW: Direct ink writing

DLP: Digital light processing

E: Elastic modulus

eb: Elongation at break

EBM: Electron beam machining

EM: Extrusion multiplier

FDM: Fused deposition modeling

FFF: Fused filament fabrication

FTIR: Fourier-transform infrared spectroscopy

G-code: Geometric code

GGM: Galactoglucomannans

GGMMA: Galactoglucomannans methacrylates

HCl: Hydrochloric acid

HPC: Hydroxypropyl cellulose

KAc: Potassium acetate

KOH: Potassium hydroxide

LCC:Lignin-carbohydrate complex

LDM: Liquid deposition modeling

LVR: Linear viscoelastic range

MCC: Microcrystalline cellulose

MMAM: Multi material additive manufacturing

NaOH: Sodium hydroxide

PEG: Polyethylene glycol

PLA: Polylactic acid

PVA: Polyvinyl alcohol

RH: Relative humidity

SEM: Scanning electron microscopy

SLA: Stereolithography

SLS: Selective laser sintering

STL: Standard tessellation language

T_g: Glass transition temperature

TGA: Thermo gravimetric analysis

TS: Tensile strength

WB: Wheat bran

XG: Xyloglucan

LIST OF SYMBOLS

η^*: Complex viscosity

η_r: Relative viscosity

η_{sp}: Specific viscosity

$[\eta]_{int}$: Intrinsic viscosity

a and K: Mark-Houwink constants

n: Flow behavior index

K′: Flow consistency index

η_{app}: Apparent viscosity

ω: Frequency

τ: shear stress

E_a: activation energy

CHAPTER 1

INTRODUCTION

1.1 Lignocellulosic biomass

Renewable, inexpensive, and abundant lignocellulosic biomass which includes forest residues, agricultural residues, bioenergy crops, agro-industrial and municipal wastes is seen as a sustainable alternative resource to replace nonrenewable fossil based carbon resources such as crude oil for the production of value-added products such as biofuels, biopolymers and other biobased chemicals (Maitan-Alfenas et al., 2015; Zoghlami and Paës, 2019). Lignocellulosic biomass comprises two carbohydrate polymers, the polysaccharides cellulose and hemicellulose, and the aromatic polymer lignin together with minor amounts of pectin, protein, extractives and ash. (Pérez et al., 2002; Pratima, 2016). This composite structure has a significant advantage over starch-based biomass as it is not used as food and hence does not endanger food safety by creating a food vs. industrial function competition (Pratima, 2016; Sathisuksanoh et al., 2009; Zoghlami and Paës, 2019). The composition of lignocellulosic biomass varies depending on the type, species and source of the biomass and the stage of growth, storage conditions as well as the growth conditions such as the climate and the composition of the soil also affect the biomass composition. Nevertheless, typical composition of cellulose, hemicellulose and lignin in a given lignocellulosic biomass is around 35-50, 20-35% and 10-25%, respectively (Pratima, 2016; Pérez et al., 2002; Jeffries, 1994).

Plant cell wall is the major resource for lignocellulose (Marriott et al., 2016) and the components of the plant cell wall, cellulose, and hemicellulose, are intertwined through hydrogen bonds, and surrounded from outside by another component of the secondary cell wall, which is lignin. (Pratima, 2016; de Vries and Visser, 2001; Marriott et al., 2016).

Cellulose connects with hemicellulose or lignin molecules mainly through hydrogen bonds, whereas hemicellulose and lignin are connected through hydrogen and covalent bonds forming the lignin-carbohydrate complex (LCC) structures (Wang et al., 2017; Pratima, 2016; Tarasov et al., 2018; Giummarella et al., 2019).

1.1.1 Cellulose

Cellulose, the most abundant renewable polymer in the world (Maitan-Alfenas et al., 2015) is a linear semicrystalline homopolymer made of glucose subunits linked by beta-1,4-glycosidic linkages. The basic repeating unit of cellulose is cellobiose as each glucose residue is rotated by 180°C relative to its neighbors (Béguin and Aubert, 1994; Pratima, 2016; McMillan, 1997).

Cellulose chains ranging in length between 100 and 14000 residues, form rigid microfibers by establishing many intra- and intermolecular hydrogen bonds (Béguin and Aubert, 1994). Cellulose microfibers formed by the combination of 20-300 cellulose chains, are held together by van der Waals forces and hydrogen bonds and these microfibers are bundled together to form cellulose fibers, which function as the skeleton for the plant cell wall by providing rigidity and strength (Béguin and Aubert, 1994; Pratima, 2016). Major proportion of cellulose in lignocellulosic biomass is in crystalline form, while a small percentage of unorganized cellulose chains are in the amorphous form (Wang et al., 2017, Pérez et al., 2002). Even though it is a hydrophilic polymer, crystalline structure, high molecular weight and strong hydrogen bonding between the molecules make cellulose a water insoluble biopolymer (Shavandi et al., 2020).

1.1.2 Hemicellulose

Hemicellulose is the second carbohydrate polymer component of lignocellulosic biomass. Unlike cellulose, hemicellulose is not chemically homogeneous, the backbone of this biopolymer could be either a homopolymer or a heteropolymer

(Pratima, 2016). It is composed of monosaccharides including pentoses (xylose, rhamnose, and arabinose), hexoses (glucose, mannose, and galactose), and uronic acids (4-O-methylglucuronic, D-glucuronic, and D-galactouronic acids) and these sugars are linked via by beta-1,4- and occasionally beta-1,3-glycosidic bonds (Pérez et al., 2002; Shavandi et al., 2020; Pratima, 2016). The main property of hemicellulose that distinguishes it from cellulose is the existence of branches with short lateral chains comprised of different sugars. These branches block the formation of crystalline regions in the structure of the biopolymer making it an amorphous polymer (Pérez et al., 2002; Marriott et al., 2016). Compared to cellulose, it has a relatively short-chained matrix consisting of 500 – 3000 sugar monomers with acidic groups (Okolie et al., 2021; Gibson, 2012). Hemicellulose forms chains that interact through hydrogen bonds with cellulose and holds the cellulose microfibrils together at specific junctions (Marriott et al., 2016; Valent and Albersheim, 1974; Busse-Wicher et al., 2014).

Hemicellulose has a lower molecular weight compared to cellulose and can be hydrolyzed quite easily (Pérez et al., 2002). Amorphous structure and lower degree of polymerization of hemicellulose contributes to easy degradation of the polymer in acidic or hot aqueous medium (Chen, 2014). Hemicellulose forms hydrogen bonding with cellulose whereas it is covalently bonded to lignin via α-benzyl ether linkages and form ester linkages with lignin through acetyl units and hydroxycinnamic acids (Shavandi et al., 2020; Bian et al., 2012). Composition of hemicellulose changes depending on cell tissue and plant species and varies in type of glycosidic linkages, side chain composition, and degree of polymerization. For instance, straw and grasses contain hemicelluloses composed mainly of xylan while softwood hemicelluloses are composed mainly of glucomannan (Pratima, 2016; Chundawat et al., 2011).

1.1.3 Lignin

Lignin, which is a hydrophobic heteropolymer, is the third major component of lignocellulosic biomass with three monomers, which are coniferyl alcohol, sinapyl alcohol, and p-coumaryl alcohol (Shavandi et al., 2020). These phenolic monomers are bound together through alkylaryl, alkyl-alkyl, and aryl-aryl ether bonds (Kim et al., 2016). Lignin has high molecular weight due its highly branched, cross-linked structure and it is water insoluble at ambient conditions due to its hydrophobic nature (Okolie et al., 2021). The polymer has various aromatic groups, and it has a 3D structure which is amorphous and highly complex (Pratima, 2016). Chemical structure and functional groups of lignin differs significantly depending on the extraction method performed to isolate the polymer (Okolie et al., 2021). Lignin has been identified as a 'glue' as it binds different components of lignocellulosic biomass, and cross-linking of lignin molecules with cellulose and hemicellulose polymers provides the plants with the necessary strength and rigidity (Okolie et al., 2021). Presence of lignin in the cell wall provides a resistance to microbial attack and oxidative stress while also hindering the enzymatic and microbial hydrolysis of lignocellulosic biomass and therefore removal of the lignin from the composite structure of biomass is considered as a requirement to enhance biomass digestibility (Kim et al., 2016).

1.2 3D printing

Three dimensional (3D) printing, also known as rapid prototyping or additive manufacturing (AM), is defined in International Organization for Standardization (ISO)/American Society for Testing and Materials (ASTM) 52900:2015 standard as "the process of joining materials to make parts from 3D model data, usually layer upon layer, as opposed to subtractive manufacturing and formative manufacturing methodologies". The real object is created directly layer-by-layer with the help of a 3D printer and any special tools like a mold or a cutting tool are not required as in

the case of conventional subtractive and formative manufacturing technologies. Computer-aided design (CAD) is used to generate the model to be printed with a huge design flexibility (Ligon et al., 2017). At early stages of the development, additive manufacturing technologies were used to produce the prototypes of tools and machine components by the engineers. Later, in the 2010s, commercial and more affordable 3D printers have emerged, and the first commercial application of 3D printed parts took place in the aerospace industry (Ligon et al., 2017). The technology continues to evolve from producing prototypes and models to producing functional final products for a wide range of application areas such as energy, medicine, and food (Ligon et al., 2017). In order to compete with the mass production technologies, issues of 3D printing related with production speed, post processing steps, mechanical performance and spatial resolution of the 3D printed parts, developing new printing materials, expanding and improving the multi material additive manufacturing (MMAM) techniques need to be addressed (Ligon et al., 2017).

1.2.1 3D printing process steps

The first step in 3D printing process is digital model creation which is carried out with CAD. Printing process starts with a digital file derived from the CAD software. Alternatively, the digital model can be created via 3D scanning and tomographic images from X-ray, MRI, etc. (Ligon et al., 2017).

Once the design is completed in CAD software, it is exported as a standard tessellation language (STL) file. At this stage, the file is translated into triangulated surfaces and vertices. STL file is then imported into printer's software in which it sliced into hundreds or thousands of two-dimensional layers and turned into a set of instructions in machine language called as geometric code (G-code) for the printer to execute (www.3dhubs.com/knowledge-base). These two steps are performed in the same way whatever the 3D printing technology is. From this stage on printing process varies by technology.

As the next step, print materials, binders, and other materials that the printer will use are loaded to the 3D printer based on the machine requirements and thereafter, the printer follows an automated process which can only be interrupted when an error in the software occurs or machine runs out of material (www.core77.com; www.alma.edu.php). It may take from several minutes to a day or more to complete the 3D printing process depending on the model, printing material, printing device and process parameters such as the printing speed and layer height. Once the 3D model is created, it is removed from the build platform of the printer and the ease of removal of the printed object depends on the selected 3D printing technology. In case of industrial 3D printing methods, printed part removal is a highly technical process including precise extraction of the print, complicated removal procedures and highly skilled machine operators (www.core77.com). Parts printed with many of the 3D printers require post processing such as support removal, sanding, welding, painting, high-pressure air cleaning, smoothing, and polishing as the final step of the printing process. This step is seen as a drawback of the additive manufacturing and should be eliminated as it complicates the printing by adding costs and increasing the delivery time (www.techbriefs.com).

1.2.2 Printing materials

Each 3D printing technology is compatible with different printing materials. Physical form of 3D printable materials is generally in the shape of filaments, powders, or resins. Available print materials are categorized mainly as polymers (plastics) and metals. 3D printing is also possible using other materials, such as ceramics and composite materials. Today, 3D printing space is experiencing the development of new materials quite frequently, which are being explored to expand the potential applications of the technology (www.3dhubs.com/materialindex). Polymeric materials (thermoplastics and thermosets) are widely used in 3D printing industry (Wang et al., 2017). Acrylonitrile butadiene styrene (ABS) and polylactic acid (PLA) polymers dominate the desktop fused deposition modeling (FDM) printing market

and are similar in cost. These polymers are also filled with carbon, glass or other additives since parts printed with this composite approach have the desired mechanical strength and functionality (Wang et al., 2017). Some of the other commercially available 3D printing materials are as follows: acrylic styrene acrylonitrile, nylon, polyethylene terephthalate glycol, thermoplastic polyurethane, polyvinyl alcohol (PVA), high impact polystyrene, polyoxymethylene, polypropylene, composites such as fiberglass reinforced nylon, carbon-reinforced nylon, kevlar-reinforced nylon, glass-filled polyamide powder, mineral-filled polyamide powder, carbon fiber filled nylon powder, glass bead filled nylon powder, aluminum filled nylon 12, metal-filled PLA and wood fiber-filled PLA (https:// formlabs.com; www.3dhubs.com).

Other than polymers, metals are also processed with 3D printing technologies to produce parts for high-end engineering applications. Titanium, stainless steel, aluminum, tool steel nickel alloys are the prevalent 3D printing metals (https://formlabs.com). Other 3D printable metals are chromite, iron infiltrated with bronze, iron-chrome-aluminum alloys, bonded tungsten, tungsten carbide (https://formlabs.com). Metal 3D printing costs is expected to further decrease through the emergence of extrusion-based metal 3D printing systems since currently the dominant approach in this area is to use metal powders and sintering these powders with a laser source (https://formlabs.com).

Other than polymers and metals, ceramics are also used as 3D printing materials for art and for industry. 3D printing technologies, with their extensive design freedom, have the potential to overcome the difficulty of producing complex shaped ceramic parts (Chen et al., 2019). Hydroxyapatite, tricalcium phosphate, tetracalcium phosphate, calcium silicate are common 3D printable ceramics and ceramics are also combined with polymers to be processed with certain 3D printing technologies to produce sensors, biomedical implants, and dental components (Chen et al., 2019; Vorndran et al., 2015).

Development of new 3D printable materials together with the enhancement in the properties of the existing printing materials are needed to make the 3D printing an integral part of manufacturing (Hofmann et al., 2014; Negi et al., 2013). Lignocellulosic biomass is a good candidate in the search for sustainable and renewable alternative 3D printable materials to replace the fossil-based printing materials in the market.

1.2.3 3D printing technologies used for biomass and biomass derived materials

There are so many different 3D printing technologies available, and these are classified mainly under seven different groups based on the differences of the layer deposition method and the selected printing material type by ASTM International Committee in 2009 (Ligon et al., 2017). In material extrusion 3D printing processes, fused deposition modeling (FDM), fused filament fabrication (FFF), 3D dispensing, and 3D bioplotting, printing material is deposited by a nozzle while the droplets of the printing material is selectively deposited on to the build platform in the case of material jetting 3D printing processes like inkjet printing. Print material is in powder form in binder jetting technologies and these powders are fused by selectively applying a liquid bonding agent. Instead of a bonding agent, a laser or an electron beam is used to selectively fuse the powder polymer or metal printing material in powder bed fusion type printing processes like selective laser sintering (SLS) and electron beam machining (EBM). Printing materials in sheet form are bonded together to obtain the 3D model in sheet lamination additive manufacturing process. Metals deposited as printing materials are melted and fused together by laser or plasma arc in directed energy deposition 3D printing technologies. In vat photopolymerization, photosensitive liquid polymer in a vat is selectively cured by light-activated polymerization and most of the lithography-based technologies such as digital light processing (DLP), and stereolithography (SLA) belong to this category (Ligon et al., 2017).

Lignocellulosic biomass derived polymers are mainly used in 3D printers using material extrusion, vat polymerization and binder jetting technologies among the seven categories mentioned above (Ji et al., 2020). The biopolymers isolated from lignocellulosic biomass are often modified and combined with other materials to make these biopolymers 3D printable. Generally, they are used in already existing 3D printable SLA resins and FDM filaments to reinforce the physical properties, biocompatibility, and biodegradation of the 3D printed models or alternatively, they are often blended with polymers to reach the rheological requirements of the selected printing method or with ceramics to aid the printing process and stabilization of 3D prints (Ji et al., 2020). Water affinity of cellulose and its derivatives is utilized in some printing methods to prepare well-dispersed suspensions that have suitable rheological behavior for material extrusion 3D printing (Ji et al., 2020). Cellulose based powder materials are also processed with binder jetting technologies. Attempts have been made to 3D print the entire lignocellulosic biomass with auxiliary materials by using a material extrusion-based 3D printing method which originally designed to extrude ceramic materials (Henke and Treml, 2013).

The following subsections include the basic operating principles of the 3D printing technologies used to process lignocellulosic biomass and its components.

1.2.3.1 Fused deposition modeling (FDM)

Among the mentioned technologies, FDM is the most widely applied technology to print lignocellulosic biomass and materials derived from it. In FDM technology, the thermoplastic polymer filament heated above its melting temperature is extruded from the nozzle moved to simulate the object geometry and then stacked in layers to form a 3D object. Mechanical force is applied to extrude the filament out of the nozzle. FDM printers have X–Y–Z three axis motion platform and single or multiple nozzles. The filament is extruded following a predetermined path with the movements of in XY axes to complete patterns in one layer. Once one layer is completed, another layer is deposited on top of the previous one by moving the

printer's head up or alternatively by moving the build platform down (Zhou et al., 2020). Adjustable process parameters are mainly the nozzle and the build platform temperature, the print speed, the layer height and cooling fan speed. Typically, available build size of a desktop FDM 3D printer is 200 x 200 x 200 mm, but these dimensions can be as large as 1000 x 1000 x 1000 mm in the case of industrial machines. The typical layer height used in FDM ranges between 0.05 and 0.4 mm, most widely a layer height of 0.2 mm is used. Today, FDM is preferred for its advantages of low-cost prototyping and design verification with very fast turnaround times. However, this technology has the lowest dimensional accuracy and resolution considering other 3D printing techniques, hence production of parts with intricate details is not possible (Perez et al., 2014). It is also not recommended to produce mechanically critical components since the parts printed are inherently anisotropic which means they are expected to be weaker in one direction due the layer adhesion mechanism (Perez et al., 2014).

1.2.3.2 Direct ink writing (DIW)

DIW is an extrusion-based printing technique like FDM. Print material is a viscoelastic ink, which is deposited through a fine nozzle by applying pressure. Distinguishing characteristic of DIW is the room temperature extrusion of print material as the printability solely depend on the rheological properties of the ink regardless of printing temperature. At the end of printing process, deposited filament is solidified under ambient conditions or an auxiliary process such as solvent evaporation, gelation, solvent-driven reactions, heat treatment, and photocuring is used such as to solidify and fix the shape of the printed object (Saadi et al., 2022). Resolution of the printed parts is in the range of 0.1 - 1.2 mm for the X-Y layer and 0.1 - 0.4 mm for the Z axis and minimum feature size is around 0.5 mm (Saadi et al., 2022).

1.2.3.3 Liquid deposition modeling (LDM)

Although the operating principle of the LDM method is the same as the DIW method, it was originally developed for 3D printing of highly viscous ceramic pastes. Printing material in the form of a paste is transferred to deposition arm by applying pneumatic pressure. The syringe holding the print material moves along the Z axis to deposit the wet filament through the nozzle onto the build platform which moves along the XY axes (Postiglione et al., 2015; www.3dprintingmedia.network; Bezzi et al., 2022). As in the case of DIW, material is extruded through the nozzle at room temperature without applying heat. LDM is an advantageous printing technique as it is cost-effective due to the low costs of the printer, high printing rate and ability to print at room temperature (Bezzi et al., 2022).

Reaching the level of precision of plastic polymer extruder is possible with this technology when pneumatic extrusion is combined with the screw extruder (www.3dprintingmedia.network). Although being primarily developed for 3D printing of traditional ceramics, the technology has been tested for processing new feedstocks like wood flour (Bezzi et al., 2022). Desktop FDM 3D printers could also be used in LDM printing by replacing the standard printing head with a syringe extruder for fluid deposition (Postiglione et al., 2015).

1.2.3.4 Binder jetting

In binder jetting print materials is in the powder form and the layers made up of the powder material are glued by a binding agent to 3D print the desired model. As described by Ji et al. (2020) powder print material is spread on the build platform with the help of a roller. Binding agent droplets are selectively deposited from the print head onto powdered material wherever necessary. Once a layer is completed, platform moves downward by one-layer thickness of the model and another layer of powder again spread on previously printed layer. Meanwhile, unbound powders surround the object to be created. Same procedure is followed until the target pattern

is formed (Ji et al., 2020). Post processing is required to improve the mechanical properties of the 3D printed parts. Binder jetting is not always appropriate to create structural parts and the need for post processing significantly increases the process time (Wang et al., 2017).

1.2.3.5 Stereolithography (SLA)

First commercialized 3D printing technique, SLA, is still widely used today for its high fabrication accuracy and speed (www.3dhubs.com/knowledge-base; Ji et al., 2020). The SLA setup consists of a container that holds photocurable liquid resin and a laser source (UV light in most of the cases) that induces the polymerization and crosslinking of liquid resin. The solid SLA part is obtained by moving the laser beam in the XY axis and with the movements of the build platform in Z axis (Li et al., 2020). Build platform is submerged in a translucent tank full of liquid photopolymer. Single-point laser maps a cross-sectional area (layer) of a design starting from the bottom of the tank and solidifies the print material. Once the layer is mapped and solidified, build platform is lifted and the process is repeated in a layer-by-layer fashion until the solid part is produced. Post processing by UV light is performed most of the time to improve mechanical properties of the printed part (Li et al., 2020).

1.2.3.6 Digital light processing (DLP)

Another form of 3D printing technology, DLP, follows a quite similar method as SLA to produce parts. As the only difference, in DLP process digital light projector is used to flash a single image of each layer all at once instead of a single point laser used in SLA process (Ji et al., 2020). This property shortens the printing time and hence, DLP prints faster compared to SLA. These two similar technologies would be a better option if the main design consideration is visual appearance rather than functionality. SLA/DLP prints are relatively brittle and are not suitable to use

outdoors as their mechanical properties and color degrade when exposed to UV radiation from the sun. On the other hand, the technology enables to produce parts with high dimensional accuracy, intricate details, and a very smooth surface finish (Ji et al., 2020).

1.3 Objective of the study

Developing novel 3D printable materials is one of the essential components for the 3D printing technology. Considering the increasing environmental concern in the world related to the utilization of non-biodegradable fossil-based synthetic polymers, using biodegradable polymers obtained from renewable resources in 3D printing applications is crucial to make the overall process sustainable.

The present study focuses on developing novel biodegradable polymers suitable for 3D printing, which were obtained from renewable resources. The renewable resource in this case is lignocellulosic agricultural wastes, which are among the most abundant biopolymer resources on earth. Lignocellulosic biomass is mainly composed of three biopolymers, which are cellulose and hemicellulose and lignin. However, even though hemicellulose and lignin constitutes almost a half of any given lignocellulosic biomass, the attention these two polymers receive is much less than the interest on cellulose-based materials. In other words, utilizing these two polymers and developing novel application areas for them in the context of polymer science and technology will enable the further utilization of lignocellulosic agricultural wastes such as CCs, which are the major lignocellulosic biomass resource used in this study.

In this context, the present study aims to provide the utilization of lignocellulosic agricultural wastes, which also accumulate in huge quantities in Turkey, together with one of the most up-to-date polymer processing technologies with the highest potential. At the same time, processing of hemicelluloses and lignins together, which are currently only available via techniques such as solvent casting and very recently

extrusion (available only on laboratory scale) were made possible via 3D printing for the first time in the literature.

CHAPTER 2

LITERATURE REVIEW

2.1 3D printing of hemicellulose

There are very limited examples in the scientific literature that use hemicelluloses (together with other polymers and/or in their modified form) in 3D printing processes. The limited number of examples involving hemicelluloses for 3D printing include the utilization of tyramine functionalized xylan together with cellulose nanofibers (CNFs). Markstedt et al. (2017) modified hemicellulose, which is extracted from spruce, with tyramine in order to introduce crosslinking property to CNFs bioink formulation. The prepared formulations were printed with the pneumatic printer head using the conical needle (outlet diameter 0.42 mm) and the printed constructs were crosslinked by submerging them in a bath of 1% H_2O_2 solution in water for 10 minutes. The authors reported that the tyramine-functionalized xylan alone was not printable even at high concentrations (300 mg/mL) due to the low viscosity and 3D parts printed with only CNFs cannot retain their shape and collapsed easily without crosslinking. Minimum CNF and tyramine-functionalized xylan concentrations to obtain a printable gel formulation were found to be 2.5% and 5%, respectively. Best printing resolution was obtained with the ink with a degree of substitution of 19% containing 2.7 wt.% CNF, 10.6 wt.% tyramine-functionalized xylan, and 86.8 wt.% water content. The ink has been shown as a candidate for tissue engineering or wound dressing applications due to its ability to form gel with high water content (~ 90%).

Markstedt et al. (2019) used tyramine functionalized xylan and CNFs to 3D print wood composite structures. The inks were used to develop packaging materials for

food and pharmaceuticals. Using an approach that aims to reconstruct wood tissue via 3D printing, solid particles were encapsulated into the printed honeycomb shaped materials, which were fixed by enzymatic cross-linking.

Other examples involving hemicelluloses for 3D printing include the utilization of galactoglucomannans (GGMs) (major hemicellulose type in softwoods) with CNF and PLA.

A similar approach utilizing cross-linkable modified hemicellulose and galactoglucomannans methacrylates (GGMMAs), together with TEMPO-oxidized CNFs, was used to obtain biomimetic inks with CNF:GGMMA ratios of 1:2 and 1:3 (Xu et al., 2019). Unlike the previous study, UV induced cross-linking was used to produce scaffolds and other grid patterned objects (such as a nose) from these inks by 3D printing. The authors have shown that this cross-linking strategy could work more compatible with 3D bioprinting applications as it increases the polymerization rate and shortens the gelation time. Lightweight TEMPO-oxidized CNF/GGMMA hydrogel scaffolds showed good cytocompatibility in the cell cultures of human dermal fibroblasts and pancreatic tumor cells and tunable control over the mechanical stiffness of the hydrogel was reported to provide promising applications in tissue engineering, cancer cell research, and high-throughput drug screening.

Xu et al. (2018) used GGMs isolated from Norway spruce via thermomechanical pulp, together with PLA for 3D printing. PLA/wood hemicellulose composites were prepared via solvent blending method and the dried blends were extruded into filaments with different blend ratios and with a diameter in the range of 1.75 ± 0.15 mm by hot melt extrusion method. Thermal stability of neat PLA filament was found to be decreased while viscosity of neat PLA filament was found to be increase with the addition of GGM. The storage modulus of composite filaments was higher than that of neat PLA filament at the low angular frequencies. The difference in storage modulus values between composite and PLA filaments was found to become less significant at angular frequencies higher than 7 rad/s. Similar flexural modulus values were determined for neat PLA and composite filaments except for the

filament containing 25 wt.% GGM which showed lower flexural modulus value. This result was attributed to the hindered PLA polymer chain entanglement and subsequent intermolecular phase separation when the GGM content increased to 25 wt.%. Scanning electron microscopy (SEM) results revealed that the addition of GGM modified the smooth and compact surface of scaffolds printed with neat PLA was to rough and porous and it was proven via SEM images that the blends of GGM and PLA immiscible due to the phase separation as GGM aggregates appeared both on the printed stripe surface and in the filament bending cross-section. Based on these findings, 3D scaffold prototypes were printed using PLA/ GGM filaments and the maximum content of GGM in PLA melt that would not deteriorate the properties of the printed materials was reported to be limited to 20 wt.%.

Xyloglucan (XG) type hemicelluloses were used as binders for the 3D printing of cellulose nanocrystals (CNCs). Kam et al. (2019) have presented a new approach for 3D printing of bioinspired structures via a material extrusion-based 3D printing method, Direct cryo writing (DCW). Ink compositions containing both CNCs and XG (4 wt.% overall solids) were 3D printed on a custom-made temperature-controlled cold platform and the resultant printed part was lyophilized to obtain 3D printed aerogels. Parts printed from pure CNC dispersions were found to easily collapsed into films upon drying at ambient conditions without freezing while pure XG solutions did not meet the rheological requirements to be 3D printable by demonstrating Newtonian flow behavior. A combination of CNC and XG was reported to be necessary as CNC provides the required rheological properties for 3D printing, while XG provides the ability to enhance mechanical properties and to control the internal structure of the printed parts. The viscosity of the CNC dispersion was found to increase with the XG addition suggesting that the XG mimicking its role in the plant cell wall by “gluing” together cellulosic building blocks into 3D objects in addition to functioning as a rheological modifier. Organized and tubular structure of aerogels were observed to change to disordered and flakey pores as in the case of the structure of various wood species when XG content in formulation was increased. Hence, the authors have concluded that it is possible to create wood-

like structures with controlled internal morphologies without additional support materials and post-printing processes via additive manufacturing technologies using renewable wood-based materials.

In another study by Kam et al. (2019), two different 3D printing technologies, namely binder jet and extrusion printing were used to print wood substitute materials in which four different wood flour microparticles (eucalyptus, wood flour from hardwood, pine, and maple) were "glued" with xyloglucan in CNC based matrix. In the study, the authors first followed the path of determining the optimum ink compositions to fabricate wood-based parts by the conventional molding and then utilized the optimum compositions to fabricate 3D parts via extrusion and inkjet-based printing technologies. A "harem window", multi-material chess board, nut and screw, a window and a cylinder were demonstrated in the article as examples of DIW, DCW and binder jet 3D models. In the extrusion approach, 40% volumetric shrinkage was measured when DIW printed parts was left to dry at ambient conditions, correspondingly dense rigid printed parts were obtained. This shrinkage was prevented by the sublimation of the ice for the DCW printed parts. Hence, extrusion-based techniques resulted in printed parts with a wide range of densities (100 vs 850 kg m^{-3}). Dense 3D printed parts were demonstrated to be processable with the conventional tools utilized for natural wood, the density of which was reported to vary between 160 and 1300 kg m^{-3}, depending on the type of the tree. Modulus and strength of the printed parts were reported to be within the range of natural woods while thermal conductivity of the printed parts was found to be remarkably low.

2.2 3D printing of lignin

Just like the case with hemicelluloses, blending with other polymers is also a popular strategy for the utilization of lignin in 3D printing. 3D printing of lignin together with PLA was reported in several studies in which the lignin concentration ranged from 0.5% up to 50%.

One of the reasons for using lignin together with PLA was to create a material with antioxidant properties (Domínguez-Robles et al., 2019; Tanase-Opedal et al., 2019; Yao et al. 2021).

Domínguez-Robles et al. (2019) 3D printed samples which intended to be used in health-related fields by adding antioxidant feature to PLA by means of lignin. Lignin powder and castor oil coated PLA pellets were extruded into filaments which contained lignin ranging from 0% to 3% (w/w). Squares (1 cm x 1 cm), different shapes and meshes (0.4 mm thickness) with different grid sizes (1 and 1.5 mm) designed for wound dressing purposes were 3D printed using the PLA and 2% (w/w) lignin composite filament. The antioxidant capability of the resultant 3D printed samples was investigated via 2,2-diphenyl-1-picrylhydrazyl method and it was found out that the materials containing lignin demonstrated radical scavenging activity. Still, mechanical performance of the samples printed from pristine PLA filament were superior to that of samples printed from the composite filament. Among the composite filaments, the highest resistance to fracture was recorded when the lignin content was 0.5%.

Tanase-Opedal et al. (2019) evaluated the 3D printability of PLA/20% and 40% softwood lignin biocomposite filaments. The presence of lignin was found to deteriorate the mechanical properties of 3D printed parts. It was determined that the printing temperature influences the mechanical performance of the printed lignin containing filaments as tensile strength and elastic modulus were improved by 56% and 40%, respectively, when the printing temperature was 215ºC instead of 230ºC. This mechanical test result was also confirmed through the SEM images since printed threads of 3D printed structure were clearly visible at 205ºC while an improvement of bonding of the printed layers was observed at 215ºC. Decrease in tensile strength and modulus values by further increasing the printing temperature to 230ºC was attributed to degradation of the carbohydrates in the lignin fraction at this temperature. Lignin-containing biocomposites was reported to demonstrate antioxidant activity owing to antioxidant property of lignin.

Yao et al. (2021) demonstrated a new way to modify alkali lignin without using a catalyst or a solvent before the fabrication of PLA/lignin blends to enhance its compatibility with PLA and to prevent lignin agglomeration. The authors reported that it was not possible to fabricate continuous filaments of PLA and the unmodified lignin even at low concentration (10 wt.%). Lignin content of the composite filament could be increased up to 50% by utilizing microwave-assisted functionalization to hydrophobize alkali lignin. Best tensile properties which were comparable with the neat PLA tensile properties were achieved with PLA/lignin blends containing 10 wt. % acetylated and 10 wt.% hexanoated lignin. Still blends containing up to 50 wt.% acetylated lignin were reported to have good melt-processability, 3D printability, and mechanical properties comparable to neat PLA. 3D parts printed from PLA/ acetylated lignin composite filaments demonstrated UV-shielding and antioxidant properties based on the free radical scavenging, UV−vis spectroscopy, and oxidation induction temperature determination experiments.

In some studies, it was also reported that the addition of lignin to PLA might have a negative impact on the mechanical properties of 3D printed materials compared to pure PLA.

Wasti et al. (2021) investigated the effect of two different plasticizers on thermal and mechanical properties of composite filaments fabricated from PLA and organosolv lignin (hardwood). Maximum addable percentage of lignin was determined as 20 wt.%. Composite filaments with a diameter in the range of 1.6–1.9 mm was 3D printed at 210ºC printing and 60ºC bed temperature with an FDM machine equipped with a nozzle diameter of 0.4 mm. As composite filaments exhibited a lower mechanical performance compared to pristine PLA filament, two different plasticizers (polyethylene glycol (PEG) 2000 and struktol TR451) were used in the study with the hypothesis that plasticizers would prevent lignin agglomeration and consequently improve mechanical properties. Best mechanical performance was obtained with the addition of 2 wt.% PEG (19% improvement in tensile strength and 35% improvement in elongation). It was found that the composite filaments had 11% lower tensile strength value compared to pristine PLA filament, even in the presence

of plasticizers. Presence of lignin was found to decrease the onset decomposition temperature of PLA while maximum degradation temperature did not affect. Adding 1 wt.% PEG or struktol did not change the TG curve of PLA. Maximum degradation temperature was shifted to a lower temperature when the polyethylene glycol content was increased to 2-5 wt.%. Glass transition temperature (T_g) of PLA was decreased by 6°C with the lignin addition while plasticizers did not affect the glass transition temperature.

Hong et al. (2021) fabricated PLA-based biocomposite 3D printing filaments with acceptable diameter tolerances (1.41 ± 0.072 mm) and with varying COOH-lignin contents in the range of 5-20 wt.%. Organosolv lignin was chemically modified to improve interfacial adhesion between the filler and the polymer matrix. Addition of pristine lignin reduced both tensile strength and the tensile modulus values while chemical modification applied to pristine lignin led to an improvement in tensile strength and tensile modulus. Still measured tensile strength value for chemically modified lignin containing filament could not exceed that measured for pure PLA.

Mimini et al. (2019) investigated the blending of PLA with Kraft lignin, Organosolv lignin, and lignosulfonate without the addition of any solvent, compatibilizers or other reagents. The report also investigated the 3D printability of unmodified lignin-PLA composite filaments in FDM. It was determined that both flexural and impact strength of the samples printed from composite filaments containing 5, 10, and 15 wt.% lignin was slightly lower than those printed from pristine PLA filament. Highest compatibility was obtained when PLA was blended with organosolv lignin while lignosulfonate-PLA blends were reported to reveal encouraging results in terms of 3D printability.

Gkartzou et al. (2017) investigated physical properties and melt processability of kraft pine lignin/PLA filaments. 5 wt.% lignin content was selected among different lignin concentrations (5, 10, 15 and 20 wt.%) as higher lignin contents were reported to result in severe agglomeration and increase the material's brittleness and melt's apparent viscosity during extrusion. A remarkable increase in surface roughness of

fibers were observed through the addition of lignin. Dog bone specimens were printed from PLA/lignin filaments containing 5 wt.% lignin at 205°C extrusion temperature and 20 mm/sec printing speed to characterize the mechanical properties. Elongation at break (eb) and ultimate tensile strength (UTS) values were found to decreased by 40% and 15%, respectively when the PLA filaments contain 5 wt.% lignin.

Other than PLA, lignin was blended with other polymers. Nguyen et al. (2018) prepared nitrile-butadiene rubber–hardwood lignin, nylon 12-hardwood lignin, and nylon 12-hardwood lignin-carbon fiber composites which were then extruded into filaments to be processed with FDM. The renewable alternative to ABS where the styrene component is replaced with lignin was determined to be unfavorable for FDM. The filaments of modified nylon blends containing 40 to 60 wt.% lignin could be processed with FDM (>170ºC), and the parts printed revealed enhanced mechanical properties. This enhancement in mechanical properties was related with the presence of rigid phenolic units in lignin.

Mohan et al. (2021) used biodegradable fillers obtained from agricultural biomass to improve the mechanical properties of 3D parts printed with ABS filament. Lignin was isolated via organosolv treatment and homogenized with graphene nanoplatelets prior to blending with ABS at varying loadings. 3D printing was performed at relatively high temperature (250ºC) with a commercial FDM printer. Tensile specimen printed with neat ABS (printed at 0º orientation) had the highest tensile stress compared to ABS composite filaments reinforced with lignin, graphene nanoplatelets, and lignin/graphene nanoplatelets. Further increasing the lignin concentration above 5 wt.%, mechanical properties were reported to be deteriorated due to agglomeration and increment of voids in the parts printed. Best mechanical performance was measured when the dog bone shaped specimen printed with ABS composite filaments containing 5% lignin and 0.50% graphene nanoplatelets. Cubic structures and a complex calibration test model (3DBenchy) could be printed with

composite filaments containing 5% lignin and 5% lignin together with 0.50% graphene nanoplatelets.

Vaidya et al. (2019) used biodegradable polyhydroxy butyrate to blend with lignin for the fabrication of 3D printing composite filaments. Based on the melt rheology results, the formulation contained up to 20% w/w biorefinery lignin in polyhydroxy butyrate was chosen to evaluate 3D printability and quality of the printed parts. Flat objects were printed at 190°C nozzle and 40°C build platform temperatures using an FDM printer equipped with a 0.75 mm nozzle. Quality and shrinkage of the resultant samples were reported to be improved when printing was performed with polyhydroxy butyrate:biorefinery lignin (20% w/w) filament. Parts printed with lignin contained filament showed between 34 to 78% less warpage compared to the 100% polyhydroxy butyrate printed object.

Gleuwitz and coworkers (2020) blended lignin with hydroxypropyl cellulose (HPC) and investigated the feasibility of HPC/organosolv lignin binary solvent mixture (3:1 w/w) for DIW. Citric acid and Pripol 1017 were used as crosslinking agents. As example of 3D models, double-layered grids and a 3D ring structure were demonstrated in the article. Printed structures were found to display hydration behavior based on the swelling tests. Size of the printed grids was observed to be reduced considerably after 20 min contact with water especially in the case of the printed structures crosslinked with citric acid. The authors emphasized that the shape fidelity, warpage, and solidification issues should be improved.

Implementation of lignin with HPC in DIW is also presented in Ebers et al.'s study (2020). A printability window for organosolv lignin solutions of 45, 47.5, and 50% solid contents and organosolv lignin / HPC w/w ratios of 30/70, 40/60, and 50/50 was identified based on the prescreening tests to conduct the further optimization studies. Prescreening tests were performed simply by loading the bioinks to the syringe with a two different needle tips (metal tip with a diameter of 0.57 mm and a conically shaped plastic tip with a diameter of 0.41 mm). A layer of the bioink were dispensed manually and the printability was assessed visually through the shape of

the extrudate. To assess layer stacking or merging, two layers of bioink was dispersed again manually on top of each other. Required viscoelastic properties for DIW was reported to be achieved only for formulations with organosolv lignin /HPC ratio at or above 50/50 and with 45 to 50% solid content through the shear thinning property contribution of HPC and stability and solid-like property contribution of lignin. Best performance in terms of the shape fidelity, morphology, and mechanical properties (995 MPa Young's modulus, 18.5 MPa tensile strength) of printed monolayers was reported to be achieved through the ink formulation with a solid content of 47.5% and organosolv lignin/HPC ratio of 50/50. Formulations with solid contents of 47.5 and 50% and organosolv lignin/HPC ratios of 40/60 and 50/50 were used to DIW 3D objects consisting of multiple layers. Still, the mechanical properties of DIW models were reported to be inferior to the mechanical properties of those obtained by FDM of lignin combined with thermoplastic polymers.

Spherical colloidal lignin nanoparticles (CLPs) were used in the formulation of CNF-sodium alginate inks to prepare scaffolds (cylindrical shape 1.5 cm in diameter, 2 cm in height) with a 3D bioprinter for biomedical applications in the study of Zhang et al. (2020). Print material was prepared by altering the CLP/CNF ratio (0-15% w/w) where the concentration of CNF and sodium alginate in the final ink were kept constant as 2 and 0.5 wt.%, respectively. The presence of lignin, depending on its concentration, enabled the 3D printed scaffold structures to display antioxidant properties and contribute to the print resolution without modifying the desired rheological behavior of the ink at a CLP/CNF ratio up to 25%.

Äkräs (2019) used CLPs which were prepared from the lignin from softwood kraft pulping together with CNF and alginate for tissue engineering and regenerative medicine 3D printing applications. The bioink were formulated by changing the lignin nanoparticle concentrations (1-5-10-25%) relative to the dry weight of CNF in solutions containing 2.5 wt.% CNF and 0.5% alginate. Ink rheology, printability, compression, and structural stability in different storage conditions which were humidity chamber, freeze-drying and re-wetting, salt-water solution, and free-standing were investigated in the study. Increasing CLP concentration in bioink

formulation was found to increase the viscosity of the bioink and shrinkage of the printed parts. Best hydrogels based on the investigated properties were selected as ink formulations containing 10 and 25% CLP. Hydrogels containing 10 wt.% CLP was reported to have high viscosity, good repeatability, re-wetting properties and shape retention when exposed to high moisture and salt-water solutions. These samples also showed good mechanical properties straight after 3D bioprinting and freeze-drying and re-wetting. Hydrogels containing 10 wt.% CLP was reported to have superior bioink strength which significantly resulted in to obtain models with high resolution and stability right after bioprinting process. Easy dissolution in salt-water solution and rather fast drying with significant shrinkage under ambient conditions was pointed out as handicap of these samples. The authors also reported that the further research is needed related with the non-toxicity and degradation rates inside the human body of these hydrogels.

Lignin was also used together with 3D printable SLA resins. Ibrahim et al. (2019) utilized organosolv lignin and graphene nanoplatelets as filler and reinforcement in photo-curable polyurethane resin. Lignin used in the study was extracted from oil palm empty fruit bunch fibers with an organosolv extraction method in which the formic acid was used. Curing was carried out with UV light with a wavelength of 405 nm. Maximum load of the filler-reinforcement was limited to 3% as higher loadings were reported to interrupt the curing behavior of the photo-curable polyurethane resin. The highest improvement in mechanical properties of SLA printed parts were achieved when the concentration of lignin-graphene was 0.6% and above 0.8%, mechanical properties were found to be deteriorated. The incorporation of graphene nanoplatelets yielded 238% increment in hardness compared to unmodified polyurethane resin.

Feng et al. (2017) combined photoreactive methacrylate resin with lignin-coated cellulose nanocrystals at various contents of 0, 0.1, 0.5, and 1 wt.% to overcome dimensional instability (shrinkages) and poor mechanical properties of SLA printed parts. Following the printing process, a post cure treatment which performed at elevated temperature was applied with the intention of enhancing the material

properties. Interaction between the matrix and the reinforcement was found to be deteriorated at high lignin-coated cellulose nanocrystals content (1 wt.%) because of the aggregation of lignin-coated cellulose nanocrystals and uneven dispersion in the matrix which was also observable through the SEM images. Accordingly, lignin contents at which the mechanical performance of the printed material enhanced were determined as 0.1 and 0.5 wt.%.

Zhang et al. (2019) used softwood kraft lignin (0.2−1.0 wt.%) as filler in commercially available methacrylate resin to enhance the mechanical properties of printed structures. UV absorption property of lignin was reported to inhibit the complete polymerization of the methacrylate resin and consequently decreased the degree of crosslinking which resulted in to obtain printed parts with lower stiffness with the increasing lignin content. Lignin content of 3D printed parts was measured higher than expected and this was attributed to inefficient dispersion of the unmodified lignin which was also reported to be observed by the settled lignin polymers at the bottom of the printer reservoir while printing. Low charges of lignin (0.2−1.0 wt.%) was found to enhance the mechanical properties of printed structures (46-64% increase in TS, 13-37% increase in elastic modulus (EM)). This enhancement was related in the article to the rough fracture surfaces of lignin containing samples observed via SEM images which probably dissipate the stress concentration. The authors also designed a post curing process to printed parts in order to complete the crosslinking of non-gel fraction and reported that the post curing process improved the mechanical properties of the printed parts.

Sutton et al. (2018) formulated a modified lignin contained photoactive acrylate resin that can be processed with a commercial desktop SLA 3D printer. Lignin was modified (acylated via methacrylic anhydride) with the intend of further improving the ultimate material properties through covalent linkages instead of noncovalent hydrogen bonding or physical cross-linking. Maximum modified lignin content of the fabricated resin to remain within the operable viscosity and cure property ranges was determined as 15 wt.%. Mechanical testing has shown that the incorporation of organosolv lignin (15 wt.%) into commercial SLA acrylate resin decreased the

elastic modulus of SLA prints from 0.65 to 0.37 GPa and increased the elongation and ultimate tensile strength from 1.87 to 7.6% and from 11 to 15 MPa, respectively. Lignin incorporation was also found to decrease the thermal stability of the photoactive resin.

Alkali and kraft lignin obtained from hardwoods and softwoods were made 3D printable by using a chemical crosslinker to improve the rheological properties of lignin when mixed with water. Jiang et al. (2020) showed for the first time that lignin-based inks could be 3D printed via DIW technology at room temperature regardless of its type or molecular structure. Mechanical ultrasonication was applied to overcome poor water retention of the polymer and unfavorable rheological properties of lignin for printing were reported to be overcome by the addition of chemical crosslinker, Pluronic F127, to the ink formulation consisting of lignin and water. Prepared inks were reported to form a flexible gel at room temperature which can be squeezed out from a syringe as a continuous filament without extra particle refining to lignin. Lignin concentration in the printable ink formulation was determined to be in the range of 38% to 56% and final 3D printed part consists of 83 wt.% lignin. The report also includes a comparative analysis of DIW of cellulose and lignin in terms of water stability, density, mechanical and thermal properties of final printed parts.

2.3 3D printing of entire lignocellulosic biomass with all of its components

The use of whole lignocellulosic biomass without fractionation in 3D printing was also investigated. Predominantly, the processing of wood with 3D printing technologies were studied by preparing a wood paste containing water and other auxiliary materials. The study by Henke and Treml (2013) was the first to demonstrate the utilization of wood in LDM. Wooden chips made of spruce were used as the bulk material, gypsum, methyl cellulose, sodium silicate and cement were tested as binders. Different geometries oriented in different directions were 3D printed successfully. Best results were obtained with chips/cement ratio of 0.15 and a water/cement ratio of 0.80. The authors were reported that the mechanical

properties of the printed parts were suitable for the use in non-structural applications only.

The resolution of the LDM printed parts was further improved in the study of Kariz et al. (2016) by using 3 mm nozzle diameter. Different ratios of beech wood powder and polyvinyl acetate or urea–formaldehyde adhesives (12.5, 15, 17.5, 20, 22.5 and 25%) were used to print four-layered simple blocks with dimensions of 150 x 30 x 8 mm^3. Polyvinyl acetate blends with 17.5 and 20% and urea–formaldehyde mixtures with 15 and 17.5% wood loadings could be 3D printed. The models printed from those formulations were printed on a hot surface (80°C) and cured on a surface of 50°C for 2 hours and left to ambient conditions to complete the solidification process. Printed blocks were found to shrink upon drying especially in terms of thickness which was measured as 22% for the urea–formaldehyde and 17% for the polyvinyl acetate adhesive mixture. Material flow was also reported to contribute to this shrinkage; therefore, it was recommended to scale up the model before initiating the printing process. Mechanical performance of the 3D printed parts containing polyvinyl acetate adhesive was found to be inadequate whereas parts printed with wood and urea–formaldehyde mixture was reported to have the potential to be used only in non-structural applications.

LDM was also used in the study of Rosenthal et al. (2018) for 3D printing of wood. Paste-like suspensions containing ground beech sawdust and methylcellulose dissolved in water were printed with a standard Cartesian 3D printer with a cylindrical plastic cartridge as an outlet an 8 mm nozzle. Volumetric shrinkage of the printed models upon drying were found to be between 17.3 and 20.0%. Density of the parts printed from sawdust/methylcellulose/water pastes was measured in the range of 0.33 and 0.48 g/cm^3 while modulus of rupture and modulus of elasticity were determined to be in the range of 2.3 to 7.4 and 284.8 to 733.1 N/mm^2, respectively. 89% wood content in dry mass were reported to be achieved. Still the authors emphasize that the strength properties, dimensional stability, and the spatial resolution is required to be improved.

To improve the mechanical properties of printed parts and to reduce the use of adhesives, Henke et al. (2021) introduced a new method named as 'Individual layer fabrication' for the utilization of wood in additive manufacturing. In preliminary experiments, a truncated cone with a base diameter of 200 mm, upper diameter of 100 mm and height of 100 mm was demonstrated to be 3D printed with spruce wood chips with a particle size of 0.8–1.1 mm and a layer thickness of 2 mm. To overcome design freedom limitations, layers were proposed to be individually fabricated rather than applying pressure to the whole model during the printing process. Desired model was obtained by first spreading a thin layer by a scattering device, then applying the adhesive through a print head specifically to the areas where the bulk will be bound. Individual layer fabrication was completed by applying the mechanical pressure with a press, the unbound bulk was removed, and each panel were stacked and laminated in the end. It has been reported that the proposed method needs improvement in terms of material properties, shape accuracy, geometric freedom, process speed and reliability.

Whole lignocellulosic biomass was also used in already 3D printable thermoplastic filaments as reinforcing agent. Kariz et al. (2018) blended beech wood flour with commercial thermoplastic PLA and ABS filaments to fabricate composite filaments for FDM. Commercial filaments were compared with the composite filaments prepared with 5 different wood loadings (10-50%) in terms of density, mechanical, thermal, and rheological properties of the printed parts. Composite filaments were fabricated in 1.45 - 1.75 mm diameter range. Density of the printed part was found to be decreased from 0.63 g/cm^3 to 0.48 g/cm^3 with 50% wood loading. It has been shown that the existence of wood in the filaments did not change the glass transition temperature whereas the surface of the printed parts became rougher, more porous with visible clusters of wood particles. More than 10% wood content was found to impair the tensile strength of the printed parts while elastic modulus could only be improved up to 20% wood contents. Hence, it was reported that at low loadings, wood particles behave as a reinforcing agent. Deterioration of mechanical properties at higher loadings was explained with poor bonding and limited load transfer as the

polymer could not encapsulate the wood particles completely. The requirement that the size of wood particles be small enough to pass through the opening of the printer's nozzle was reported as an obstacle to obtain 3D parts with comparable performance and properties to those printed from the commercially available thermoplastic filaments.

To better understand the effect of particle size of wood fillers on thermal, mechanical, and rheological properties of the 3D printed parts, Zhao et al. (2019) conducted a study in which the composite filaments were fabricated with PLA and poplar fibers of different mesh sizes (<180, 180−425, 425−850, and 850−2360 μm). Optimum size range of poplar fibers to produce biocomposites which intended to be used in large-scale 3D printing was determined to be less than 180 μm. Composites prepared from smaller poplar fibers (<180 μm) were found to increase the tensile strength by 59%, have more compact fracture surfaces with fewer voids and possess more pores on their outer surfaces, which serve as access and penetration sites for PLA. Based on the rheology measurements, the composites demonstrated a shear-thinning behavior and the complex viscosity of the composites prepared with <180 μm poplar fibers was determined to be in the optimum viscosity range which reported as approximately 100−10000 Pa.s. for 3D printing via a desktop-scale extrusion-based hydrogel 3D printing system. A 3D printed podium base model was as provided in the article as evidence of suitability of prepared poplar/PLA composites for large-scale 3D printing.

The potential of wood's hygroscopic nature, which is shown as a drawback for the properties of parts printed with wood polymer composite filaments, was investigated by Le Duigou et al. (2016) to produce moisture-sensitive smart materials via FDM 3D printing. For this purpose, a commercial filament which is a blend of PLA and poly(hydroxyalkanoate) matrix, reinforced with recycled wood fibers were used to 3D print self-bending hygromorphic biocomposites that actuate in response to a moisture gradient and to establish a relationship between FDM, and actuation properties induced by natural-fiber composites. Inspired by the natural actuators such as pinecone microstructure, a bilayer microstructure with differential elastic and

swelling properties were 3D printed. Samples were printed by changing the printing width as 100, 200 and 300% as this parameter is significant for biocomposite properties which affect the internal cohesion of the printed specimen. It was observed that the biocomposite bilayers start actuating by bending themselves once immersed in water and after immersion, the transformation was found to be partially reversible (50% curvature recovery for samples with 100% and 200% printing width, 60% curvature recovery for samples with 300% printing width). Maximal curvature and actuation speed of wood biocomposites were improved through FDM process. In the end, the authors concluded that the optimization of biocomposite formulation was required to enhance the actuation performance, and especially durability.

Kariz et al. (2018) investigated the behavior of wood-PLA filaments with different wood ratios (10%, 20%, 30%, 40%, and 50%) under dry (T=20°C, RH 33%), standard (T=20°C, RH 65%), humid (T=20°C, RH 87%) environment to guide the production of smart materials via four dimensional (4D) printing. Simple rectangular shapes (80 × 12 × 4 mm) having top and bottom solid layers and a mesh inner structure were printed with an FDM printer and conditioned in different climates. Filaments with higher wood content were determined to possess the higher moisture content, larger dimensional swelling, and lower EM value. EM value was found to decrease by 47% under standard clime conditions when the wood addition to PLA was only 10%. Non-homogeneous printing due to nozzle clogging, insufficiently fused layers, small dimensions/aspect ratio of wood particles which was limited with the printer's nozzle diameter, wood particles not fully encapsulated with polymer was proposed by the authors as the possible reasons of obtaining lower bending properties for the parts printed with wood particles. These negative characteristics were reported to be beneficial for forming 4D printing materials that undergo climate induced shape changes.

Ecker et al. (2018) fabricated PLA/wood composite filaments for FDM and immersed the samples printed from these filaments in tap water at room temperature for seven days to understand to effect of water absorption on mechanics and morphology of printed samples. The study also provided a comparison between two

different productions methods, namely 3D printing and injection molding in terms of the properties of the fabricated parts. Mechanical performance of PLA and PLA/wood composite samples were reported to remarkably reduced with the "softening effect" of water especially for the 3D printed ones with the higher wood loadings. Water absorption capability was found to increase with the wood addition to PLA, no matter what the production method was selected. 3D-printed samples absorbed faster and more water than the injection molded ones which was ascribed to the porous structure of the PLA specimen when produced via 3D printing. Both unfilled PLA as well as its composites showed better mechanical performance when produced by injection molding. Unlike the composite samples, TS of unfilled PLA samples did not affect significantly by the storage in water, hence mechanical performance reduction in composite filaments was related with the wood content.

In order to improve the compatibility between the polymer and wood, Xie et al. (2017) used different plasticizer combinations (4% glycerol, 2% glycerol + 2% tributyl citrate, 4% tributyl citrate) in wood flour/PLA blends and fabricated composite FDM 3D printing filament. The effect of plasticizer combinations on mechanical properties, melt index, water absorption and heat stability were investigated. Based on the melt index experiments glycerol was favored as plasticizer for the extrusion processing of the composite filaments while 4% tributyl citrate performed better in terms of compatibility, water absorption, mechanical and thermal properties.

Zander et al. (2019) used wastepaper and cardboard (<20 wt.%) to fabricate polypropylene composite filaments. Recycled polypropylene (from yoghurt containers) and commercial polypropylene were used in the composites which were prepared via solid-state shear pulverization process. The problem of warping, which is generally encountered in 3D printing of polypropylene, was found to be reduced when the composites prepared with recycled polymer. The addition of biomass-derived materials was found to decrease the TS of polypropylene.

Liu et al. (2019) used different plant fibers (bleached pulp board, mechanical pulp board, newspaper powder, eucalyptus powder, pine powder and lignin) to melt blend and produce PLA based 3D printing composite. Plant fibers were modified by silane coupling agent (KH550) to improve the compatibility between the plant fibers and the polymer. The effect of fiber type and content (up to 20%) on density, melt flow, compatibility, thermal and mechanical properties was investigated and the composite with the best performance was determined to test its 3D printability. A remarkable increase in the density of the PLA with the increasing fiber content was determined, especially when the PLA was blended with lignin. Increasing amount of modified fiber was found to reduce the melt flow rate of PLA. Best TS values were measured for the composites when the fiber content was 15% and among all the plant fibers tested, modified lignin/PLA composite gave the best TS value with the 74% improvement compared to pristine PLA sample. The deterioration of mechanical properties when the fiber content was further increased to 20% was explained by the authors as the inability of the fibers to be fully encapsulated by the polymer and consequent fiber agglomeration in the composite structure which was also proven via the SEM images. 3D printing experiments were performed with the filament containing 15% modified lignin and the composite filament was reported to fulfill the requirements of 3D printing.

CHAPTER 3

MATERIALS AND METHODS

3.1 Materials

CCs obtained from Kırklareli, Turkey were utilized as the main agricultural waste in the study. Potassium hydroxide (KOH), sodium hydroxide (NaOH), acetic acid, hydrochloric acid (HCl), alkali lignin, xylan from birchwood, micro crystalline cellulose (MCC) and ethanol (95%) were purchased from Sigma-Aldrich. PVA filaments were purchased from E-Sun.

3.2 Biopolymer extraction from CCs

A large variety of alkaline extraction parameters including solid to liquid ratio, extraction temperature, alkali concentration and extraction time were used in the study, and these depend on the processing method that was used to process the extracted biopolymers hemicellulose and lignin. The extraction parameters were tuned in order to obtain the most suitable polymer formulation for the processing method.

Prior to the extraction of hemicellulose and lignin from CCs, the biomass was ground by using an impact mill. The ground CC particles were separated by using a sieve to have a particle size of < 2 mm. Biopolymers were extracted from CCs via alkaline extraction by following previously described methods (Zilliox and Debeire, 1998) by soaking and mixing ground biomass with a magnetic stirrer in 3, 5 or 10% (w/w) KOH solution for 1, 3 or 24 h at room temperature, 60°C or 80°C with a solid to liquid (biomass to alkaline solution) ratio of 1:3, 1:4 or 1:5. At the end of the extraction period, the insoluble material in the medium, which are the cellulose rich fractions of CC particles, were removed by filtration. These particles were washed

extensively by water, neutralized and dried for further analysis. Depending on the polymer processing technique, at the end of the extraction, the solubilized biopolymers in the alkaline medium were either precipitated (by the addition of 10% acetic acid ethanol solution as an antisolvent) or the water content of the medium was reduced by evaporation in a magnetic stirrer. In the case of precipitation, the precipitated polymers were collected by filtration.

3.3 Preparation of hemicellulosic pastes

The hemicellulosic pastes used in 3D printing are obtained from the precipitated biopolymers as described above. Following the alkaline extraction process performed with 10% KOH solution at 60°C for 1 h, the hemicellulosic polymers were mixed with water with or without NaOH. Extracted hemicelluloses were not allowed to dry and 16 ml of water or 16 ml of 10 wt.% NaOH solution was added to 100 g of wet hemicellulosic paste, which was thoroughly mixed mechanically. To adjust the water content of the hemicellulosic pastes, the pastes were treated in an oven at 60°C for different periods of time until the desired water content was reached. A moisture content analyzer (Mettler Toledo Halogen Moisture Analyzer HS153) was used to determine the water content of the pastes.

3.4 Preparation of CC gel extracts

The precipitation and polymer recovery step performed at the end of extraction to prepare hemicellulosic paste is bypassed in the preparation of gel extract samples. CCs were subjected to alkaline extraction by using a 3%, 5% or 10% KOH solution at room temperature, 60°C or 80°C for different periods of time including 1 h, 3 h and 24 h. In a typical extraction performed to obtain a gel, CCs (50 g) were mixed with the alkaline solution (200 ml) containing 5% KOH for 3 h with magnetic stirring at 80°C. At the end of the 3 h period the insoluble particles in the mixture were removed with a filtering cloth and the remaining dark brown colored solution, which

is referred to as the CC extract, was concentrated by evaporating around 60% of its water content at 80°C by continuous magnetic stirring. The concentrated extract was left to cool at room temperature and upon cooling it formed a gel, which was used for 3D printing experiments. A typical extraction yields 12.36 ± 0.45 g (3 replicates) of material on a dry basis that constitutes the gel from 50 g of CC as the starting material. The CC fraction which was not solubilized during the alkaline extraction was recovered and washed 5 times with 1 L of DI water for each washing cycle. Upon washing this fraction was dried at room temperature for 72 h before analysis.

3.5 Preparation of blends containing hemicellulosic pastes or CC extracts together with PVA

In order to prepare the blends containing the hemicellulosic paste, 10 grams of commercial PVA filament (E-Sun) was cut into small pieces (Figure 3.1A) and added into 50 ml of DI water and stirred for 1 h at 60°C. Relevant amount of hemicellulosic paste to prepare the blends containing 15, 25, 40 and 50 wt.% paste on dry basis was dispersed in DI water at 60°C for 1 h. Slurries containing the paste and PVA were mixed and stirred for 1 h at 60°C. Hemicellulosic paste–PVA blends were poured into plastic petri dishes with a diameter of 9 cm and left to dry at 40°C in an oven for 48 hours. After 48 hours dried blends were detached from the petri dishes as intact films and the dried films were stored in a plastic box containing silica beads with humidity indicator due to the moisture sensitivity of PVA (Figure 3.1B).

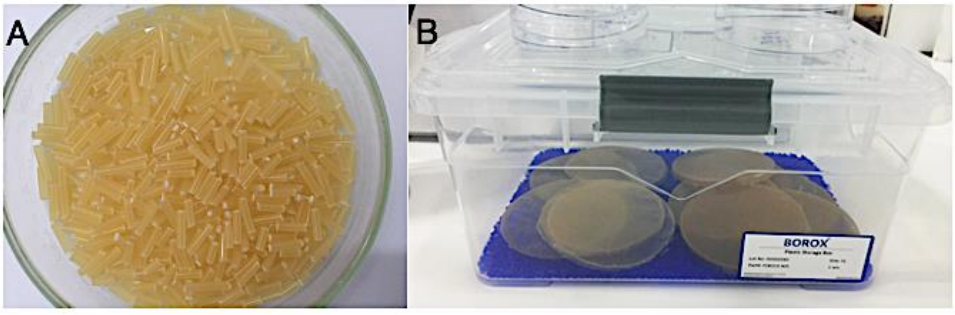


Figure 3.1 Chopped PVA filament (A) and storage container used for blend films, filaments and printed 3D models (B).

In order to prepare the blends containing the CC extract, 10 grams of commercial PVA filament was chopped and added to 50 ml of DI water at 60°C and stirred for 1 h. The relevant amount of extract required to obtain blends with extract loadings of 25 and 40 wt.% on a dry basis was calculated considering the water content of the extract, which was determined with a moisture content analyzer. The extract was directly added to the PVA slurry to obtain blends with different extract concentrations. Each blend was stirred at 60°C for 1 hour, poured into plastic petri dishes and left to dry at 40°C for 48 hours.

Desalted hemicellulosic paste–PVA blends were prepared produced in the same way that the salted samples were produced. Only, the blend with 40 wt.% desalted hemicellulosic paste was further concentrated by stirring at 60°C until its volume was reduced by 50% in order to avoid the heterogeneous appearance with fragmentation upon drying of the samples.

Pure PVA samples were also prepared by dissolving 5 g of chopped PVA filament in 50 mL of DI water at 60°C for 1 hour. The slurry was poured into plastic petri dishes and left to dry at 40°C oven for 48 hours.

To prepare films from the hemicellulosic pastes alone, 13 g of hemicellulosic paste with a water content of around 70% was mixed with 60 ml water at a temperature of 60°C for 1h.

3.6 Desalting the hemicellulosic paste

The potassium acetate (KAc) content of the hemicellulosic paste was reduced by removing this salt from the paste. For this purpose, 65 grams of hemicellulosic paste was washed five times with 200 ml of ethanol-water solution containing 70% (v/v) ethanol. 10 mL of 10% NaOH solution was added to the desalted hemicellulosic paste. The paste was left in oven at 60°C for one hour to evaporate ethanol and to adjust the water of the desalted paste around 70%.

3.7 Filament fabrication from blends containing hemicellulosic pastes and CC extracts together with PVA

The blends containing the hemicellulosic paste and CC extracts films were stored in a closed box containing silica beads until the filament fabrication experiments were performed. Blend films were chopped and subjected to an extra drying step in the oven at 170°C for 20 minutes just before the filament fabrication experiments in order to eliminate the negative effects of any residual water on the filaments. Filaments were obtained by using a capillary rheometer (Dynisco, LCR-7001) equipped with a die having a diameter of 1.524 mm. The piston speed of the rheometer ranged between 8 – 30 mm/min at a temperature of 170 - 200°C depending on the type of the blend as discussed in detail in the upcoming chapters. The die diameter was chosen intentionally smaller than the target diameter (1.75 ± 0.05 mm) since the all the materials swell as they leave the die.

3.8 3D printing of hemicellulosic pastes, CC extracts and filaments containing PVA

A custom-made 3D printer was built in cooperation with 3D4E (Ankara, Turkey) and used throughout the printing studies (Figure 3.2). The printer is capable of printing solid polymer filaments as well as viscous liquids and pastes by changing its printing head accordingly.

As shown in Figure 3.2A, the 3D printer used in the study is a cartesian desktop FDM 3D printer. The printing process is performed on to a build platform, which can be heated to certain temperature. The dimensions of the build platform are 20 cm x 20 cm. It is crucial to correctly calibrate this platform manually prior to any printing operation to obtain a properly printed object. The printing apparatus in which the printing heads are attached to can move in the X and Z axes by the help of electric step motors where the build platform only moves in the Y axis again with the help of an electric step motor.

The 3D printer is controlled with a software named Simplfy3D. The object to be printed, which is initially in the CAD format, is imported to the Simplfy3D software. The Simplfy3D software enables a large variety of 3D printing parameters to be set for the 3D printing operation. The 3D printing parameters that can be controlled with the Simplfy3D software include; print speed, layer height (height of a single layer deposited during printing), extrusion width (width of a single layer deposited during printing), nozzle temperature, built platform temperature, cooling fan status and speed, depositing support layers or skirts prior to the main printing operation, setting polymer filament diameter, infill % (to set weather the inside of the object to printed will be hollow or filled with polymer), printing pattern while building an object (honeycomb, rectilinear, grid, triangular, and wiggle).

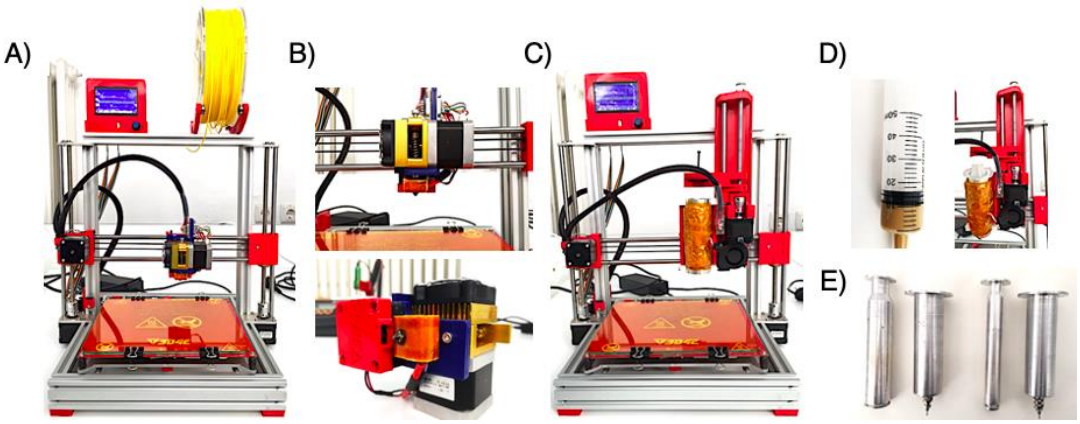


Figure 3.2 Appearance of the 3D printer with the standard extruder head attached for filament printing (A). Standard extruder head in more detail (B). Appearance of the 3D printer with the syringe printing head attached for paste and gel printing (C). Polypropylene (D) and stainless-steel syringes with to different inner diameters (E) that can fit into the barrel of the syringe printing head.

Syringe printing head of the 3D printer was used to print the paste and gel samples instead of using the standard extrusion printing head of the printer suitable for the printing of solid filaments. Two stainless-steel syringes with two different inner diameters (29 mm and 19 mm) were manufactured to be used with the printing head for printing the hemicellulosic pastes and gel extracts in the present study (Figure

3.2E). The paste or extract samples were loaded to the stainless-steel syringe, which perfectly fits to a barrel surrounded with a heating coil on the printer, which enables controlling the printing temperature with this printing head. Once the sample is loaded to the syringe, the plunger is closed, and the plunger flange is fitted to the cavity on the 3D printer head. A step motor moves this part of the printer head at a previously determined rate to turn a screw, which pushes the plunger flange down, forcing the sample to come out of the syringe's nozzle. The printer can be equipped with 12 different interchangeable nozzles that have inner diameters between 0.54 mm-3.30 mm. Among those 12 nozzles, the ones with inner diameters of 0.68 mm and 0.54 mm were the most frequently used ones during the study. Hemicellulosic paste samples and CC extracts were printed on a glass surface and this surface was also covered with a polymer stretch film depending on the subsequent washing step. The models printed with hemicellulosic paste were removed from the build platform and left to dry at ambient conditions while the models printed with CC extract were removed from the build platform together with the stretch film and immersed into an ethanol bath for 5 min. Once in the ethanol bath, the models immediately solidified, and they were detached from the stretch film by themselves. At the end of the immersion period, the models were removed from the ethanol bath and dried at ambient conditions for 24 h prior to analysis.

Filaments containing PVA were also printed with the same 3D printer by using its standard extrusion head. Prior to the experiments, the diameter of the filaments was measured from several different points with a digital micrometer (Mahr 40 EXL) and this value was set as the filament diameter in the software. Printing temperature of filaments was much higher compared to that of the pastes or the extracts since the filaments contain at least 50% PVA, which needs a printing temperature between 170°C - 210°C. Models obtained from the filaments were printed directly onto the glass build platform, which was preheated to a temperature of 75°C to create the sufficient adhesion of the first layer of the models.

3.9 Rheological characterizations

Complex viscosities (η*) of different hemicellulosic pastes having different water contents were measured using a rheometer (TA Instruments ARES) with a parallel plate geometry (25 mm diameter and 0.5 mm gap). Apparent viscosities (η_{app}) of the hemicellulosic pastes were measured using a capillary viscometer (Dynisco 7100) using a capillary die with 25 mm length and 0.76 mm diameter. Viscosities of the blends containing hemicellulosic paste or extract together with PVA were also measured by a capillary viscometer (Dynisco 7100).

Rheological characterization of CC extracts with different water contents were measured using a rheometer (TA Instruments ARES) with a co-axial cylindrical geometry (34 mm cup diameter, 32 mm bob diameter, and 50 mm length). After determining the linear viscoelastic range (LVR) of CC extract samples, the dynamic oscillatory frequency sweep tests ranging from 1 to 100 rad/s were conducted at various temperatures. The maximum strain amplitude of 0.5 % (within the LVR) was selected for all measurements.

3.10 Determination of mechanical properties

Dog bone shaped specimens were 3D printed from the hemicellulosic pastes, extracts and PVA containing filaments along the length of the specimens (parallel to the tensile testing direction) to determine the mechanical properties by tensile testing. For this purpose, a Zwick/Roell Z250 universal testing machine equipped with an extensometer was used. Mechanical properties of 3D printed specimens including TS, eb and E were determined by using a 100 N or 10 kN load cell at a crosshead speed of 5 mm/min for the pastes and extracts and 20 mm/min for the PVA containing filaments.

In addition to 3D printed samples, solvent cast films were also tested for their mechanical properties. In this case, a manual cutting press was used to obtain dog-

bone shaped samples. All the tests were made with at least 3 parallels and the thickness together with the width of each dog-bone shaped specimen was measured with a digital micrometer prior to tests.

The effect of different water contents on the mechanical properties was investigated for the models printed from the PVA containing filaments. For this purpose, the samples were conditioned in three different environments with different relative humidity (RH) values to obtain samples with different water contents. The samples were conditioned at a RH of 47% and 15% in addition to being conditioned at 40°C in an oven for 1 day.

3.11 Water content determination

A moisture content analyzer (Mettler Toledo Halogen Moisture Analyzer HS153) was used to determine water content of the pastes, extracts, filaments, 3D printed samples and solvent cast films. The analyzer uses a halogen lamp as the heating source retains the set temperature within a precision of ±1°C throughout the drying procedure. Analyzer stops drying after a given period of time while displaying the drying curve in real time as the drying process proceeds. At the end of the drying process the water content of the specimen together with the drying curve is recorded by the device and can be exported if desired in .csv format for further analysis.

3.12 Scanning electron microscopy (SEM)

SEM analyses were performed with a QUANTA 400 F field emission SEM at low vacuum with an accelerating voltage of 20 kV. The samples were coated with gold-palladium coating prior to analysis. For cross-sectional analysis with SEM, samples were fractured in liquid nitrogen.

3.13 Fourier-transform infrared spectroscopy (FT-IR)

FT-IR was performed with a Perkin-Elmer Spectrum 400 between 400 and 4000 cm^{-1}. 16 scans were recorded for each sample with a resolution of 4 cm^{-1}.

3.14 Thermo gravimetric analysis (TGA)

TGA was performed with a Perkin Elmer Pyris 1 under nitrogen atmosphere with a heating rate of 10°C/min up to 900°C. The temperature was kept constant for 15 min at 105°C during measurements to eliminate any effect the water content of the samples might have on the measurements.

3.15 Determination of PVA molecular weight

Apparent viscosities of the PVA solutions were measured using an Ubbelohde viscometer. A PVA solution in water with a known concentration was passed through the capillary of the viscometer. The time it takes for the solution to flow between the two marked points in the capillary was recorded as the flow time. The temperature was kept constant during the measurements of flow time of solvent (water) and the PVA solutions. PVA solutions in water were prepared with different PVA concentrations (from 0.375 g/dL to 3 g/dL) and first, the flow time for the solvent (t_0) was measured. Flow time measurements were repeated three times for each sample, relative (η_r) and specific (η_{sp}) viscosities were calculated using the average flow time which was provided in Table 3.1.

The intrinsic viscosity ($[\eta]_{int}$), which shows the capability of a polymer to increase the viscosity of the solution, can be obtained by using the Huggins or Kraemer equation. The plot of η_{sp}/c or $In(n_{rel})/c$ against concentration at a fixed temperature is a straight line (Figure 3.3), with the intercept on Y axis showing the value of $[\eta]_{int}$. Viscosity average molecular weight of PVA was determined by using the Mark-Houwink equation:

$$[\eta]_{int} = K * M^{a} \qquad (3.1)$$

where a=0.76 and K= $2x10^{-4}$ dL/g Mark-Houwink constants for PVA-water system (www.rsc.org/suppdata.pdf).

As shown in Table 3.2, viscosity average molecular weight of PVA was determined as around 9500 g/mol.

Table 3.1 Results of measurements made for the calculation of PVA molecular weight.

Concentration (g/dL)	*Flow time (s)*	$n_{rel}=t/t_0$	$n_{sp}=n_{rel}-1$	*HUGGINS* (n_{sp}/c)	*KRAEMER* $ln(n_{rel})/c$
0.375	38	1.118	0.118	0.314	0.297
0.75	41	1.206	0.206	0.275	0.250
1.5	50	1.471	0.471	0.314	0.257
3	83	2.441	1.441	0.480	0.297

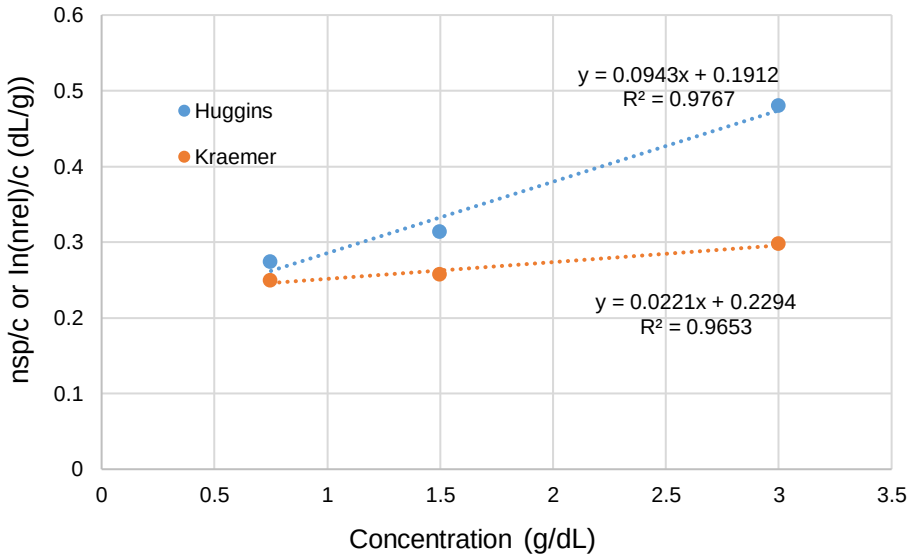


Figure 3.3 Data points obtained from Huggins and Kraemer equations for determining the intrinsic viscosity of PVA.

Table 3.2 Molecular weight calculated from the corresponding Mark-Houwink constants.

	n	*K*	*a*	*Molecular weight (g/mol)*
Huggins	0.1912	$2x10^{-4}$	0.76	8349.40
Kraemer	0.2294	$2x10^{-4}$	0.76	10610.63
Average	0.2103	$2x10^{-4}$	0.76	9463.78

3.16 Determination of hydrolysis degree of PVA

Titration was performed for the determination of hydrolysis degree in PVA by following previously described method (Aruldass et al., 2019). PVA was dried by using the moisture content analyzer before performing the experiment. At first, a blank test by using a 0.5 M NaOH solution was performed without any PVA. 0.5 M HCl solution was prepared by diluting 37% (w/w) HCl. 0.2 g of phenolphthalein was dissolved in 100 mL of 50% ethanol solution to be used as an indicator. After the blank test, 1 g dried PVA was added in 25 mL of 0.5 M NaOH, and 25 mL of DI water and the mixture was treated for 30 min at 100°C with magnetic stirring. When the mixture was cooled down to room temperature, a few drops phenolphthalein solution was added to this mixture. Immediately, the titration was initiated by adding the HCl solution to the mixture while gently swirling the contents of the flask. When the end point (the point where the color change is observed) was reached, the amount of HCl consumed was recorded. Degree of hydrolysis for PVA was calculated as 84.73% using the equations below (Aruldass et al., 2019).

$$S = 39.997(V_2 - V_1).\frac{M}{W} \qquad (3.2)$$

$$DH = 100 - \frac{(7.84.S)}{100-(0.075.S)} \qquad (3.3)$$

where S is the saponification value; V_2 is the volume of HCl consumed by blank; V_1 is the volume of HCl consumed by sample; M is the molarity of HCl solution (0.5 M); W is the weight of sample (1 g); DH is the degree of hydrolysis.

CHAPTER 4

3D PRINTING OF HEMICELLULOSIC PASTES

The main objective of this study is to develop novel approaches that will render hemicellulose and lignin found in lignocellulosic biomass 3D printable without any chemical modifications that might impact the biodegradability of these biopolymers. Rendering hemicellulos and lignin 3D printable is important because together these two biopolymers make up around half of a given lignocellulosic biomass by weight. In other words, despite they are hugely available biopolymers, the attention they have received so far has been severely limited unlike cellulose, the other major biopolymer found in lignocellulosic biomass. In this context, one of the first approaches developed in this study was the 3D printing of hemicellulosic pastes by using a custom-built 3D printer capable printing pastes and viscous inks thanks to its specially designed and manufactured printing head consisting of a syringe connected to a step motor. In this context, various paste formulations were developed and tested for their printability. The present chapter of the study is the first example in the literature in which hemicelluloses were used in 3D printing without any chemical modifications and/or without mixing them with another polymer to aid in the 3D printing process. Hemicelluloses were alkaline extracted from CCs, a widely available resource of lignocellulosic biomass, and were used in the form of hemicellulosic pastes and different models were printed from these biopolymers by employing different paste formulations and 3D printing parameters.

4.1 Preliminary studies on the general factors influencing the 3D printability of extracted hemicellulosic biopolymers

The current phase of the study starts with preliminary experiments on the 3D printability of hemicellulosic pastes by focusing on the pastes' flow and viscosity.

Since 3D printing of unmodified hemicelluloses in an unexplored territory in the literature, a large set of preliminary experiments had to be made and the initial decisions on the paste formulations were based on the appearance of the printed models. Following these initial trials, more systematic and detailed analysis and measurements were made regarding the rheological properties of the pastes since this way the effect of paste formulation as well as 3D printing parameters such as temperature on the viscosity of the pastes could be determined. Following the rheological measurements, a second set of experiments for 3D printing the hemicellulosic pastes were designed and executed, which enabled the successful 3D printing of hemicellulosic pastes where models with different shapes could be printed including a scaffold prototype while also allowing for the calculation of printability values that enables the quantification of the 3D printing experiments. Finally, the mechanical properties of the 3D printed models were also determined by tensile testing.

The main objective during the preliminary trials is to obtain an extrudable paste capable of retaining its structure once it's deposited on to the build platform. For this purpose, the alkaline extracted dry hemicellulosic portion was dissolved in deionized water to obtain a homogeneous paste however complete dissolution could not be obtained this way. In order to obtain a paste without aggregates, 1 wt. % aqueous sodium hydroxide solution was prepared to dissolve the dried hemicellulosic portion since hemicellulose is more prone to dissolve in basic conditions. However, since there were still aggregates in this case, instead of drying the hemicellulosic fraction after alkaline extraction from CCs, hemicellulosic portion was used while it was still wet. The NaOH solution was directly added to the wet hemicellulosic fraction, and a paste was obtained this way.

It was observed that the paste could flow continuously from a syringe and forms self-supporting extrudates on the glass surface. The extrudates that were dispersed manually with the syringe on the glass surface were solidified following a drying period of 24 hours.

Following the preliminary trial with the syringe, the printability of the paste was assessed qualitatively through visual inspection by using the 3D printer. The printer is equipped with a special printing head suitable for printing pastes where a syringe fitted to a barrel is connected to a step motor that precisely forces the material inside the syringe to flow out of the nozzle of the syringe. For the initial trials with the 3D printer, a rectangular model which is 40 mm long, 30 mm wide and 10 mm high with an infill percentage of 50% was 3D printed at room temperature. It was observed that the 3D printer could extrude the hemicellulosic paste almost continuously even though the shape of the printed model was far from being perfect.

As shown in Figure 4.1, there were obvious variations in the dimensions of the first layer of the 3D printed model compared to the intended (original) dimensions, especially when the infill pattern is considered. The print-preview provided by the 3D printing software is also given in Figure 4.1. Comparing the print-preview image and the actual printed model clearly reveals that the gaps that should exist between the printed lines of the infill pattern were almost totally absent since the thickness of these lines were considerably more than intended, creating a pattern where there is almost no separation between the lines. It was observed that once deposited through the nozzle, these lines spread on to the build platform because of the low viscosity of the hemicellulosic paste. A low viscosity is known to give a bad printing fidelity and inhibits the possibility of printing several layers without the printed structure collapsing. Aforementioned observation suggests that the hemicellulosic paste should have been more viscous to achieve the desired shape fidelity.

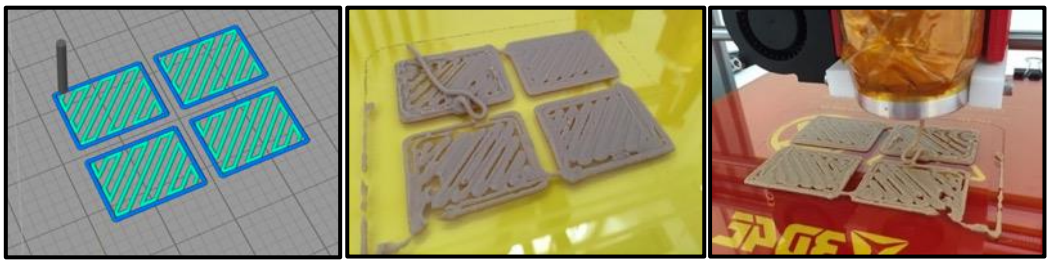


Figure 4.1 Print-preview and the first layer of the 3D printed model obtained during the one of the first preliminary experiments with the hemicellulosic paste.

The amount of sodium hydroxide added to avoid agglomeration by making the pH of the hemicellulosic paste basic was reduced by half to increase the viscosity of the paste. The first layer of the model was printed again at room temperature to observe the effect of reducing the NaOH content where it was determined that the printed lines were rougher compared to the previous trial. The infill pattern was printed more successfully this time, with some separation between the lines even though it was still far from being identical to the model drawn with the software. The visual differences of the first layers, provided in Figures 4.1 and 4.2, are likely due to the different viscosities the pastes, which was a result of different NaOH contents since all other parameters were identical in both of the preliminary experiments. For both of the experiments, shrinkage of the printed models was observed following their drying period at ambient conditions for 24 hours, which was a result of the reduction of their water contents during the drying period.

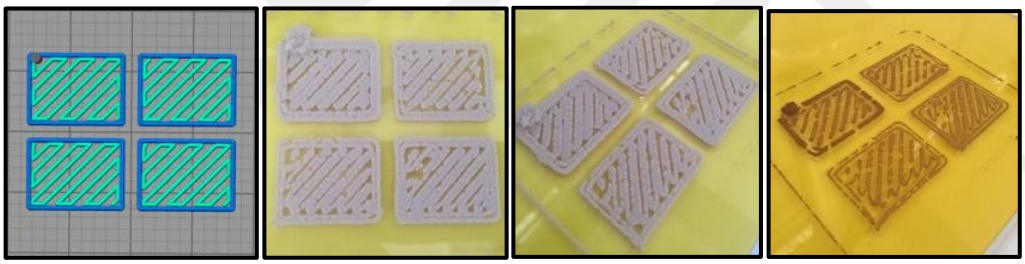


Figure 4.2 Print-preview and the model printed right after and after 24 hours of the printing process.

The preliminary experiments continued by printing the model shown in Figures 4.1 and 4.2 beyond the first layer and 15 layers were printed consecutively to observe if the layers could be stacked on top of each other to 3D print a self-supporting model. Water content of the hemicellulosic paste at this point was determined as 82% and the process was performed at room temperature. The visual appearance of the 3D printed model in this preliminary trial is shown in Figure 4.3. Although the first layer could not be printed properly as described before, the 3D printing process was completed without the collapse of the fifteen layers deposited on top of each other.

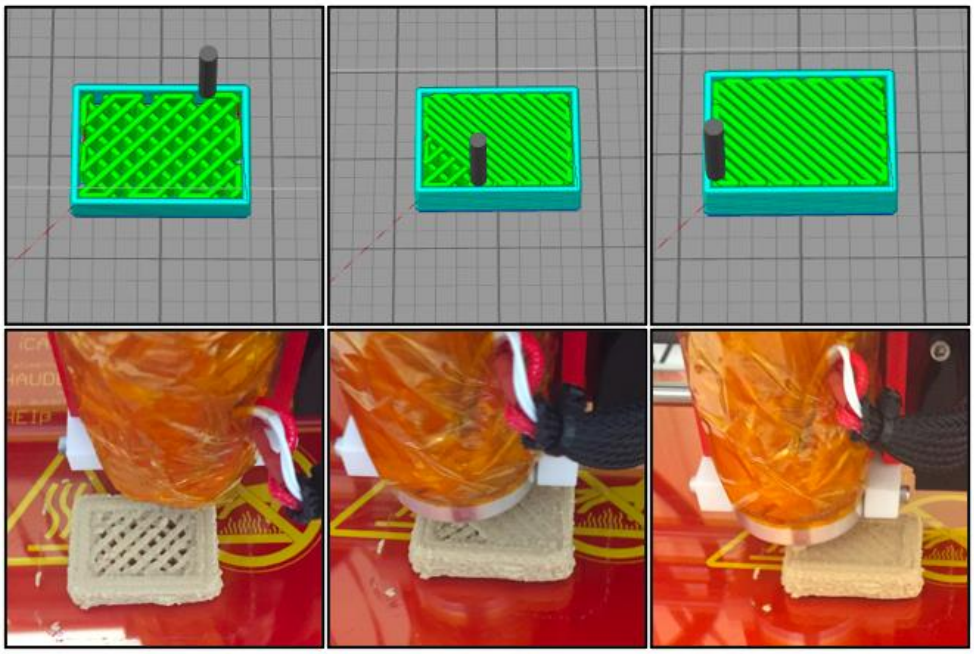


Figure 4.3 Print-preview and the actual printing process of 40 x 30 x 10 mm rectangular model.

Experimenting with settings related to the 3D printing parameters is essential to find the “sweet spot” for each printing process (Wang et al., 2017; Kearns et al., 2016). In this context, effect of one of the major printing parameters, printing speed, on the appearance of the printed model was investigated in more detail since it is one of the parameters that directly affects the quality of the finished parts produced via FDM 3D printers. It defines at which speed (controlled as mm/minute in Simplify3D) the print head moves during printing to form a complete object (Chai et al., 2017). Currently, FDM 3D printers are classified into four categories in terms of speed. The relatively slow ones can support printing speeds around 2400 mm/min to 4800 mm/min, the mid-speed ones can print around 6000 mm/min, the rapid ones can print as fast as 9000 mm/min, and the very fast ones may even print at speeds faster than 9000 mm/min. However, quality of the printed models drops dramatically at faster printing speeds.

In order to investigate the effect of printing speed on the resolution and smoothness of the printed structures, hemicellulosic biopolymer pastes with 80% water content

were printed at room temperature with seven different printing speeds. Effect of printing speed is investigated with respect to line resolution by printing square grid structures consisting of two crossing layers. 10 and 50 mm/min print speeds were found to be too slow to extrude the paste properly as illustrated in Figure 4.4. Inaccurate amount of material extruded per millimeter of printer head movement resulted in inconsistent extrusion. Furthermore, it took almost 40-50 minutes to print just two layers of the model, which was only 40 mm long, 13.4 mm tall and 40 mm wide with 50% infill percentage. Printing with 100, 1000 and 2000 mm/min printing speeds causes a roughness in the lines printed (Figure 4.4). Print head stays longer on the same spot compared to faster printing speeds and more pressure is applied to the unsolidified soft hemicellulosic paste causing an expansion and a roughness in the printed lines. This visual deformation is most clear in the model printed with 100 mm/min printing speed. It was observed that this reduction in visual quality is decreased by increasing the printing speed. Smoother lines could be printed with 3000 and 4000 mm/min printing speeds compared to slower printing speeds as shown in Figure 4.4. Based on these observations, it was obvious that the printing speed had a major influence on the smoothness and resolution of the printed models.

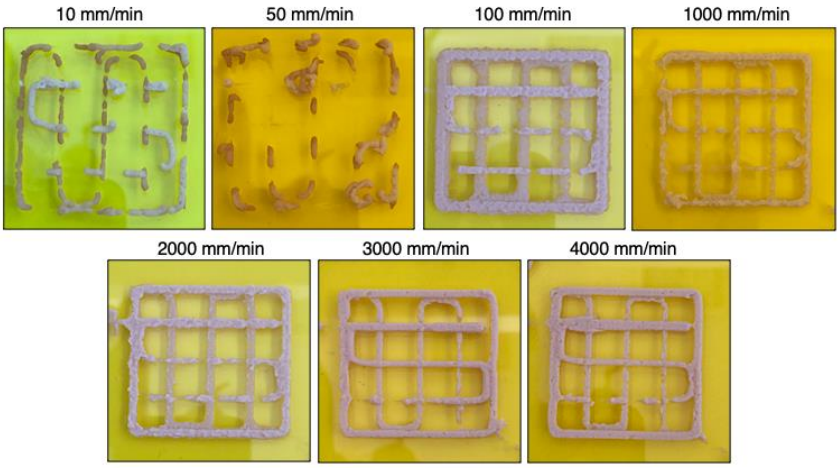


Figure 4.4 Printed grids of two crossing layers with seven different printing speeds. Images taken right after the printing process.

As mentioned before, successful printability necessitates homogeneous print materials to enable a consistent flow without clogging the nozzle during the printing process. In this context, sodium hyroxide was added to the extracted hemicellulosic portion to at least neutralize the paste, which tend to be in the acidic range at the end of alkaline extraction process because hemicellulose was precipitated from the alkaline solution with a solution of acetic acid and ethanol. It was observed that adding 1 wt.% NaOH solution right after the extraction process to hemicellulosic portion improved the homogeneity of the paste significantly.

In order to further investigate the effect of NaOH addition on the printability of the biopolymer paste, different concentrations of aqueus NaOH solution were added to the extracted hemicellulosic portion. One of the pastes was prepared by just adding the same amount of deionized water without any NaOH, as a control, to check whether NaOH had any effect on the homogeneity of the paste. The water content of the pastes in Figure 4.5 was around 78%.

It was observed through printed grids (Figure 4.5) that NaOH addition contributed to the homogeneity of the hemicellulosic paste. Among the sodium hydroxide additions tested, the lines printed with 5 wt.% NaOH solution additon were the smoothest ones.

Increasing NaOH concentration to 5 wt.% had a noticeable effect on the resolution of the printed lines as well. Lines of two crossing layers printed with the paste prepared by adding solely deionized water (without any NaOH) and by adding 1 wt.% NaOH solution are rougher compared to the lines printed with pastes containing more NaOH, as shown in Figure 4.5. Despite the increasing resolution of the printed lines with increasing NaOH content, minor imperfections were observed on the printed infill pattern. The reason for these minor imperfections is most likely related to the air bubbles stuck inside the hemicellulosic paste. The results presented in Figure 4.5 also show that considering the printing speed alone as a major determinant on the smoothness and resolution of the printed samples is not correct and printing speed should be considered together with the NaOH content of the

hemicellulosic pastes in order to have a more complete understanding of the overall process.

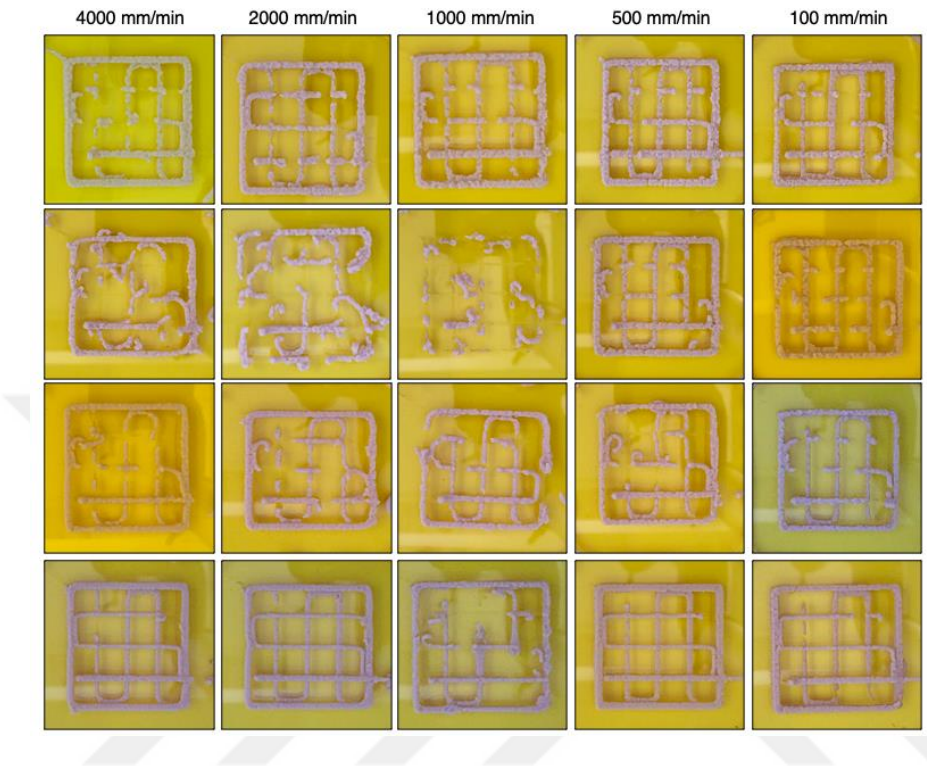


Figure 4.5 Printed grids of two crossing layers with 5 different printing speeds. Top to bottom: hemicellulose + DI water, hemicellulose + 1 wt.% NaOH solution, hemicellulose 2.5 wt.% NaOH solution, hemicellulose + 3 wt.% NaOH solution and hemicellulose + 5 wt.% NaOH solution. Images taken right after the 3D printing process (pastes contain 75-80% water content).

Printing materials with lower water contents enables avoiding the excess shrinking of the printed materials once they are dried, which is a case observed for the materials printed from hemicellulosic pastes with 80% water content at room temperature. In order to overcome this issue, printing the pastes at temperatures higher than room temperature was also studied and resulted to significant improvements regarding not only on the printability of the pastes but also on the appearances of the printed models.

3D printability of the paste with lower water contents was investigated by heating the paste, which was filled inside a polypropylene syringe with a heating coil around barrel in which the syringe was fitted into, during the 3D printing process. First two layers of the model which was 40 mm long and 40 mm wide were tried to be printed with the hemicellulosic paste containing 60% water content, which was reduced from 79%.

Heating the paste to 50ºC was found to be insufficient to make it extrudable from the nozzle of the syringe during printing process. Increasing EM value even to 3.00 at 70ºC was not sufficient to deposit the adequate amount of print material from the syringe. First two layers of the selected model could be printed when the print temperature was raised to 90ºC with an EM value of 1.50. Further increasing the EM value to 3.00 at 90ºC resulted to an over extrusion.

It was investigated whether adding NaOH solution at a higher concentration to the hemicellulosic paste would make the 3D printing of the paste containing lower water content possible at room temperature since NaOH addition had an impact on viscosity of the paste.

For this purpose, higher concentrations of NaOH solutions compared to those that were previously utilized, which contain 10 and 20 wt.% NaOH, were prepared. These NaOH solutions were then added to the hemicellulosic paste. By this way, two different pastes were obtained containing different amounts of NaOH with the same water content. These two pastes were compared with the paste containing 5 wt.% NaOH solution with the same water content in terms of their printability. However, once the three pastes were prepared, it is observed that the viscosity of the pastes containing 10 and 20 wt.% NaOH were too low to be printed at room temperature although the water content of the three pastes were the same. Therefore, instead of the polypropylene syringe, it was decided to produce a stainless-steel syringe for the 3D printer so that temperatures exceeding 100ºC could be applied to the hemicellulosic pastes.

4.2 Viscosity studies of the hemicellulosic pastes

Viscosity properties of the polymers is a key property for 3D printing. Complex and apparent viscosities of hemicellulosic pastes obtained from corn cobs were determined using oscillatory and capillary rheometers, respectively, so that the influence of temperature and water content on the viscosity can be characterized.

Complex viscosities of pastes with five different water contents, with and without NaOH addition, were determined using a parallel plate geometry. As shown in parts A and B of Figure 4.6, the pastes demonstrate a shear thinning behavior. This shear thinning behavior is particularly desirable when it comes to 3D printing of polymers (Paxton et al., 2017), and it shows that the pastes obtained from corn CCs have potential for 3D printing. Viscosity was found to increase as pastes lose their water content and it was extremely responsive to even very small changes in the water content. For example, reduction of water content from around 73% to 70% leads to an approximately 50% increase in the viscosity of the pastes containing NaOH (Figure 4.6A) and the increase in viscosity was almost 100% for the pastes that did not contain NaOH (Figure 4.6B). When the water content was reduced from 73% to around 62%, the viscosity was increased approximately by 4-fold (Figure 4.6A) and 6-fold (Figure 4.6B) for pastes with and without NaOH addition, respectively. These results also show that the addition of NaOH into the paste formulations makes the viscosity of the pastes less responsive to changes in water content when compared to pastes without NaOH. Results given in parts A and B of Figure 4.6 also show that the two pastes with and without NaOH show major differences in terms of viscosity.

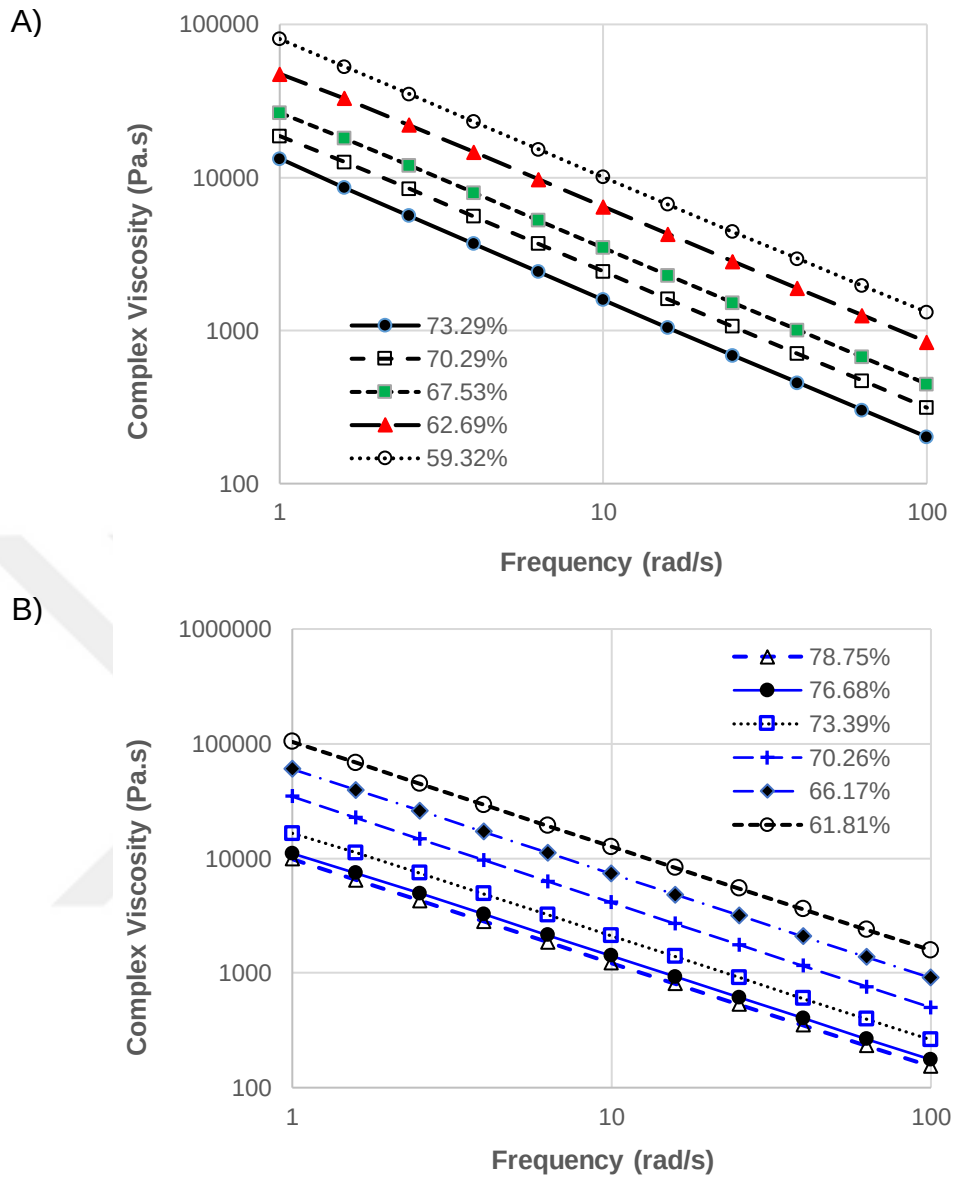


Figure 4.6 Parallel plate measurements of hemicellulosic pastes (A) with NaOH addition and (B) without NaOH addition at different water contents.

The power law model (Eq. 4.1) is widely used to represent the relationship between apparent viscosity and shear rate. The complex viscosity (η*) as a function of angular frequency (ω) can also be represented by the power law relationship (Eq. 4.2):

$$\eta_{app} = K\gamma^{n} \qquad (4.1)$$

$$\eta^{*} = K'\omega^{n'} \qquad (4.2)$$

Here K′ can be considered as the flow consistency index and n′ as the flow behavior index. The value of n′ for the pastes is nearly independent of the water content of pastes and was determined as 0.1. The value of n did not change significantly for the pastes with different water contents. As a result, the influence of water content can be described through K value.

The following empirical equation was used to represent the influence of water content on the complex viscosities of the pastes.

$$K=f(H_2O\%) = A.\exp(B.(H_2O\%)) \quad (4.3)$$

Then, the complex modulus as a function of both water content and angular frequency can be represented by the following equation.

$$\eta^* = A.\exp(B.H_2O\%)).\ \omega^{(n-1)} \quad (4.4)$$

The flow consistency index values as a function of the water content of the pastes are given in Figure 4.7. As shown in Figure 4.7, for the same water content, K′ values of the pastes without NaOH are higher than that of the pastes with NaOH, suggesting that the complex viscosity of the pastes without NaOH is higher than that of the pastes with NaOH.

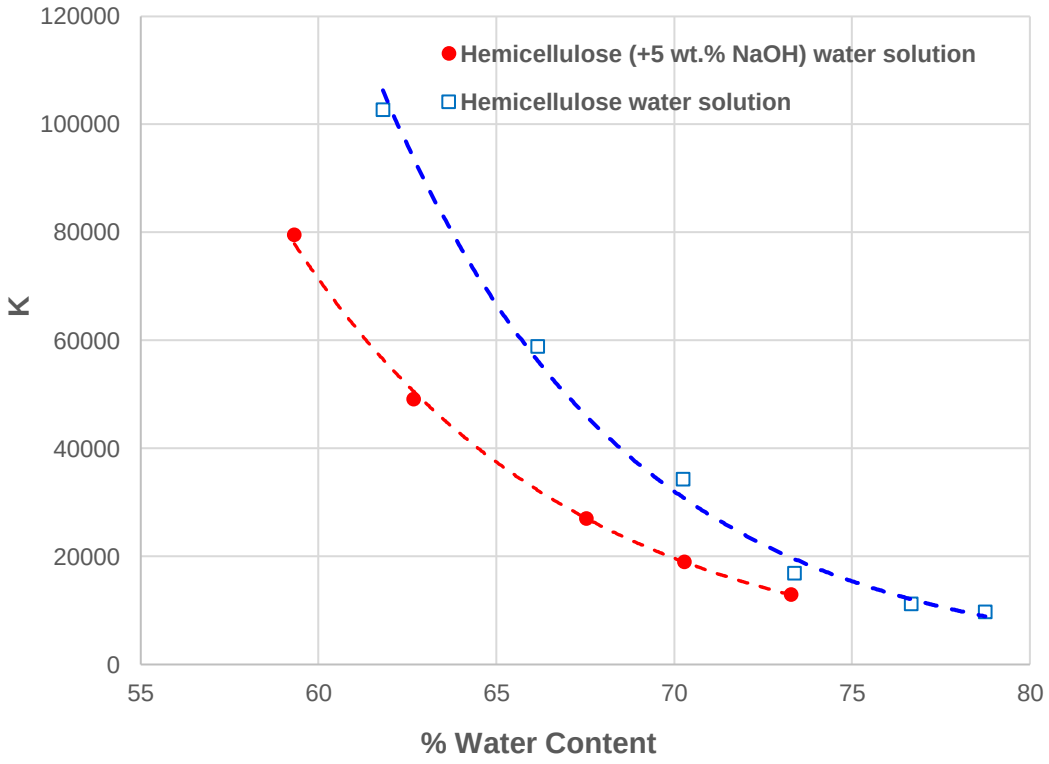


Figure 4.7 K value as a function of water content for the hemicellulosic paste with and without 5% NaOH solution.

Results given in Figure 4.6 also show that the two pastes with and without NaOH show major differences in terms of viscosity. For the same water content, the complex viscosity of NaOH containing paste is around 1.7 times lower than that of the paste without NaOH. Therefore, adding NaOH solution to hemicellulosic pastes was found to reduce their viscosity. This behavior in viscosity might be attributed to the higher solubility of hemicelluloses in basic conditions.

Changes in the viscosity of hemicellulosic pastes with respect to temperature were also investigated by parallel plate rheometer measurements (Figure 4.8). Heating the hemicellulosic paste from room temperature to 80°C reduced the viscosity of the paste by roughly 4-fold. For each 10°C increase between 60, 70, and 80°C, which were also the temperatures where 3D printing of the hemicellulosic pastes were performed, the viscosity was decreased by around 1.5-fold, showing the viscosity of

the hemicellulosic pastes were not only very responsive to changes in the water content but also to the changes in temperature.

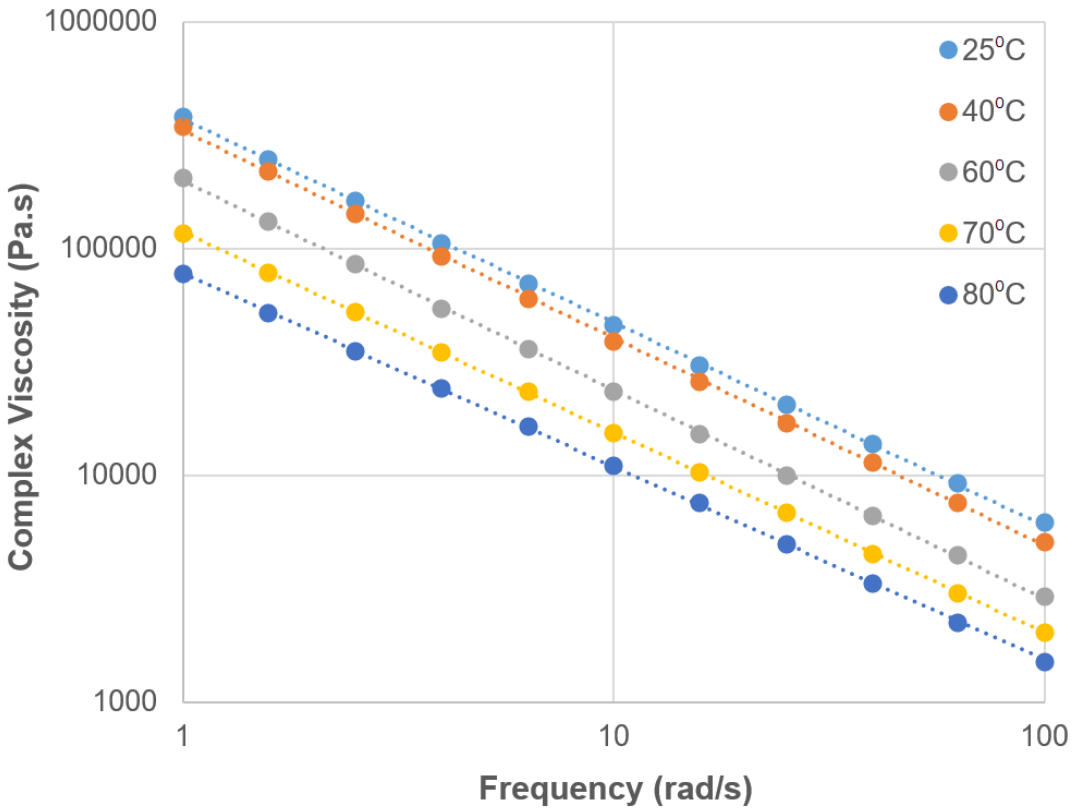


Figure 4.8 Effect of temperature on viscosity of the hemicellulosic paste containing 1 wt.% NaOH solution.

The complex viscosity results may not be relevant to 3D printing process since the pastes were subjected to a very small oscillatory strain (0.5%) during the oscillatory measurements. Therefore, the apparent viscosities of the pastes as a function of shear rate using a capillary rheometer were also measured at five different temperatures ranging from 60 to 80°C. The apparent viscosities of the pastes with different water contents and at different temperatures are shown in Figure 4.9. The power law model was used to represent the apparent viscosity (η_{app}) versus shear rate data. The value of flow behavior index (n), which was nearly independent of water content and temperature, was calculated as 0.41, which is 4 times higher than the value of n′ from

the oscillatory measurements. It appears that it was not possible to relate the complex viscosity as a function of angular frequency to the apparent viscosity as a function of shear rate using the Cox−Merz or modified Cox−Merz relationships (Eq. 4.5 and Eq. 4.6).

$$\eta^*(\omega) = \eta_{app}(\gamma)_{\omega=\gamma} \quad \text{Cox} - \text{Merz rule} \tag{4.5}$$

$$\eta^*(\omega.\alpha) = \eta_{app}(\gamma)_{\omega=\gamma} \quad \text{modified Cox} - \text{Merz rule} \tag{4.6}$$

Here, α is the shift factor.

Since the apparent viscosity values are relevant to 3D printing process, the viscosity of the pastes should be measured using the capillary rheometer. Because it is faster and easier to obtain complex viscosity results, the oscillatory measurements were also used to establish the relationship between water content, temperature and NaOH addition.

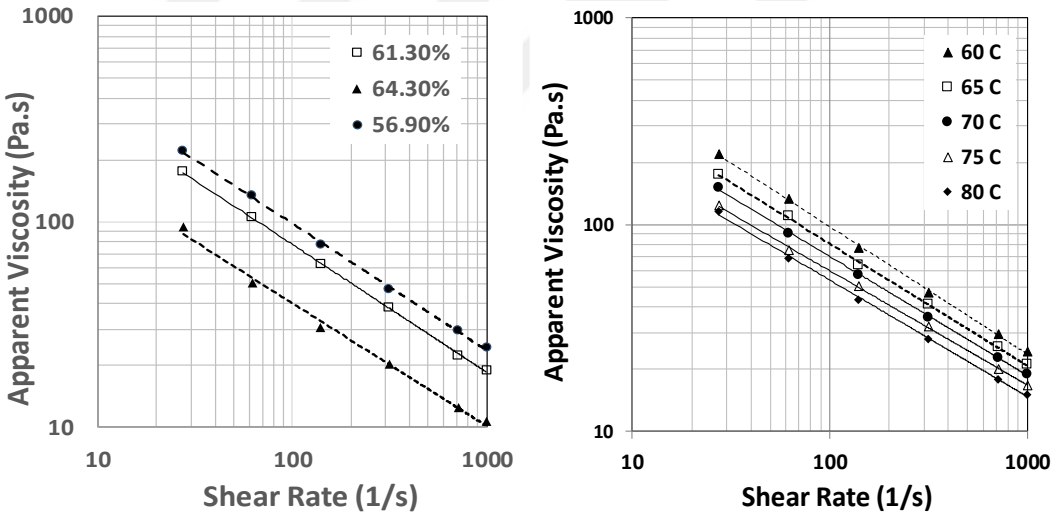


Figure 4.9 Influence of water content on the apparent viscosity of hemicellulosic pastes at 60°C and influence of temperature on the apparent viscosity of hemicellulosic pastes with a water content of 57%.

3D printing processes involving nanocellulose containing hydrogel inks typically suffer from low viscosity values, which create problems related to structural

integrity, leading to extra post printing steps and utilization of supporting polymers (Chinga-Carrasco, 2018; Fukuzumi et al., 2013; Chinga-Carrasco et al., 2011; Moberg et al., 2017). Related to 3D printing, the viscosity results given are important since they show that the viscosities of pastes can easily be adjusted by changing water content and temperature unlike the case with nanocellulose inks, which makes the current hemicellulose-based printing process more flexible compared to nanocellulose based processes. Since the viscosities of the hemicellulosic pastes used in this study are considerably higher than those of the hydrogel inks, there is no lower limit in viscosity and the upper limit is related to the printing setup. At 80°C the viscosity of the pastes is sufficiently low so that the paste can be printed using the printer with the existing stepper motor. If a stronger stepper motor is used, it would be possible to print pastes at lower temperatures or at lower water contents.

4.3 Effect of water content and process parameters on 3D printability of hemicellulosic pastes

Following the preliminary experiments and findings related to water and NaOH contents of hemicellulosic pastes together with the effect of temperature on paste viscosity and flow, a new series of experiments were designed and performed with different printing temperatures, water contents and EMs. The results of these experiments were used to determine the 3D printability window for hemicellulosic pastes obtained from CCs. These new series of experiments were performed with a stainless-steel syringe, which was manufactured according to the specifications of our research group, instead of the polypropylene one used in the earlier experiments since the hemicellulosic paste inside the stainless-steel syringe can be heated in a much more effective way due to the conductivity of the metal. Making consecutive experiments that involve temperatures close to 100°C were also more feasible by using a metal syringe instead of a polypropylene one. The stainless-steel syringe also came with several interchangeable nozzles that had different inner diameters.

As shown in Figure 4.10, hemicellulosic pastes with a water content of 62% at two different temperatures (60°C and 70°C) were printed at 4 different extrusion multipliers (EMs) as one-layered grid structures were printed. At 60°C printing temperature, paste deposition could not be achieved most likely due to the very high viscosity of the paste. Increasing the printing temperature to 70°C enabled some paste deposition when the EM was set at least to 1.25.

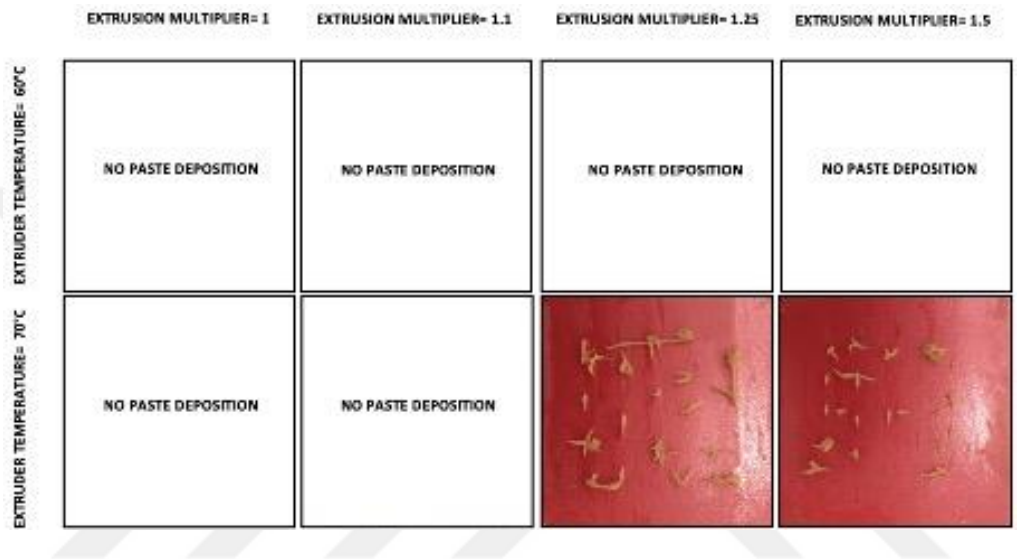


Figure 4.10 3D printing of hemicellulosic paste with 62% water content at different temperatures.

As shown in Figure 4.11, increasing the water content of the pastes from 62% to 65% enabled more paste deposition to be achieved when the extrusion temperature was set as 70°C. It was possible to print a structure close the intended model at 70°C at EM value of 1.25.

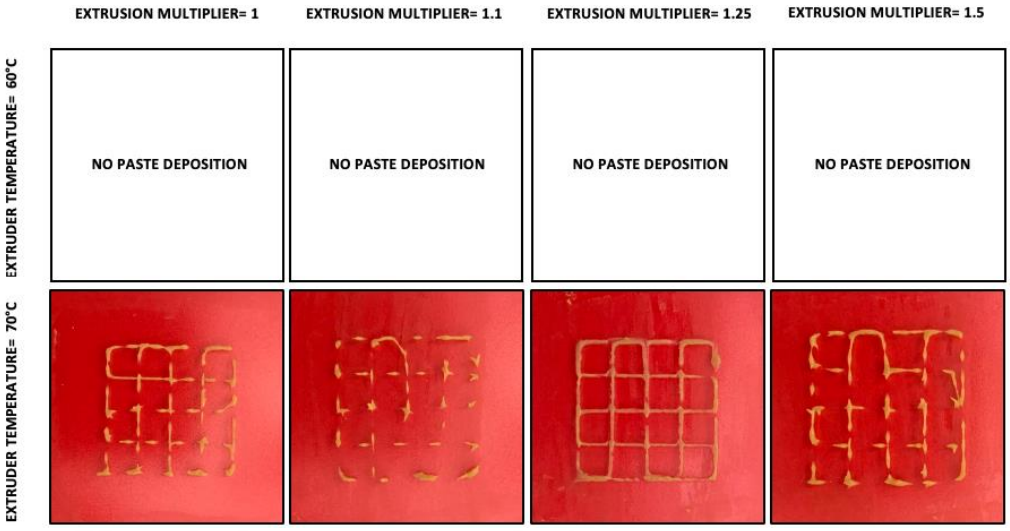


Figure 4.11 3D printing of hemicellulosic paste with 65% water content.

Appearance of the printed models obtained from hemicellulosic paste with a water content of 68% are shown in Figure 4.12. Unlike the previous trials performed with lower water contents, this time the paste could be deposited at the temperatures tested but the deposited material was insufficient to create continuous lines and hence to print the model properly.

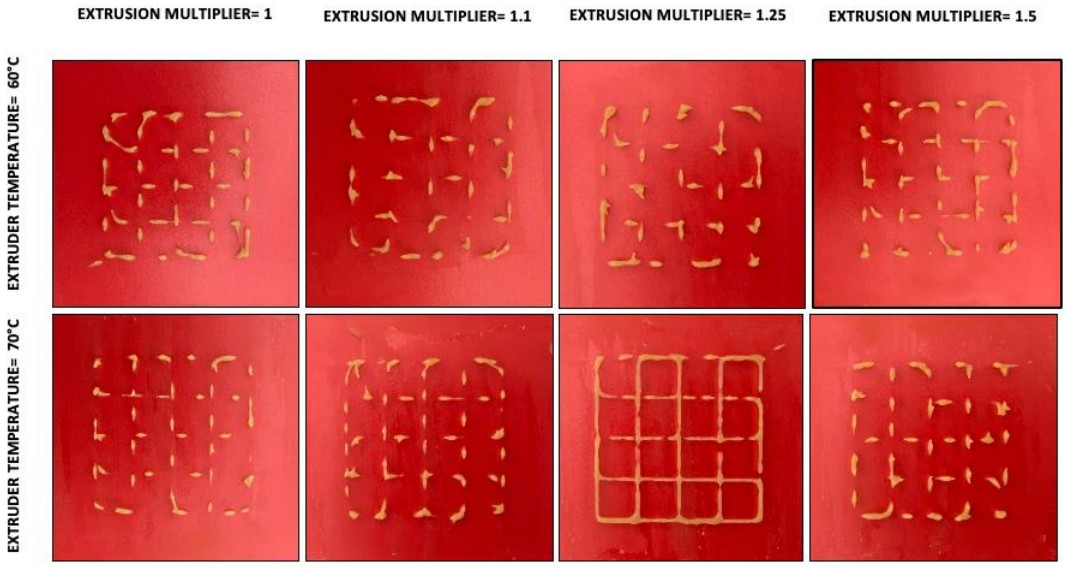


Figure 4.12 3D printing of hemicellulosic paste with 68% water content.

Based on these results obtained from the printing of a one layered model, a water content range between 60% and 70% was chosen for the hemicellulosic pastes to be printed since below a water content of 60% paste deposition could not be obtained while at water contents close to or above 70% the paste flow was observed to be inconsistent and discontinuous. Hemicellulosic pastes to be printed in three layered structures were thus prepared at three water contents, which were around 62%, 65% and 68%. All the pastes were printed at a higher temperature of 80°C as previously tested printing temperatures (60°C and 70°C) were not sufficient to create a continuous flow of material. For three-layered models, as shown in Figure 4.13, successful deposition of the paste could not be obtained at a water content of 62% for EM values between 1 and 1.5. EM was further increased to 3 to see if steady deposition of the paste could be achieved in this case and indeed a model structure consisting of 3 layers could be obtained for the first time at this quite high EM value as shown in Figure 4.13. Although the model could be 3D printed in this case, it is apparent from the line thickness values that the lines of the model were significantly thicker than intended. The inner diameter of the nozzle of the 3D printer in which the hemicellulosic paste is deposited is 0.68 mm while the average line thickness of the printed model was determined as 1.35 mm indicating the printing parameters employed were not ideal. EM is simply related to the amount of the material that flows (or intended to flow) from the printer nozzle (in this case the tip of the syringe) and thus changing EM modifies the amount of the polymer deposited. At this point it is worth noting that an EM setting of 3 is rather unconventional in terms of general 3D printing practices where this setting is generally taken around 1 for standard popular 3D printing polymers such as ABS and PLA.

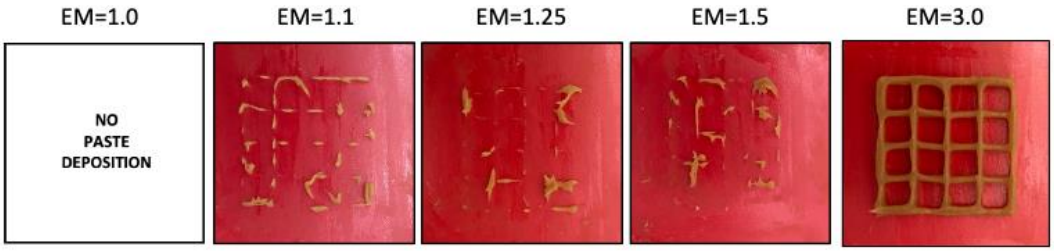


Figure 4.13 Hemicellulosic pastes with a water content of 62% printed at 80°C at five different EM values.

The water content of the hemicellulosic paste was increased to 65% from 62% in order to investigate if it could be possible to print the models at EM values less than 3, which could lead to line thicknesses closer to the intended values. Compared to the case where the pastes had 62% water content, a water content of 65% enables more paste to be deposited onto the build platform for the EM values of 1, 1.1 and 1.25 as shown in Figure 4.14A. However, the printed models were not intact or as it was the case for when EM was set to 1.25, they had significant defects. It was possible to successfully print the model when EM was set to 1.5 as shown in Figure 4.14A where the average line thickness value (0.74 mm) was much thinner compared to the previous case when the water content was lower. The small difference between the line thickness and the inner nozzle diameter is expected and acceptable since some expansion of the paste as it comes out of the nozzle during the printing process is inevitable because of the pressure build up inside the syringe's barrel. The same paste was also printed with an EM value of 2 to observe the impact of EM where again a successful printing of the model could be obtained this time with an average line thickness of 0.94 mm.

The printing of the hemicellulosic pastes was also performed by further increasing the water content from 65% to 68%. The paste could be deposited at all the EM values tested (namely for EM=1, 1.1, 1.25 and 1.5) as shown in Figure 4.14B. However, when the printed models were inspected it was observed that the upper layers of the models, which consisted of three layers in total, had significant defects in the form of spike like structures for all the EM values between 1 and 1.5. The most

likely reason for this was the increased stickiness of the pastes with increasing water content. As the paste was deposited onto the first layer during the printing of the second layer of the model, the deposited paste dragged some of the previously deposited paste since the paste was also partially adhered to the nozzle as the nozzle was moving during the printing process. When EM was set to 2, the spike like defects were not observed and a smooth model could be obtained most likely due to the higher material flow rate from the nozzle which prevented the dragging action.

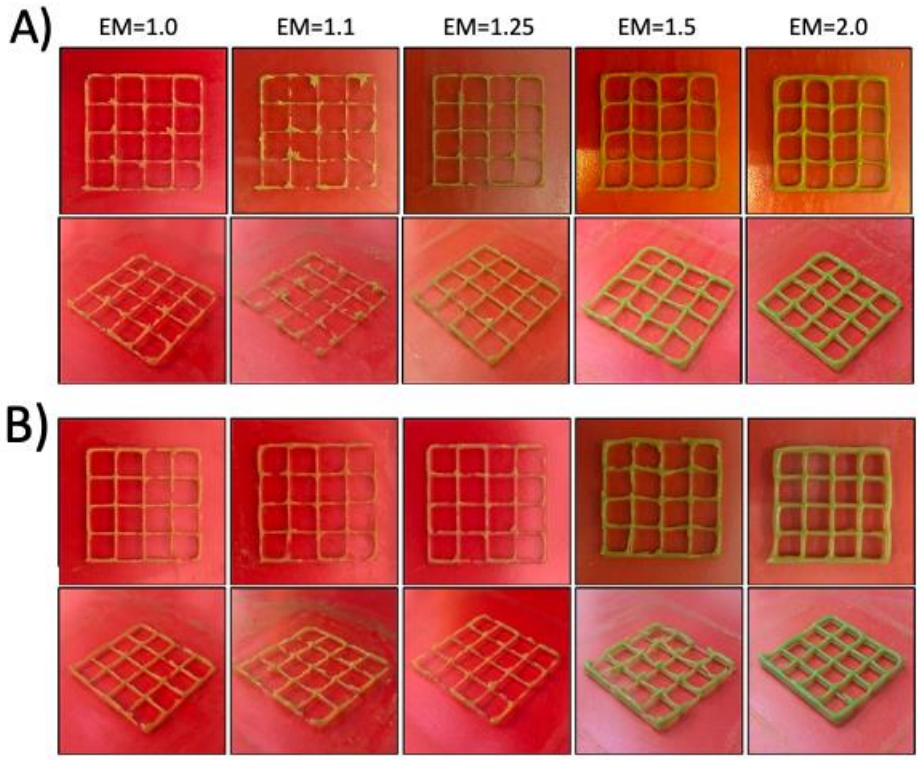


Figure 4.14 Appearance of three-layered models printed from hemicellulosic pastes with a water content of 65% (A) and 68% (B) at 80°C by using five different EM values between 1.0–2.0.

The results given so far include printing temperatures up to 80°C where a trial with a printing temperature of 90°C was also performed. When the temperature was raised above 80°C, successful deposition of the paste could not be achieved. As shown in Figure 4.15, when the printing temperature was set as 90°C, due to the buildup of excessive vapor pressure inside the syringe, more material than intended was

deposited on to the build platform, resulting in a model with defective and significantly thicker lines. As the vapor pressure at this temperature disrupted the flow of the material, paste also leaked from the joint in which the nozzle was attached to the barrel of the stainless steel syringe.



Figure 4.15 3D printing of hemicellulosic paste at 90°C.

Effect of drying on the shape of the printed grid structures was also investigated by drying the three-layered grid structure printed at 80°C with an EM of 1 by using a paste with 55% water content. As shown in Figure 4.16, the integrity of the structure was retained following drying at room temperature for 24 hours where all the cells that makeup the grid structure also retained their original shapes.



Figure 4.16 Appearance of three-layered grid structure upon drying.

The hemicellulosic paste was also used to print a hollow cube with the so-called vase mode. This model consisted of 15 layers built on top of each other with a height of 1 cm where each side of the model was 2 cm wide. A hemicellulosic paste with a

water content of 68% was used for this experiment. As shown in Figure 4.17, there was sufficient layer adhesion, and the material could sustain its own weight as it could stand on its own without collapsing. Following the printing process, the model was left to dry for 24 hours at room temperature. Although there were no cracks or defects on the printed model following drying, the model shrunk at the end of drying period. The shrinkage at the base of the model was minimum due to the very good adhesion of the printed model's first layer to the printing bed, which was made from glass. The shrinkage was most significant at the upper opening of the model where each of the edges was shrunk by 35% compared to their initial lengths and the area of the upper opening was shrunk by 58%. The height of the model was also shrunk by 60%.

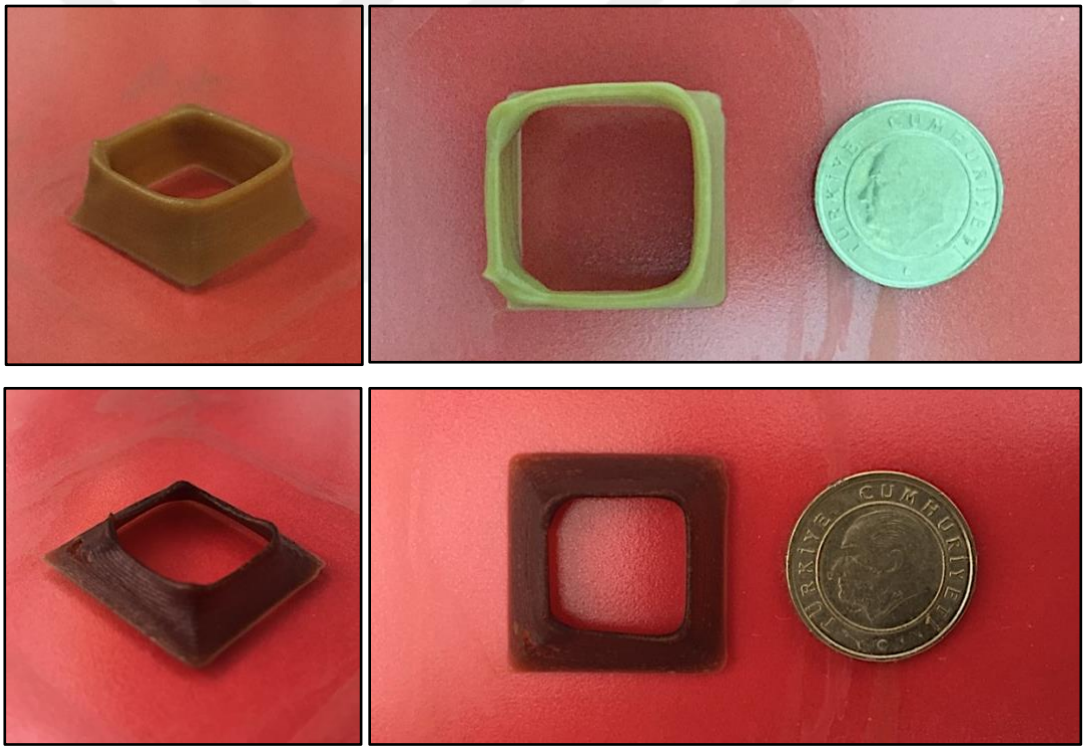


Figure 4.17 A hollow cube printed from hemicellulosic paste and its appearance upon drying.

Since the shrinkage observed in the hollow cube was uneven, the final shape of the model became somewhat different compared to the originally intended one when the

printed model was dried. In order to solve this problem, the glass build platform was covered with paper which was then covered by a polymer stretch film and the model was printed on to this polymer film rather than on the glass surface. Once the printing was complete, the polymer film below the model in which the model was printed upon was cut (together with the paper below it) and removed together with the model to a separate location. This way the uneven shrinkage that distorted the overall shape of the model was prevented since the bottom part of the model was also allowed to shrink as much as the top part of the model thanks to the presence of the polymer stretch film and the model still had a cubic structure after drying as shown in Figure 4.18 where all three dimensions of the model shrunk evenly this time by 25%.



Figure 4.18 A hollow cube printed from hemicellulosic paste and its appearance upon drying. Appearance of the hollow cube right after the printing process while it was wet (top row) and after drying at ambient conditions for 24 h (bottom row).

Based on the observations made on the hollow cube, a 3D daisy figure was also printed from hemicellulosic paste with an EM of 1.5. As shown in Figure 4.19, unlike the hollow cube the shrinkage was minimal with this figure since it was also printed on the polymer stretch film rather than the glass surface.



Figure 4.19 A 3D daisy figure printed from hemicellulosic paste.

It is worth noting that during the 3D printing of all the hemicellulosic pastes with different water contents, layer height was also a major concern. In conventional 3D printing processes, layer height is generally taken as half of the nozzle diameter as a rule of thumb. When this was also applied in the current case, because of the expansion of the hemicellulosic paste as it comes out of the nozzle, the increment of the nozzle when it built each new layer was insufficient and the tip built the upper new layer partially inside the lower one, creating a dimensional instability that appeared as a defect. Because of this issue, the layer height value was first increased to 75% of the nozzle diameter, which again did not provide sufficient height for the new layer to be deposited properly, and then finally to the same value as the tip diameter (0.68 mm), which was finally sufficient for the new layers to be printed properly on top of the lower ones.

Considering the printing results obtained with hemicellulosic pastes it appears that there is a very narrow window in terms of their printability regarding the parameters associated with the hemicellulosic paste as well as the printing process itself. Very small changes in the water contents of the pastes had dramatic impacts on the printability of the hemicellulosic polymers, which is directly reflected to the way the polymers are deposited during the printing process, affecting the structure of the printed models. Presence of adequate amounts of NaOH in the hemicellulosic paste formulation was also necessary for the smooth and continuous printing of the hemicellulosic paste as well.

A quantitative analysis of the 3D printed models might also be helpful in order to assess the printability of the hemicellulosic pastes with respect to different parameters. A previous approach taken to quantitatively analyze the printability of the pastes was to determine a so-called "target area" for the square cells inside the models and to compare it with the actual areas obtained at the end of the printing process as demonstrated by Liu et al. (2019) for the printability evaluation of carrageenan-xanthan-starch gel systems. Some of the printed grid models were chosen in order to investigate if this approach could also be used in the present study so that the printability of hemicellulosic pastes could be evaluated quantitatively. As shown in Table 4.1, models printed from the pastes having a water content of 65% with an EM of 1.5 gave the highest cell area and eventually the highest % target area, which shows the percent realization of the cell area that would be obtained provided that the most ideal conditions were met (perfect square with the line thicknesses identical to the nozzle diameter, which is 0.68 mm, giving an area of 34.7 mm^2) was calculated as 87%. The second highest % target area value among the 4 models analyzed was obtained again from the pastes having a water content of 65%, this time with an EM of 2, implying that this water content was more ideal for the 3D printing of hemicellulosic pastes compared to the paste water contents of 62% and 68%, which both gave % target area values of around 72.5%.

Table 4.1 Printability, cell area and % target area values for models printed at different EMs and printing speeds at 80°C.

3D printing parameters (Water content of hemicellulosic paste – EM)	*Average area of a single cell (mm^2)*	*% Target (Ideal) Area*	*Printability*
62%- 3.0	25.15 ± 1.68	72.5	0.90 ± 0.02
65%- 1.5	30.20 ± 1.72	87.0	0.89 ± 0.02
65%- 2.0	27.34 ± 1.74	78.8	0.88 ± 0.02
68%- 2.0	25.15 ± 1.35	72.5	0.92 ± 0.02

In addition to % target area, another approach for the quantitative analysis of the 3D printed models might be to determine a printability value as demonstrated by Ouyang et al. (2016) for bioinks based on gelatin and alginic acid sodium salts in which the printability value represents the squareness of the cells inside the printed model. Printability values between 0.9 and 1.1 represent the printable range according to Ouyang et al. (2016). Image analysis of each one of the 16 cells in each successfully printed model was performed to calculate the necessary printability values. As shown in Table 4.1, all 4 models had very similar and adequate printability values between 0.88 – 0.92 regarding the squareness of the cells inside the model. It is also important to note that not only the printability value, but also the %target area value should be considered when evaluating the optimal printing parameters for a given material since although all the models had very similar printability values, the % target area values were different from each other.

4.4 3D printing of a scaffold prototype

Following the findings related to the formulation of hemicellulosic pastes with respect to their water and NaOH contents, effect of temperature on paste viscosity and flow and the effect of EM values on 3D printability presented in the previous sections, a series of experiments were performed with different printing temperatures, water contents and EMs. The results of these experiments were used to determine the printability window in order to construct scaffold prototypes from hemicellulosic pastes. As shown in Figure 4.20, three-layered grid structures this time consisting of 64 cells were printed with the hemicellulosic paste with a water content of 62% at three different printing speeds (100, 500 and 1000 mm/min) and at an EM of 1.25. It is worth noting that this model is much more challenging to print compared to the previous grid models since it contains 64 cells instead of 16 fitted inside a much smaller area where each side of the scaffold model is around 50% shorter compared to the previously printed grid models. In addition to fitting a higher number of cells inside a smaller area, scaffold model also has more layers compared

to the previously printed 16 cell grid models, which makes the 3D printing of the scaffold model even more challenging. Therefore, this new design needs its own unique set of printing parameters so that it can be 3D printed properly.

It was found that 500 and 1000 mm/min printing speed values were too high to print this model properly as shown in Figure 4.20A. On the other hand, increasing the material extruded by increasing the EM from 1.25 to 1.5 resulted in completely closed cells as shown in Figure 4.20B.

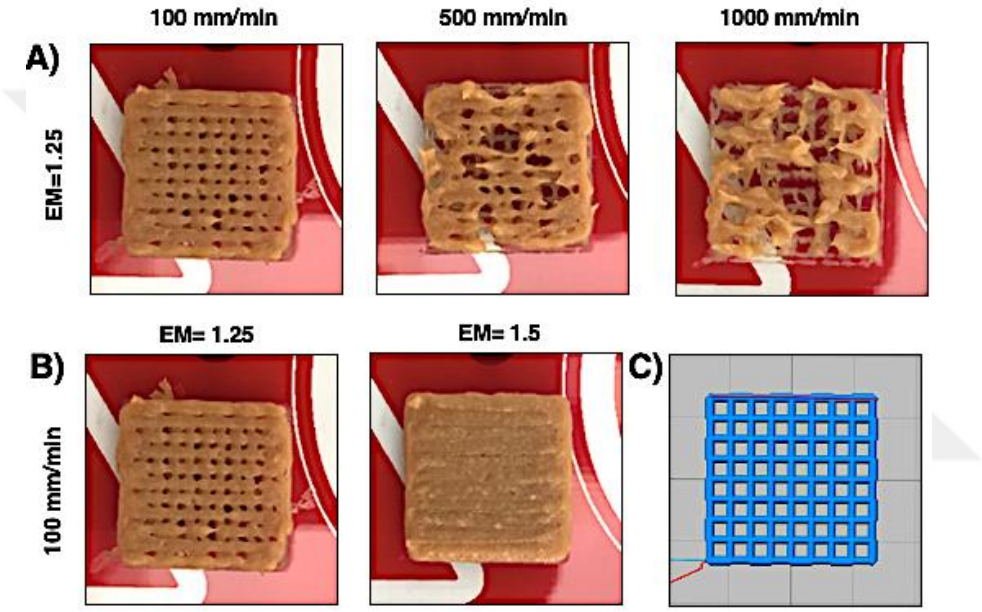


Figure 4.20 3D printing of three-layered scaffold prototypes with intended dimensions of 15 mm x 15 mm x 2.43 mm from hemicellulosic paste with 62% water content. Scaffold prototypes printed at (A) three different printing speeds with an EM value of 1.25, (B) two different EM values at 100 mm/min printing speed (C) Top print preview of designed scaffold prototype.

In order to obtain a scaffold prototype containing cells that are more clearly separated from each other, printing speed was increased from 100 mm/min to 300 mm/min in an EM range of 1.0–1.5 as shown in Figure 4.21. The change in printing speed and EM values enabled to obtain a structure closer to the originally designed one for 300 mm/min printing speed at 1.0–1.25 EM values as shown in Figure 4.21A.

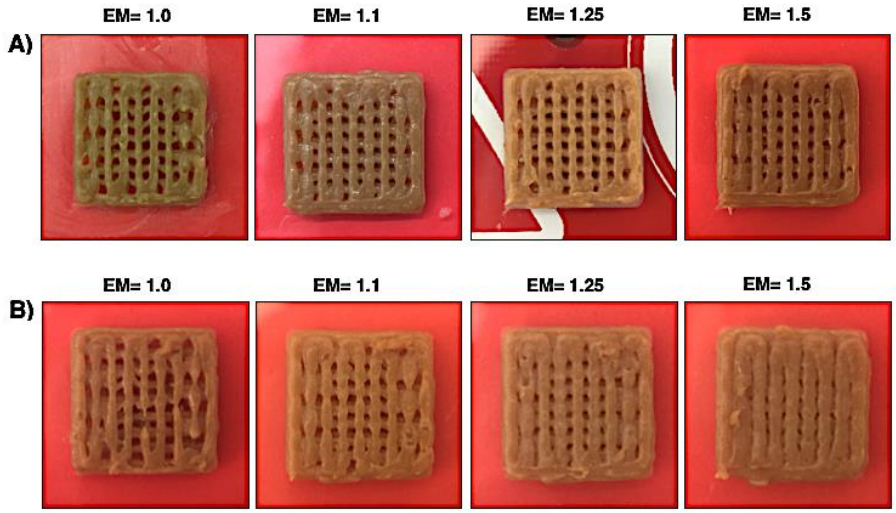


Figure 4.21 Three-layered scaffold prototypes printed at (A) 300 mm/min and (B) 100 mm/min printing speed in 1.0-1.5 EM value ranges.

Printing process of the scaffold structure's first layer was also shown together with the appearance of the completed scaffold prototype in Figure 4.22A. The prototype was printed with the printing parameters that gave better results previously. It was also observed that the aperture of the cells decreased after the deposition of the first layer as the upcoming layers were constructed on top of one another. Figure 4.22B shows the three-layered scaffold prototype printed at 300 mm/min with an EM of 1.1 while Figure 4.22C shows the scaffold prototype after drying at room temperature for 24 hours.

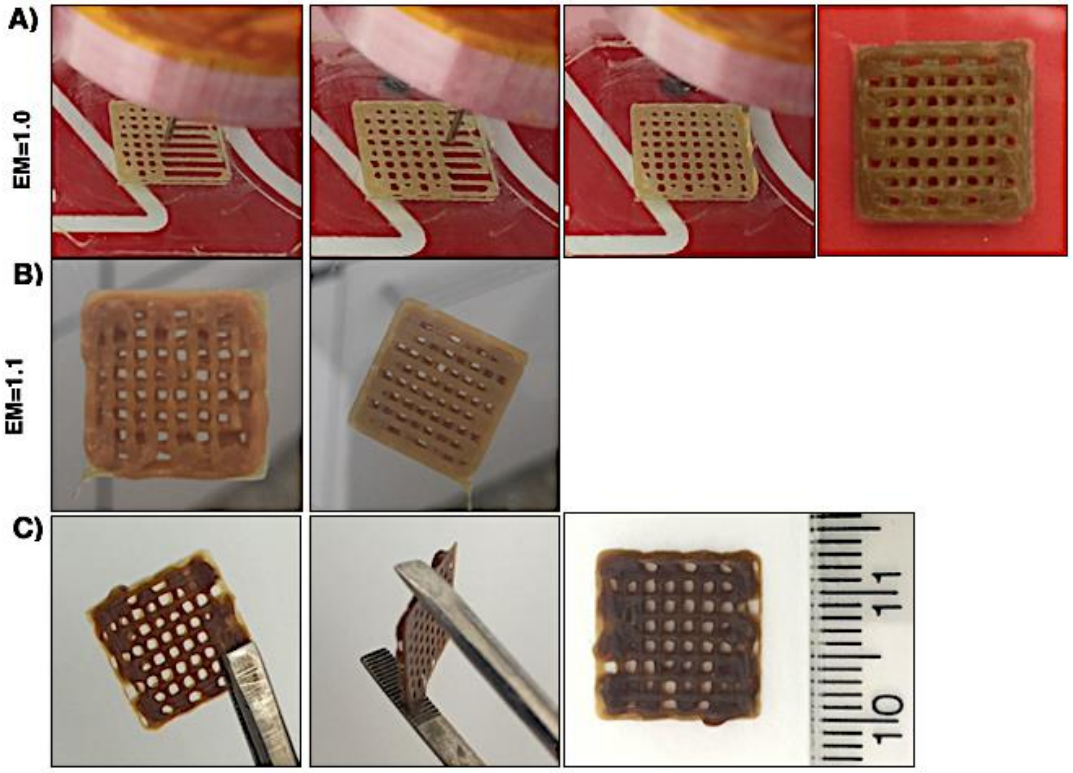


Figure 4.22 Three-layered scaffold prototype printed at 300 mm/min and a layer height of 0.81 mm. Printing with (A) 1.0 and (B) 1.1 EM values. Appearance of scaffold prototype upon drying (C).

Scaffold prototypes were also printed at 60°C instead of 80°C in order to see if there was going to be less expansion of the paste as it comes out of the nozzle so that the aperture of the cells can be increased, getting closer to the intended (original) dimensions. In order to 3D print the hemicellulosic paste at this temperature, water content of the paste was increased to reduce its viscosity. Figure 4.23 shows the three-layered scaffold prototypes printed at 60°C and at 300 mm/min printing speed with five different layer heights. All the other printing parameters were the same with the parameters used to print the structure shown in Figure 4.22A.

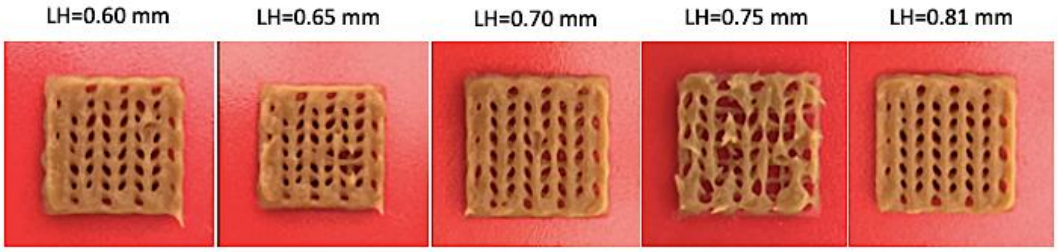


Figure 4.23 Three-layered scaffold prototype printed with five different layer heights (LH) at 300 mm/min printing speed and 60°C.

Encouraging result could not be obtained upon changing the printing temperature. Increasing water content of the paste was disadvantageous when it came to printing scaffolds containing 64 cells since there was little room for the nozzle to move precisely to form the cells of the scaffold successfully with sufficient resolution. Increasing the water content was also problematic regarding the changes applied in the layer height setting of the 3D printing process. Increasing the water content made the paste softer and the paste which was being deposited from the tip also dragged away the paste already deposited in the previous layer, which eventually led to the formation of undesired cell shapes with diagonal sides as shown in Figure 4.23.

Various changes were made to the 3D printing process to resolve the issues related to the successful printing of the scaffold prototype. In order to solve the stickiness problem of the paste that leads to defects, the printing process performed at a lower content of 62% and a higher temperature of 80°C compared to the previous trial. The nozzle diameter was also reduced from 0.68 mm to 0.54 to achieve a better resolution, which was expected to give a better aperture for the cells. The nozzle with an inner diameter of 0.54 was the smallest nozzle available following the nozzle with a diameter of 0.68 mm. Finally, the number of cells inside the model was reduced to 36 from 64. This way, it was possible to print three-layered and also ten-layered scaffold prototypes. Figure 4.24A and Figure 4.24C show the print preview of three-layered and ten-layered scaffold prototypes while wet and dry 3D printed scaffolds prototypes are shown in Figure 4.24B and Figure 4.24D.

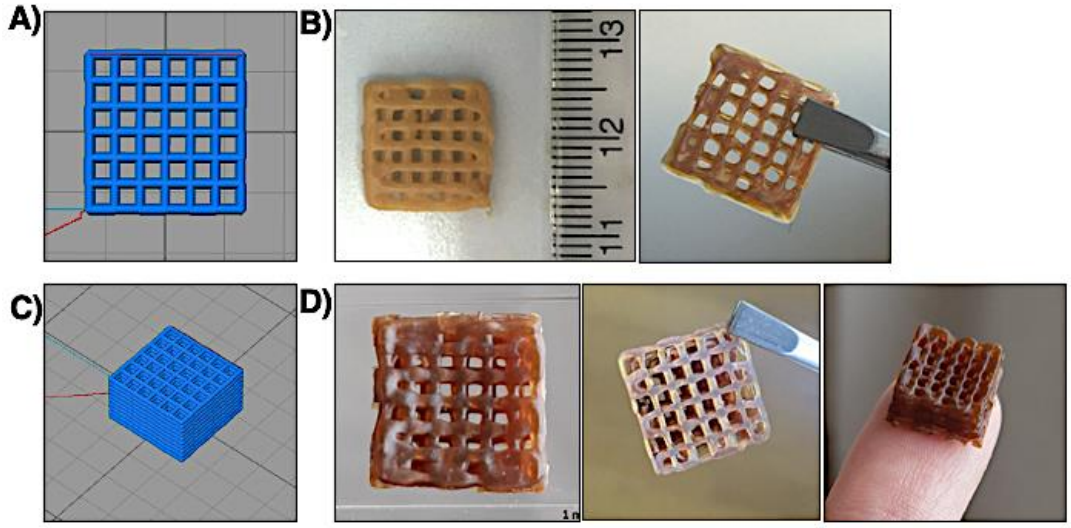


Figure 4.24 (A) Top print preview of designed three-layered scaffold prototype. (B) Appearance of 3D printed three-layered scaffold prototype right after the printing process and after drying at ambient conditions for 24 h (C) Print preview of designed ten-layered scaffold prototype. (D) Appearance of 3D printed ten-layered scaffold prototype after drying at ambient conditions for 24 h.

Any crack formation or defects in the printed model due to drying was not observed. However, the model was found to shrunk by retaining its proportionality (Figure 4.24B). The scaffold prototype shown in Figure 4.24D is 10.5 mm on the sides, and it is 5.3 mm long. The very small cells obtained in this scaffold had dimensions of about 0.84 mm on each side, which continue throughout the ten successive layers in the middle region of the model. The cells located on the edges of the model appears to be blocked due the irregularities created by the successive movement of the nozzle on the sides during the printing process. The interlayer stickiness results in the newly deposited paste to drag the paste on the layer below it, leading to the mentioned irregularity. Scaffold's volume was found to shrunk by 53% upon drying at room temperature. The volume decrease was found to be smaller than original water content of the hemicellulosic paste used to print the scaffold which, was 62%. This shows that some water was retained in the 3D printed scaffold as expected. This also indicates that the water content of the hemicellulosic paste used to print the scaffold

can be used to tailor its porosity if freeze-drying can be applied to the 3D printed scaffolds instead of conventional drying. The original dimensions of the printed model might also be preserved via the application of freeze-drying method.

4.5 The mechanical properties of 3D printed models from hemicellulosic pastes

Dog bone shaped specimens were printed from hemicellulosic pastes to investigate the mechanical properties of the models via tensile testing. The build direction of dog bone shaped specimens was adjusted to be parallel to the tensile testing direction as the mechanical properties of 3D printed materials are known to be dependent on the direction of the applied force during testing. Mechanical properties of 3D-printed hemicellulosic specimens are given in Table 4.2. Solvent cast and extruded specimens, which were also obtained from hemicellulosic fractions alkaline extracted from CCs were also included in Table 4.2 to make a comparison between mechanical property data of CC hemicellulosic polymers processed with different methods.

Table 4.2 Mechanical property data including TS, %eb, and E for materials obtained from CC hemicellulosic polymers by different polymer processing techniques.

Production Method	*TS (MPa)*	*eb (%)*	*E (MPa)*	*Reference*
3D printing	11 ± 4	7 ± 5	545 ± 100	present study
Extrusion	76 ± 6	35 ± 8	1073 ± 86	Bahcegul et al. (2013)
Solvent casting	35 ± 4	6 ± 1	1778 ± 198	Bahcegul et al. (2014)

A shown in Table 4.2, lower TS, % eb, and E values were obtained for 3D printed materials compared to both solvent cast and extruded materials which were obtained from the same type of hemicellulosic polymers.

Seven times lower UTS and 5 times lower %eb values compared to extrusion was measured for 3D printed hemicellulosic polymers. Around 2 to 3 times lower E values and 3 to 7 times lower TS values were obtained when hemicellulosic polymers were 3D printed instead of using solvent casting or extrusion methods.

These differences in the mechanical properties of the materials obtained with 3D printing and other conventional methods are expected and could be attributed to the processing principle of the FDM technique. Lower mechanical properties of 3D printed hemicellulosic biopolymers can be related to insufficient interlayer bonding in FDM which is also the case for 3D printed cellulose-based materials (Wang et al., 2018). There is also difference between the CAD model and the actual 3D printed model after drying since the paste contains a certain amount of water, which evaporates during drying. These could lead to shape deviations as the printed model starts to shrink during the drying period. This situation is also considered to contribute to the inferior mechanical properties of 3D-printed materials (Zhang et al., 2020; Wang et al., 2018). Void formation during the printing process of FDM is also reported to adversely affect the mechanical properties (Priya et al., 2019).

4.6 SEM analysis of the 3D printed models from hemicellulosic pastes

As shown in Figure 4.25, SEM images reveal mostly homogeneous cross-sections with some occasional crystal-like particles. These particles were identified to contain high amount of potassium via EDX and thus they are most likely KAc particles, which is expected in this case since the presence of KAc was also verified by the FTIR spectrum of the hemicellulosic paste (please see section 5.4). The surface of the samples was very different from the cross-section and covered with inorganic crystals, which were again KAc particles since a very high potassium content was detected here via EDX analysis performed simultaneously with SEM. It appears that the KAc salts have migrated to the surface of the samples, which should have a lower water content compared to the inner part of the samples.

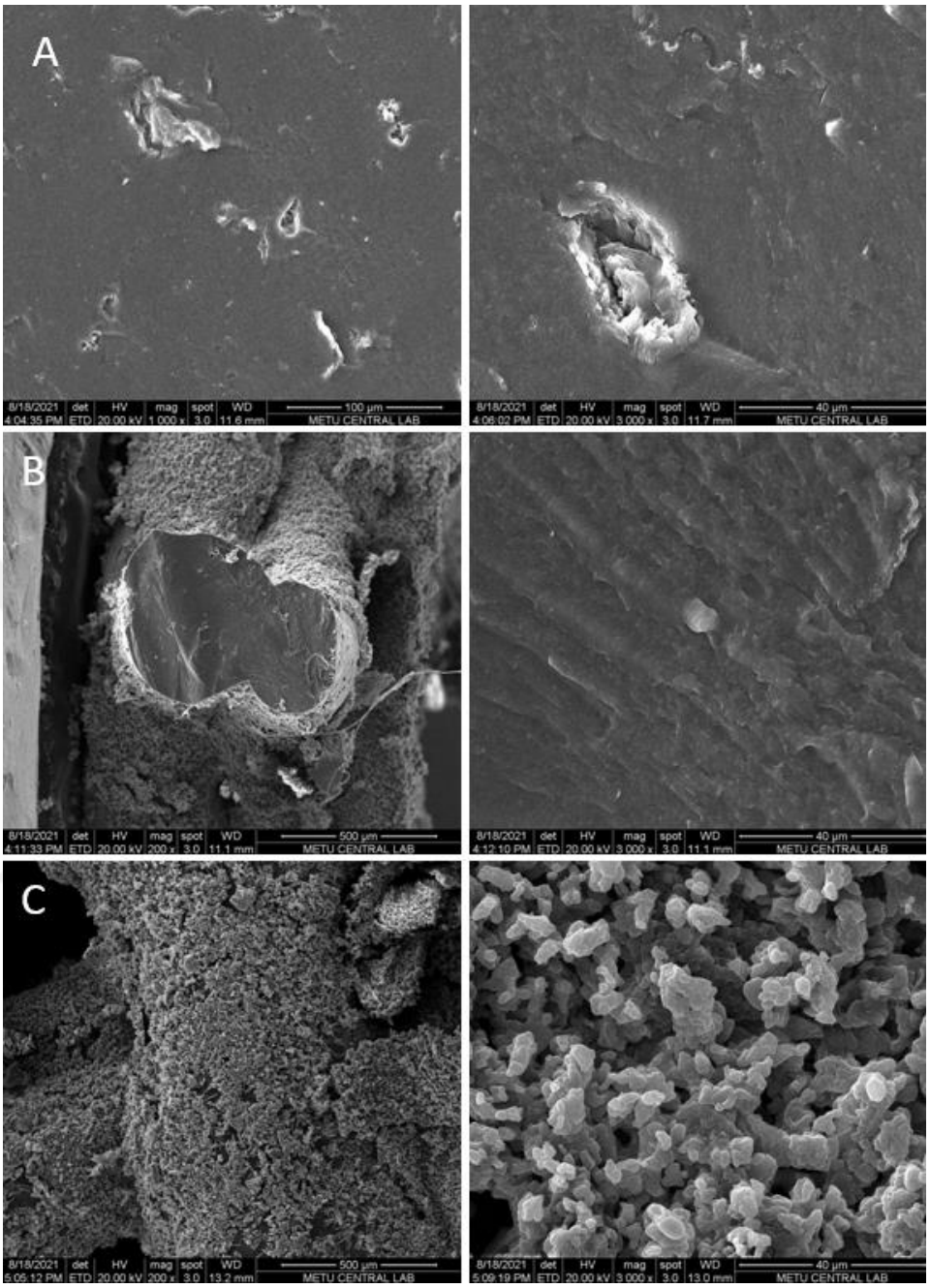


Figure 4.25 (A) Cross-section SEM images of a dog bone shaped model and (B) cross-section, (C) surface SEM images of the dried grid model printed from the hemicellulosic paste at two different magnifications.

CHAPTER 5

3D PRINTING OF CC EXTRACTS CONTAINING HEMICELLULOSE AND LIGNIN

The hemicellulosic paste based 3D printing strategy described in the previous chapter involves the precipitation of the polymers dissolved in the alkaline medium at the end of the extraction process by using a solution of ethanol and acetic acid followed by the collection precipitated polymers (hemicellulose and lignin) via filtration from the extraction medium. These precipitation and filtration stages not only bring additional steps to the overall process but some of the polymers dissolved in the alkaline medium, especially lignins, are lost as these are not totally precipitated together with hemicellulose polymers. Taking these issues into account, a novel strategy that focuses on using all the polymers dissolved in the alkaline medium directly is developed and described in this chapter. The strategy here is to use the entire alkaline medium, with all the dissolved polymers in it, in 3D printing without any precipitation and filtration steps. In order to achieve this, the alkaline solution containing dissolved hemicellulose and lignin polymers, which is called as the "CC (CC) extract" is used in 3D printing. However, the CC extract viscosity is very low at the end of the extraction process and not suitable for 3D printing. In order to solve this problem without using any cross-linkers or any additives and auxiliary polymers to increase the viscosity, the water content of the CC extract was reduced to a certain extend upon the evaporation of water, which enabled the formation of a thermoreversible cold-setting gel. This gel, which retains its shape at room temperature while becoming a flowing viscous liquid at mild temperatures, is very advantageous for 3D printing since once it is deposited on to the build platform, it can retain the intended shape of the model and flows adequately from the nozzle during the printing process. This strategy also removes the precipitation step from the process while using more of the biopolymers available in the lignocellulosic

biomass (CCs). Since such a strategy is explored and reported for the first time in the literature related to lignocellulosic biomass-based 3D printed materials, numerous preliminary trials were made in the beginning, just like the studies described in the previous chapter. Following the preliminary studies, more systematic studies and further characterization were performed, which are explained in detail in this chapter.

5.1 Preliminary studies on the general factors influencing the 3D printability of CC extracts containing hemicellulose and lignin

As the first phase of preliminary trials, different CC extraction solutions were obtained by changing the alkaline extraction parameters and these were used in manual dispensing trials by using a syringe also with the 3D printer if applicable. The main reason for changing the extraction parameters was to obtain an extract solution with a higher viscosity that was more suitable for 3D printing.

The typical extraction solution contains 10% (w/w) KOH dissolved in water. The first approach taken was to reduce the amount of water during the extraction while keeping the KOH concentration as well as the amount of CCs subjected to extraction the same. In this context the volume of the liquid extraction medium was first reduced by 20% but the viscosity of the extract obtained at the end of this extraction was still too low (quite similar to the viscosity of water) to be processed by 3D printing. In order to check if sufficient viscosity at this stage would really enable 3D printing, carboxy methyl cellulose (CMC) sodium salt was added to the solution at a concentration of 3% (v/w), which increased the viscosity as expected.

3D printing trials were made with this CMC containing extract as shown in Figure 5.1. Once the 3D printing process has started it was observed that the CMC containing extract was being spread much higher than intended, creating thicker lines, and thus giving smaller cell areas. As the printed lines were too thick an anti-solvent solution consisting of 10% acetic acid in ethanol was added simultaneously

with printing to prevent printed lines from spreading and to fix their shape once they were extruded. The model printed this way is shown in Figure 5.1. Therefore, CMC sodium salt was found to improve the printability of the CC extract. However, the studies were focused back to examining the ability to print CC extract without an auxiliary polymer added externally after the extraction to increase viscosity and thus the printability.

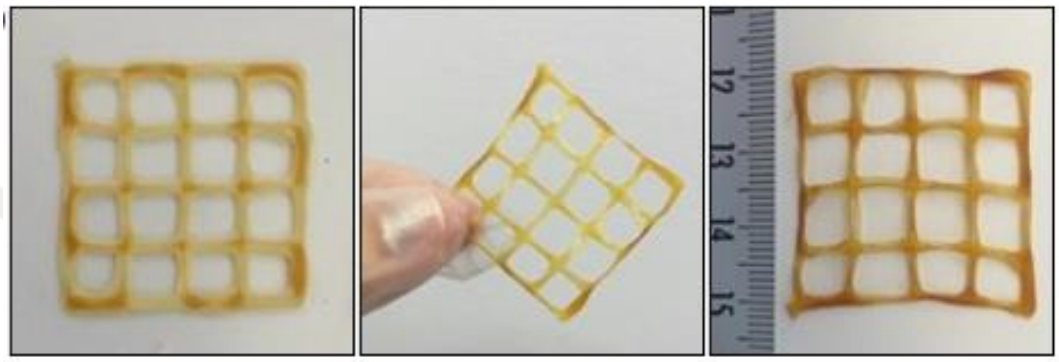


Figure 5.1 Trials to print 40 x 40 mm three- layered grid structure printed with (A) 200 mm/min, 0.68 mm layer height (B) 200 mm/min, 0.54 mm layer height.

In order to determine if sufficient viscosity obtained at the end of extraction would give 3D printable extracts without externally adding an auxiliary polymer such as CMC following the extraction, wheat bran (WB) was used instead of CC during extraction. The reason for using WB instead of CCs was that at the same extraction conditions, WB gives an extract with a much higher viscosity. As an initial trial, WB extract was loaded to a syringe and filaments were obtained from the extract at room temperature once the WB extract was deposited into the antisolvent bath composed of acetic acid and ethanol. Since this preliminary experiment was promising, 3D printer was used at room temperature to print the grid model from the WB extract. As shown in Figure 5.2, grid models could be printed this way to a certain extent with some defects and the appearance of the models differed significantly depending on how the antisolvent was added. When the antisolvent was added after the printing process, the extract spread too much and there was excessive bubble formation in the model. On the other hand, the spreading as well as the bubble formation could be

prevented when the antisolvent was added simultaneously during printing. However, a model consisting of fibers rather than an intact model was obtained this time as shown in Figure 5.2B. Adding the antisolvent simultaneously during printing prevents the layer adhesion from taking place since the surface is covered with the antisolvent. Since the extract solidifies almost immediately following its deposition from the nozzle, the nozzle drags the printed material as it moves, leading to the formation of irregular cells with round edges rather than the intended square shaped cells.

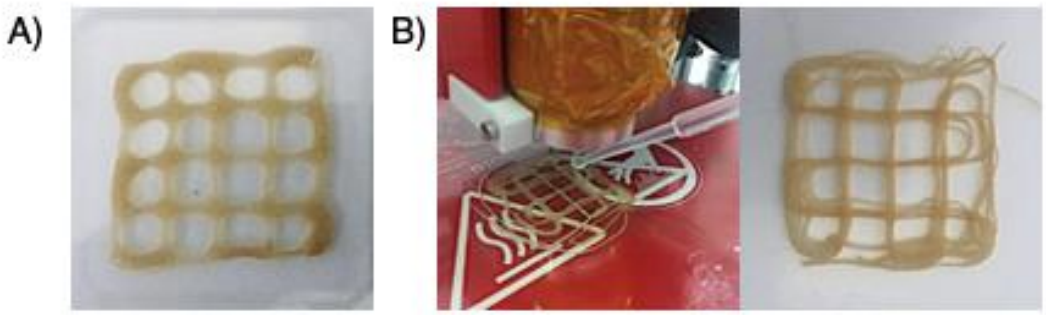


Figure 5.2 3D models printed from wheat bran extracts by the addition of the solvent after printing (A) and simultaneously during printing (B).

Once the viscosity increase obtained by using WB instead of CC was observed, this time CC and WB were used together in order to take advantage of the viscosity increase brought by WB while still using a lignocellulosic biomass blend rich in CC. For this purpose, WB and CC biomass particles were mixed at a ratio of 1:3 (w/w) and subjected to alkaline extraction under typical conditions. The extract obtained did have an increased viscosity, but the results obtained this way were very similar to those shown in Figure 5.2 where spreading of the extract and extensive bubbles inside the model were again observed.

Based on these preliminary results, it was observed that increasing the viscosity of the CC extract alone was essential to render it 3D printable and studies were focused again on the CC extract alone. It was not possible to reduce the volume of the alkaline medium used during extraction below a certain threshold since when the volume was

lower than it should be the solid CC particles could not be mixed properly during extraction. In other words, when the solid (CC particles) to liquid (alkaline solution) ratio was too high, effective mixing of CC particles inside the alkaline solution could not be achieved since the amount of liquid inside the extraction system was insufficient compared to the solid CC particles. Eventually this prevented the extraction to be performed in an appropriate way. Therefore, instead of reducing the volume of the alkaline solution used during extraction, the water content of the extract, which was obtained following the completion of the extraction procedure, was reduced simply by evaporation. This was done in order to obtain CC extracts with higher viscosities.

As a preliminary trial in this context, the CC extract was subjected to a heat treatment for 1 h at 70°C to evaporate some of its water content by reducing the volume of the extract by 30%. Once the stirring was stopped and the extract was cooled to room temperature, a crust was observed at the top of the together with some lumps inside the extract and there was a significant increase in the viscosity. The extract was stirred again following the addition of water to homogenize it.

The extract obtained this way was used for the 3D printing trials at room temperature and as shown in Figure 5.3, grid models could be printed to a certain extent. The problem with these models was that following the addition of the antisolvent, they could not be removed from the built platform. Removing the printed models from the platform was tried both when the models were still wet and when they were dried. In the case of dried models, the models had to be scratched (rather than being detached) from the platform, they simply did not have an intact structure. When the models were wet, they could be removed from the platform but in pieces rather than as a whole since again the material seemed too weak to keep itself intact. An important observation made here was that the printed model, even though it had 6 layers, looked like a 2D structure rather than a 3D one since it lacked any significant height. The most likely reason for this could be insufficient dry matter (polymer) concentration in the extract so increased amount of material was extruded from the

nozzle by increasing the EM setting of the printer. However, the results were still similar as shown in Figure 5.3.

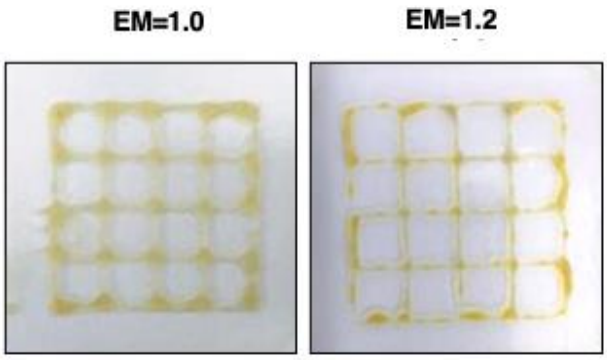


Figure 5.3 Appearance of grid models from partially concentrated CC extracts printed at room temperature at different EM values.

Another important observation related to this trial was that the printed models had a lighter color when the antisolvent was added on to the models and the lines of the models seemed to get thinner as if the material that makes up the model was being washed away with the antisolvent. A likely reason for this could be the excessive salt formation because of the acid-base reaction that takes place between the KOH in the CC extract and the acetic acid in the antisolvent.

As shown in Figure 5.4, the same model was also 3D printed by using a nozzle with a higher inner diameter (1.23 mm) with the idea that this might increase the amount of polymer found in model. Considering the salt formation because of the acid-base reaction mentioned above, in addition to the acetic acid ethanol solution, a washing solution containing only ethanol and no acetic acid was also used to wash the printed model to understand whether the printed lines would become thinner and deformed again. It was observed that when the antisolvent containing acetic acid and ethanol was used, the continuity of the lines forming the model was decreased since the lines became significantly thinner compared to when they were washed with ethanol only (Figure 5.4B and C). The printed model also lost its thickness considerably and could not be removed from the glass surface when dried when the acetic acid containing antisolvent was used. On the other hand, when only ethanol was used to wash the

models, the model retained its integrity and could be removed from the glass surface without letting it dry as shown in Figure 5.4C.

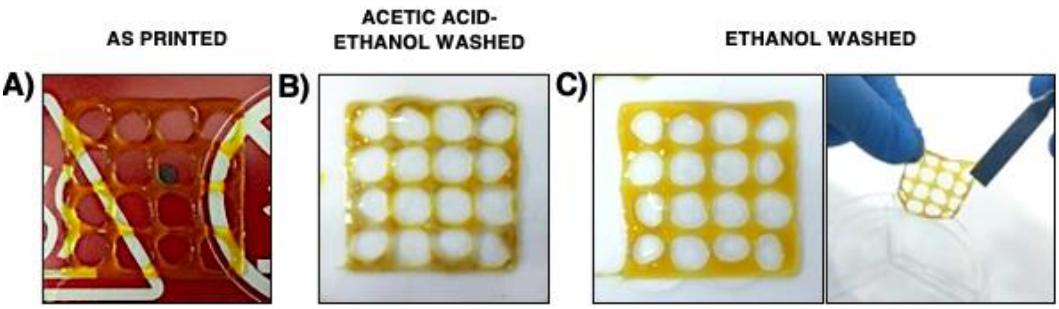


Figure 5.4 Appearance of 40 x 40 mm three-layered grid structure printed with nozzle tip with 1.23 mm inner diameter (A) as printed (B) after washing with acetic acid-ethanol solution (C) after washing only with ethanol.

Based on the observations related to the antisolvent, a new extraction was performed by using a 5% KOH solution instead of the typical 10% KOH solution with the thought that the acid-base reaction in this case could be less detrimental for the integrity of the models. The partially concentrated CC extract was 3D printed again in a similar way as described above and antisolvents with different acetic acid concentrations were used this time to understand the effect of antisolvent composition on the printed models.

As shown in Figure 5.5, the amount of acetic acid found together with ethanol in the antisolvent has a dramatic impact on the printed model. The first trial was made with a solution of acetic acid and ethanol with a typical acetic acid concentration of 10% since this was the original content of acetic acid in the solution during the hemicellulose precipitation step in the alkaline extraction process. However, it is obvious that this solution is detrimental for the printed models as shown in Figure 5.5A, indicating that 10% acetic acid in ethanol leads to different results when used as a precipitating solution for the hemicelluloses at the end of alkaline extraction and when it is used as an antisolvent for the printed models obtained from the CC extract. Reducing the acetic acid content to 5% and further down to 2.5% gave better results

in terms of the integrity of the models after washing but it appears that the presence of acetic acid in the antisolvent is not necessary since when only ethanol was used with no acetic acid at all, models with sufficient hardness and integrity could still be obtained as shown in Figure 5.5D.

In fact, once the ethanol was in contact with the model, the lines in the model became apparently harder and this could be observed when the model was examined with a spatula. This hardness that took place once the model was in contact with the ethanol is probably because of two factors that took place simultaneously. First of all, the printed model contains significant amount of water, which acts as a plasticizer, making the material softer. When relatively a large volume of ethanol is in contact with the model, the water in the printed model dissolves in ethanol canceling the plasticization effect. Ethanol is also an antisolvent of hemicellulose. Therefore, it is reasonable to assume that these two factors are responsible for the immediate hardening of the printed models once the ethanol is in contact with them.

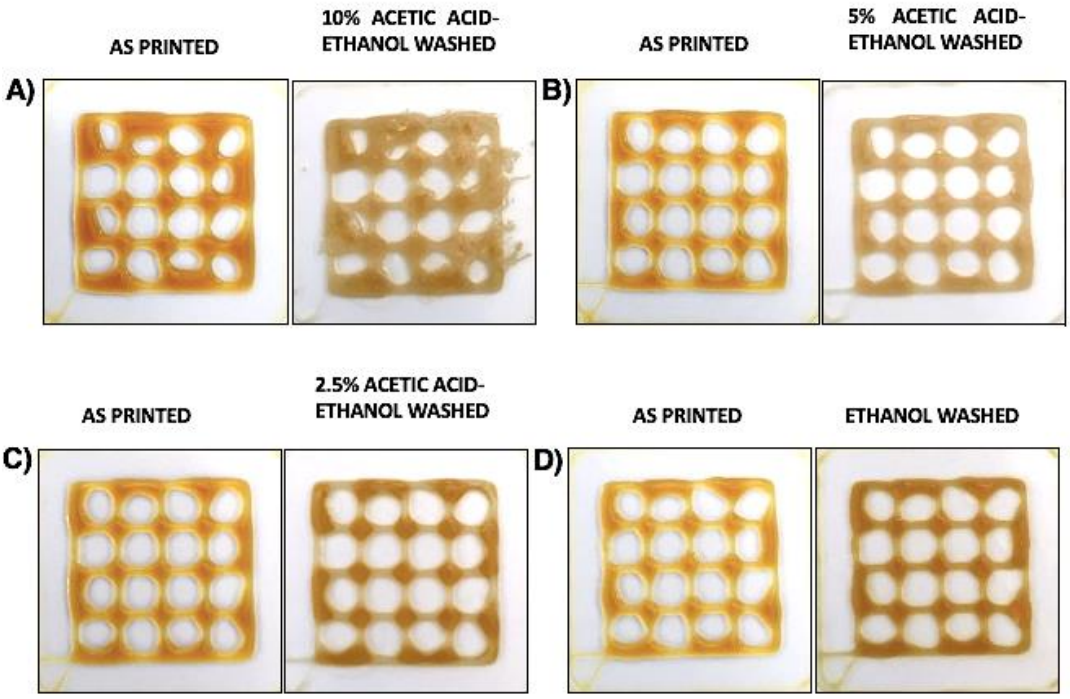


Figure 5.5 Six layered grid models printed from partially concentrated CC extracts washed by different antisolvents.

Instead of washing the models with antisolvent while they were on the glass build platform, which made it harder (or sometimes impossible) to detach them from the platform once they were dry, models were printed on to stretch plastic films (like previously done for the hemicellulosic pastes) so that they could be totally immersed in an antisolvent bath. For this purpose, the stretch film with the printed model on it was removed from the build platform by cutting it with a knife around the sides and it was completely immersed into the antisolvent bath. It was observed that when this procedure was followed, the printed model easily detached itself from the stretch film on its own without needing any outside intervention.

Antisolvent baths having different acetic acid concentrations were prepared and as shown in Figure 5.6 consistent results were obtained with the case in which the antisolvent were added onto the model when they were on the build platform. Immersing the models into the washing bath appears to work fine when the antisolvent formulation is correct. Printed samples preserving their integrity could easily be detached from the stretch film when they were immersed in ethanol and 5% acetic acid-ethanol baths. As expected from the previous experiments, antisolvent containing 10% acetic acid was detrimental for the printed models (Figure 5.6C).

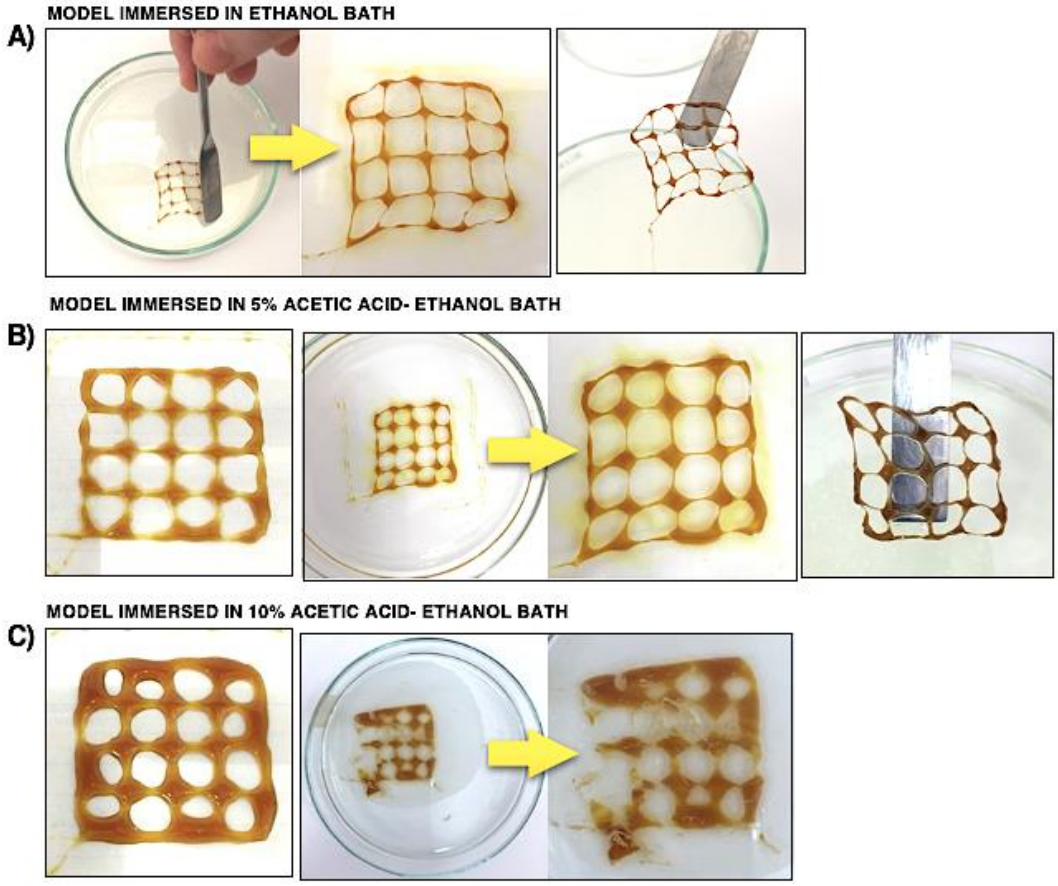


Figure 5.6 Effect of different antisolvent formulations the appearance of grid models printed from CC extract. Models were immersed in antisolvent baths prepared with (A) ethanol (B) 5% acetic acid - ethanol solution (C) 10% acetic acid-ethanol solution.

One of the most critical observations in the preliminary experiments were made when the water content of the CC extract was further reduced. The water content of CC extract obtained from alkaline extraction process performed with 5% KOH at 80°C for 3 hours was further reduced by 60% instead of the 43% reduction in the previous trials. Following the evaporation, the concentrated extract was left to cool at room temperature inside a beaker. Approximately an hour later, it was observed that a gel was obtained inside the beaker. The formation of the gel was unexpected since it was thought that a more viscous extract was going to be obtained but the

formation of the gel is very advantageous for 3D printing as will be discussed in the upcoming sections of this chapter.

By making 3D printing trials at mild temperatures higher than room temperature, it was found that this gel was thermoreversible meaning that while mild temperatures enabled it flow adequately from the nozzle for 3D printing, the gel could retain the intended shape once it was deposited on to the build platform. In other words, this was a cold setting thermoreversible gel, which was very advantageous for 3D printing. All the studies after this point were performed by using the so-called gel extracts.

As shown in Figure 5.7, this gel extract could be successfully printed at a temperature of 50°C and extruded lines could retain the intended shape during the printing process for the first time. Printed model with the gel extract was found to be much more similar to the original model compared to the results obtained with all the other trials including the ones made by the partially concentrated CC extract. The model could easily be removed from the glass surface as shown in Figure 5.7 since it had the sufficient strength retain its integrity when antisolvent (ethanol) was added.

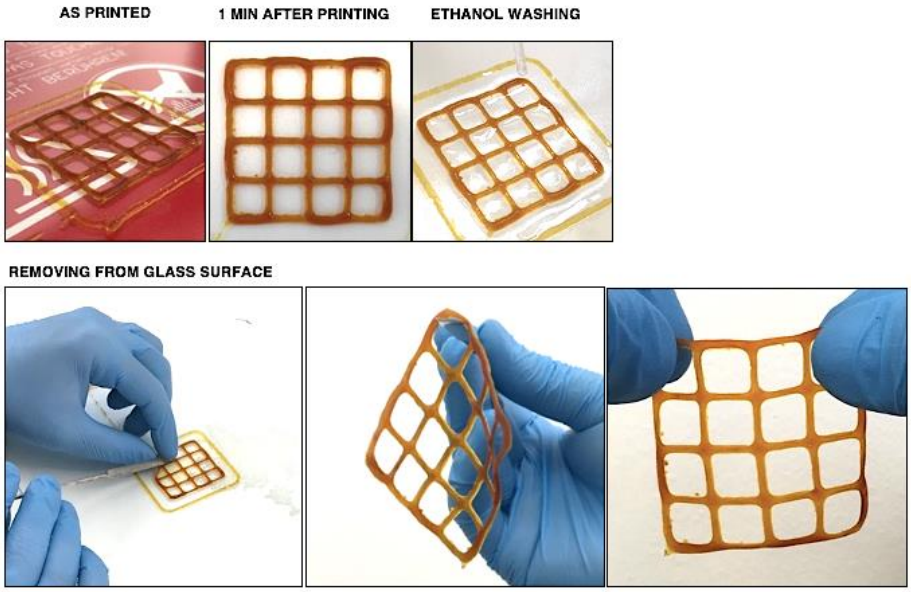


Figure 5.7 Appearance of the 4 x 4 cm grid model printed from the gel extract at 50°C following the addition of ethanol as the antisolvent.

It is important to note at this point that when printed from the extracts with lower water contents (and thus higher viscosity), the printed models had the sufficient mechanical strength to be removed from the glass build platform most likely because compared to the less concentrated extracts (where 43% of the water in the extracts were evaporated) these extra concentrated extracts (where 60% of the water in the extracts were evaporated) had higher polymer concentrations. Since building the models onto the glass build platform instead of the stretch film is more practical, stretch film approach was not initially followed at this stage of the experiments.

5.2 Effect of 3D printing parameters and water content on 3D printability of CC extracts

Based on the initial findings obtained from the preliminary trials, the extract obtained at the end of the alkaline extraction process was concentrated upon the evaporation of around 60% of its water content which led to the formation of a gel upon cooling to room temperature. The impact of process parameters and water content on 3D printability of CC extracts were further investigated to determine the optimum printing conditions. For this purpose, CC extracts with two different water contents which were 76.82% and 79.18% were printed by using two different nozzle tips (with inner diameters 0.54 mm and 0.68 mm) in a temperature range of 45-65°C (Figure 5.8).

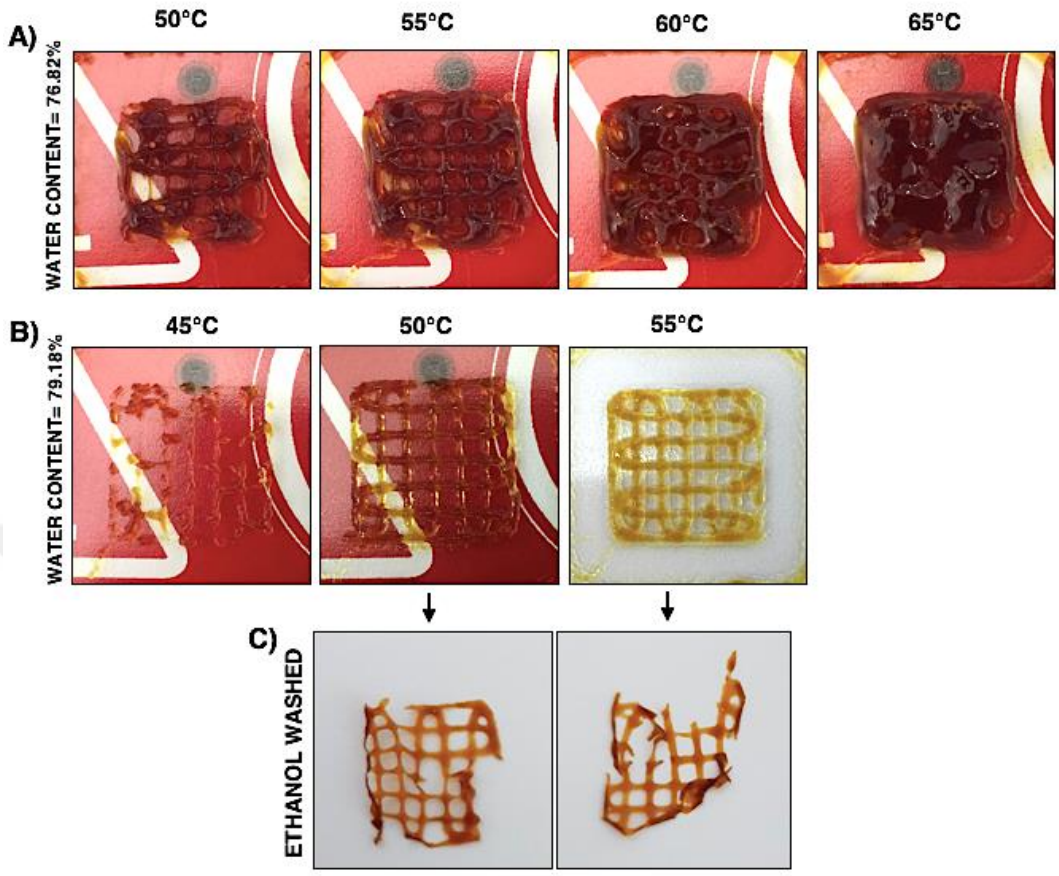


Figure 5.8 Four-layered 2 x 2 cm models printed with CC gel extract with (A) 76.82% water content in the temperature range of 50-65°C and 0.68 mm nozzle tip (B) 79.18 % water content in the temperature range of 45-55°C and 0.54 mm nozzle tip. (C) Appearance of the models printed at 50 and 55°C after being removed from the build platform following ethanol washing.

The results displayed in Figure 5.8 shows the importance of nozzle diameter related to the resolution as well the amount of material deposited. Decreasing the nozzle diameter from 0.68 to 0.54 gave better results in terms of the appearance of the printed models as shown in Figures 5.8A and 5.8B. However, in addition to the obtained resolution, sufficient material deposition is also an important issue since insufficient material deposition may impair the intactness of the printed models upon washing with ethanol as shown in Figure 5.8C.

Water content of CC extract obtained from the alkaline extraction process performed with 5% KOH at 80°C for 3 hours was further reduced to obtain gels with 66.28% and 50% water contents and these gels were used in 3D printing trials to further understand the influence of the gel extracts' water content on 3D printability. A four-layered 20 x 20 mm grid model was tried to be printed with two different nozzle diameters (0.68 and 0.84 mm) at several different temperatures between 55-100°C with EM values range of 1.2, 1.5 and 2.0.

Despite these large set of printing parameters employed to conduct the 3D printing trials, neither of these extracts with lower contents could be printed since a successful printing of the grid shaped model could not be obtained. The material flow was insufficient at the lower end of the temperature range and increasing the nozzle diameter or the EM did not help with this issue. The viscosity of the CC extract was too high for the step motor to push it out of the nozzle as well, which was observed at the lower end of the temperature range or when the extract with the lower water content of 50% was used. The temperature was further increased to 100°C together with an EM value of 2 while using the nozzle with the larger diameter of 0.84 mm to solve the problem with the insufficient polymer deposition out of the nozzle. However, the material extruded out of the nozzle had a very different texture this time and it was very sticky, which was really problematic during 3D printing since the material accumulated around the nozzle continuously once it was deposited on to the build platform, making it impossible to obtain to a model with a proper shape. Based on these experiments, it was concluded that the CC extract coming out of the nozzle should be less viscous and reducing the extracts water content up to this level did not work well.

Based on all the results obtained so far regarding a large variety of parameters related to the extraction conditions, the formulation of the extract and the printing process itself, a comprehensive experiment was designed to cover three different water contents of the extract and five different printing temperatures to determine the

optimum conditions in which the 3D printing of the CC extracts should be performed.

As shown in Figure 5.9, the CC extracts are extremely sensitive to water content and changes in the printing temperature as small as 5°C can have a dramatic impact on their 3D printability of the extracts indicating a very narrow window in which the extracts can be printed successfully. As shown in Figure 5.9A, extracts with a water content of 76% could not be printed in the temperature range utilized for the experiments. This is quite striking since it shows that even at a very high water content of 76%, the extracts might not be suitable for 3D printing due to inadequate flow of the material. Increasing the water content of the extract by just an additional 5% gave totally different results as shown in Figure 5.9B for all the temperatures tested. The best results were obtained for the 3D printing temperatures of 45°C and 50°C. Increasing the temperature to more than 50°C decreased the viscosity of the extract too much, which yielded a model where the cells were mostly closed. When the water content of the extract was further increased to 86% again a totally different behavior of the extract was observed for all the printing temperatures. As shown in Figure 5.9C, the low viscosity of the extract made it impossible to print the desired model since no definite shape could be obtained at this water content.

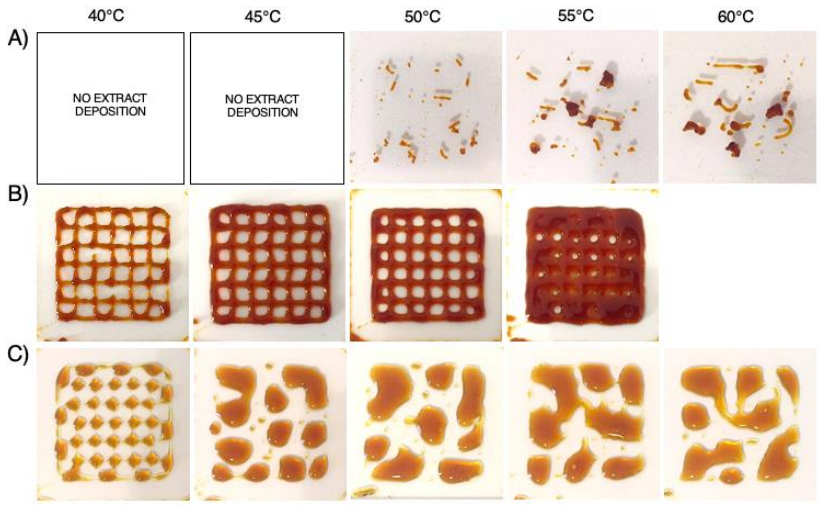


Figure 5.9 Four-layered 32 x 32 models printed from CC extract with (A) 76% (B) 83% and (C) 86 % water contents at different temperatures.

5.3 Effect of performing the alkaline extraction with lower KOH concentration on the 3D printability of CC extracts

CC extraction was also performed with a lower KOH concentration to see if decreasing the KOH content of the CC extract might be possible. The extraction of hemicellulose and lignin polymers from CC was performed with 3% KOH solution at 80°C for three hours instead of using a 5% KOH solution. Before the printing process, the extract was concentrated again by partially evaporating its water content just like it was done with the extract obtained by using 5% KOH solution. After the evaporation step it was observed that the viscosity of the solution extracted with 3% KOH was much lower than that of the solution extracted with 5% KOH even though the same amount of water was evaporated from both extracts. No gel formation was observed for the extract obtained with 3% KOH unlike the case with 5% KOH. This is most likely because the extract obtained with 3% KOH contains less amount of dissolved polymers compared to the extract obtained with 5% KOH solution. Reducing the water content of the 3% KOH extract further also did not lead to any remarkable increase in viscosity or gel formation when compared with the 5% KOH extract. Therefore, due to the low viscosity of this extract, 3D printing was performed at room temperature and higher temperatures utilized for the gel extract were not studied. Water content of the extract was measured as 67.17%. Although this water content was lower than that of extracts obtained with 5% KOH solution, it was observed that the extract was easily flowing at room temperature unlike all the CC extracts at three different water contents, which had a gel like solid structure at room temperature without any flow.

In the case of extracts obtained with a 3% KOH solution from CC, the extracts could come out of nozzle at room temperature when the EM was increased from 1.2 to 1.5. However, as shown in Figure 5.10 the model could not be 3D printed properly since the extract could not be deposited to evenly to all parts of the model. The model was also too weak most likely because of the extract's low polymer concentration, which

eventually led to the deposition of insufficient polymeric material and did not detach from the stretch film easily in the ethanol bath.

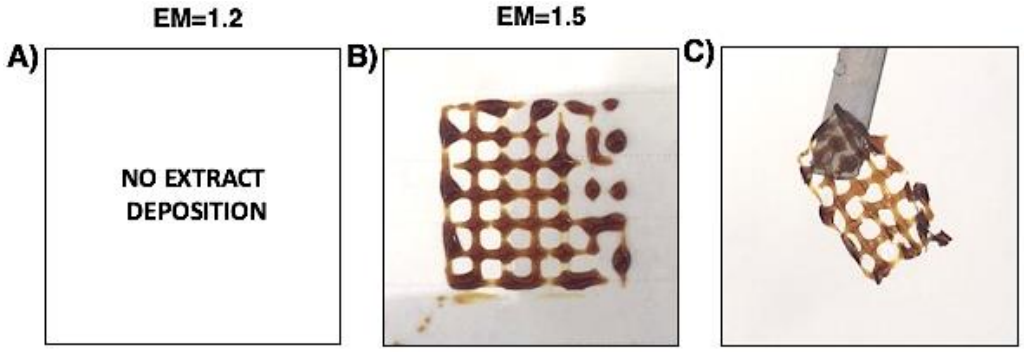


Figure 5.10 A four-layered 20 x 20 mm model printed from the CC extract obtained following the extraction with 3% KOH solution printed with an EM of 1.2 (A) and 1.5 (B) The appearance of the model after immersion into the ethanol bath is given in (C).

The key aspect of the procedure developed for the printing of the alkaline extracts obtained from CCs is obviously the gelation of the extracts, which could be obtained after around 60% of their water content was evaporated following the alkaline extraction which was performed with 5% KOH solution at 80°C for 3 hours. This gelation is essential for the developed 3D printing process because it makes the process resemble the conventional 3D printing processes, at least to a certain extent, which relies on the flowing of polymers at elevated temperatures followed by their solidification once they are deposited onto the build platform. Thanks to this gelation, CC extracts behave in a similar manner to conventional polymers such as PLA during 3D printing since the extracts flow at around 50°C and they solidify in the form of a gel at room temperature (as they exit from the nozzle and deposited on to the build platform), which enables them to retain their intended shape to a certain extend and preventing the excessive spread of printed lines due to insufficient viscosity. Figure 5.11 shows some images of the CC extracts in the form of a gel.

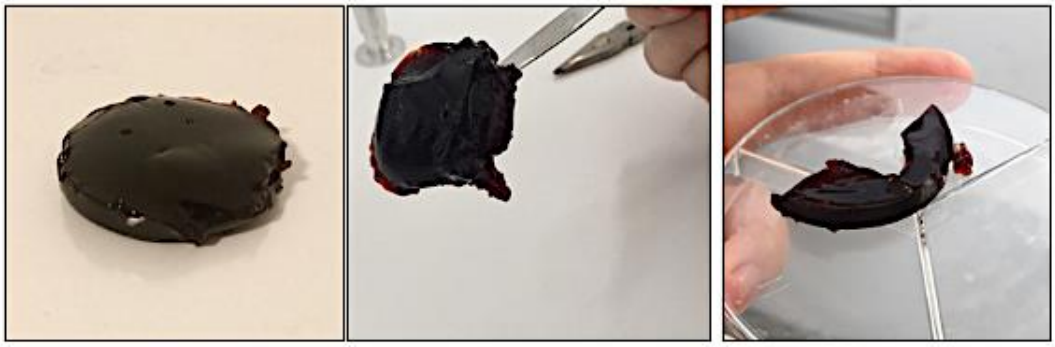


Figure 5.11 Appearance of the gel obtained from the alkaline extracts of CC.

The gelation observed with the CC extracts might be due to different gelation mechanisms, which are related to the presence of arabinoxylans in the CC extract. One of these gelation mechanisms is related to ferulic acid, which is a phenolic compound, in which the cross-linking of arabinoxylan chains with ferulic acid takes place (Anderson and Simsek, 2018; Kiszonas et al., 2013; Morales-Burgos et al., 2017; Nino-Medina et al., 2010; Marcia, 2009). Arabinoxylan, composed of a xylose backbone substituted with arabinose groups, is an abundant form of hemicellulose in CC and it can be co-extracted with ferulic acid from CC by alkaline extraction (Torre et al., 2008). The covalent cross-linking of arabinoxylan chains by ferulic acid thus leads to the formation of a gel. However, this might not be the relevant gelation mechanism in our case due to two reasons. First, for such a gelation to take place, oxidation via enzymatic or chemical compound such as peroxidase, laccase, ferric chloride or ammonium persulfate are necessary (Morales-Burgos et al., 2017; Niño-Medina et al., 2009) and these were absent in our case. The second reason is that such gels formed by the covalent cross-linking of arabinoxylan chains by ferulic acid are thermoirreversible but in our case the gel we have obtained was thermoreversible. When heated from room temperature to moderate temperatures, the CC extract gel became a highly viscous liquid and when cooled back to room temperature it again formed a gel. In fact, as explained earlier, this was one of the key mechanisms that made the CC extract 3D printable.

Other than the ferulic acid based cross-linking mechanism discussed above, another reason for the gelation of the CC extracts might be related to the junction zones

formed by arabinoxylans due to intermolecular hydrogen bonding (Fincher and Stone, 1986; Sørensen et al., 2007; Sinha et al., 2011). In fact, various intermolecular interactions play a critical role for the gelation of polysaccharide solutions in which such polysaccharide gels can be thermoreversible and cold-setting gels, meaning that the gelation is observed when the solution is cooled below a certain temperature (Cui, 2005), which is exactly what happens in our case with the CC extract. Even though the junction zones are essential for the formation of gels (Saha and Bhattacharya, 2010), if the zone of interaction in these junctions is too long then molecular aggregations that can prevent gel formation might take place (Spyropoulos et al., 2019). Therefore, to facilitate gel formation, a structure breaker that enables the formation of multiple junction zones with limited lengths at different places thorough out the gel structure is necessary, which might be the arabinose group found as a side chain in CC arabinoxylan for our case (Spyropoulos et al., 2019).

5.4 Chemical and thermogravimetric properties related to CC extracts in comparison with the hemicellulosic pastes

Following the alkaline extraction performed with CC, different fractions were obtained, some of which were used as 3D printing materials following additional steps such as NaOH addition (for hemicellulosic pastes) or evaporation (for extracts containing hemicellulose and lignin). The IR spectrum of these samples were obtained with an ATR-FTIR, and comparisons were made between these fractions to understand the chemical differences between them especially with respect to the changes relevant to hemicellulose and lignin. For lignocellulosic biomass, the wavelengths between 800-1800 cm^{-1} are considered as the "fingerprint region" by Zhou et al. (2011) since this region contains most of the bands assigned to cellulose, hemicellulose and especially lignin. Therefore, after the spectrum between 400–4000 cm^{-1} was obtained and the fingerprint region between 800 – 1800 cm^{-1} was used to compare different samples with each other.

The FTIR spectrum between 800–1800 cm^{-1} for CC before and after alkaline extraction is given in Figure 5.12. The band at 1728 cm^{-1}, which is present for native CC, completely disappears after the alkaline extraction process, which is related to the removal of hemicelluloses since this band is assigned to C=O stretching of hemicellulose (Xu et al., 2013; Sim et al., 2012). A similar disappearance of the band at 1515 cm^{-1} following the alkaline extraction indicates lignin removal from CCs since this band is related to the aromatic rings in lignin (Popescu et al., 2007; Sammons et al., 2013; Rashid et al., 2016). Another major difference between the two spectra take place between 1200 cm^{-1} and 1300 cm^{-1} since the intensity of the valley between these wavenumbers is decreased following alkaline extraction. According to the literature, this range contains bands associated with the aromatic groups in lignin at various wavenumbers including 1222 cm^{-1} for aromatic ring breathing with C-O and C=O stretching (Sun et al., 2005). 1234 cm^{-1} for syringyl ring and C=O stretch (Zhou et al., 2011) and 1265 cm^{-1} for C-O stretch of guaiacyl ring. Therefore, this decrease in the intensity of the valley located here can be regarded as an indication for the removal of lignin from CC while also showing some lignin was still retained in the CC after the extraction. The retention of lignin in CC following alkaline extraction is also evident from the strong band at 1160 cm^{-1} present in both spectra, which is assigned to the syringyl-guaiacyl-hydroxyphenyl units of lignin (Sharma et al., 2017). Similar to lignin, some hemicellulose also remains in CCs after the extraction, which can be deduced from the presence of the bands at 895 cm^{-1} assigned to ß-glycosidic linkages (1->4) between xylose units in hemicelluloses for both spectra (Sun et al., 2005).

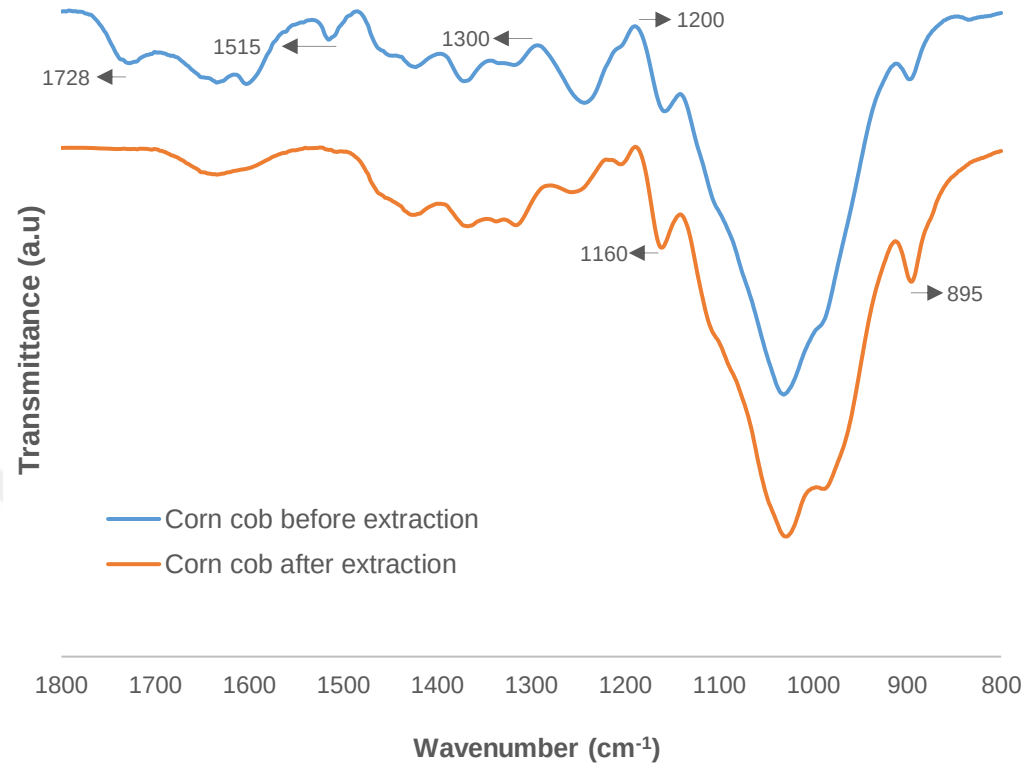


Figure 5.12 IR spectrum of CCs before and after alkaline extraction.

As shown in Figure 5.13, hemicellulosic paste and the gel extract has very different infrared spectra at the fingerprint region between 800 cm^{-1} to 1800 cm^{-1}. This was an expected result since the way these two materials are obtained from CCs was different. The hemicellulosic paste is precipitated at the end of the alkaline extraction by the addition of ethanol and acetic acid. On the other hand, no such precipitation step takes place for the gel extract since instead of precipitation, the alkaline extract is evaporated to reduce its water content to around 80% so that gelation can take place once the extract is cooled to room temperature. The precipitation step not only causes some of the lignin to be removed but it also causes the formation of KAc because of the reaction between KOH (used during the alkaline extraction) and acetic acid. As a matter of fact, the IR spectrum shows that KAc salt is indeed retained together with the hemicellulosic paste. As shown in Figure 5.14, the IR spectrum of KAc has two very strong bands at around 1400 cm^{-1} and 1570 cm^{-1}, which are also

present in the IR spectrum of hemicellulosic paste (Figure 5.13). The band at 923 cm $^{-1}$, which is absent in both the reference xylan and the gel extract is also related to the presence of KAc in the hemicellulosic paste since this band also appears in the IR spectrum of KAc as shown in Figure 5.14.

All three samples have the characteristic hemicellulose band at around 1040 cm^{-1}, which is related to the C-O and C-C stretching and the glycosidic linkages (Sun et al., 2005). The other band related to hemicellulose in the samples is the band at 896 cm^{-1}, which is related to ß-glycosidic linkages (1->4) between xylose units in hemicelluloses (Sun et al., 2005). This band appears as a valley for the reference xylan sample and more like a shoulder for the hemicellulosic paste. For the gel extract, the intensity of this band is increased significantly together with a shift of this band to 881 cm^{-1}. One of the major differences between the three spectra is the broad valley found in the gel extract between 1176 cm^{-1} – 1508 cm^{-1}, with two tips appearing at 1442 cm^{-1} and 1360 cm^{-1}. This wavenumber range contains various bands associated with the aromatic ring and phenolic groups related to lignin such as C–O stretching of phenol at 1236 cm^{-1}, O–H vibration of phenolic group at 1317 cm^{-1} and 1372 cm^{-1} and C-H vibration for aromatic ring at 1429 cm^{-1} and 1506 cm^{-1} (Moghaddam et al., 2017) and presence of various vibration modes makes this wavenumber range complex especially at wavenumbers below 1400 cm^{-1} (Boeriu et al., 2004). It is also worth noting that the alkaline extraction of hemicellulose and lignin from CCs also leads to the release of phenolic compounds, especially ferulic acid and p-coumaric acid (Torre et al., 2008), which likely increase the intensity as well as the complexity of the valley between the indicated wavenumber range since bands related to phenolic groups are found here (Moghaddam et al., 2017). These observations indicate the presence of higher amounts of lignin and phenolic compounds for the gel extract compared to the reference xylan and the hemicellulosic paste.

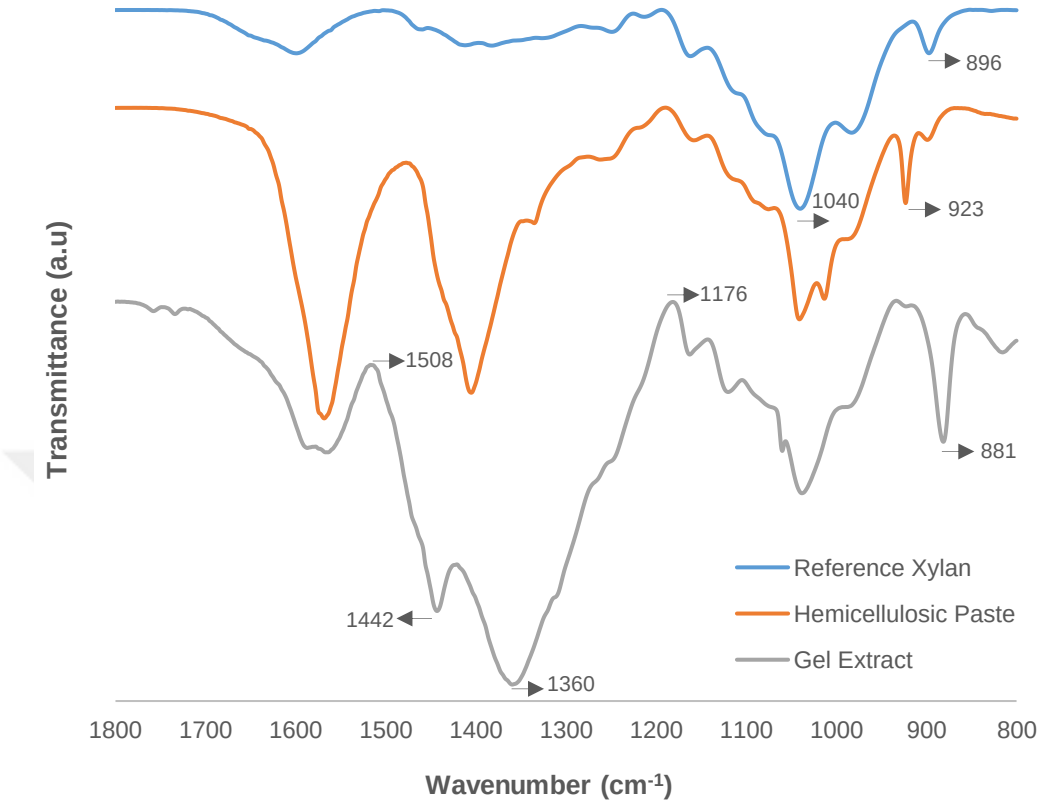


Figure 5.13 IR spectrum of reference xylan from birchwood, hemicellulosic paste and gel extract.

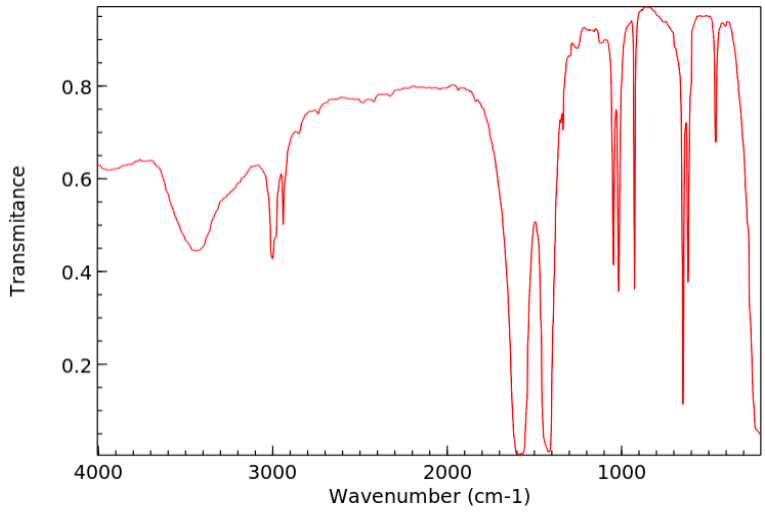


Figure 5.14 IR spectrum of KAc (from NIST webbook https://webbook.nist.gov/).

TGA of samples were conducted under nitrogen atmosphere with a heating rate of 10°C/min. CCs (before and after extraction), gel extracts and the hemicellulosic paste were analyzed with TGA to determine their weight loss profiles and thermal degradation characteristics. Prior to the analysis of the CCs, extracts and the paste, individual polymers that are found in the composition of these samples, namely cellulose, hemicellulose and lignin, were separately analyzed with TGA to provide reference values in terms of degradation temperatures and profiles.

As shown in Figure 5.15, the three polymers that make up the lignocellulosic structure (cellulose, hemicellulose, and lignin) have quite different thermal degradation profiles. MCC was used as the cellulose reference for TGA measurements. The slight weight loss of this sample up to 100°C is due to the water present in this sample, which was around 4%. The onset temperature for the degradation of pure cellulose is 342°C and cellulose loses around 90% of its original weight at 400°C showing that the degradation of cellulose takes place in a relatively narrow temperature range with maximum weight loss rate (%/min) taking place at 368°C according to the 1st derivative of the weight loss curve.

TGA measurements for hemicellulose, the major component found both in the gel extracts as well as the hemicellulosic paste, were made by using xylan from birchwood as the reference compound. The degradation onset temperature for hemicellulose is 252°C, much earlier compared to cellulose and the maximum weight loss rate occurs at 298°C, which is 70°C less than that of cellulose. Unlike cellulose, considerable weight loss continues to take place with hemicellulose samples after 400°C. Hemicellulose also retains more water compared to cellulose since at 100°C, approximately 11% of hemicelluloses weight was lost.

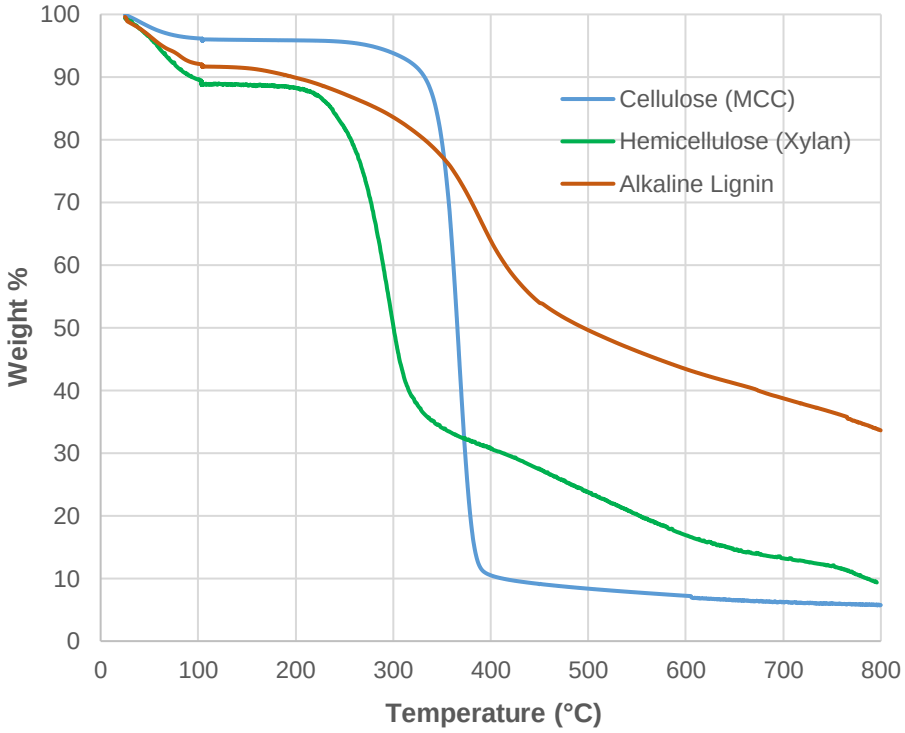


Figure 5.15 Weight loss curves for cellulose, hemicellulose and lignin obtained by TGA.

As shown in Figure 5.15, the weight loss profile for lignin is significantly different compared to cellulose and hemicellulose where alkaline lignin was used as the model compound during TGA measurements for lignin. Unlike the carbohydrate polymers cellulose and hemicellulose, lignin is a phenolic polymer with a complex structure composed of different subunits, which makes its degradation take place in a broad temperature range, which might be divided into three sections (Hua et al., 2016). The first region up 120°C includes the volatilization of impurities in addition to loss of water content in alkaline lignin (Xiao et al., 2001) followed by the second region between 120°C to 280°C where lignin degradation due to depolymerization takes place (Hua et al., 2016). The final region of weight loss profile related to lignin pyrolysis takes place up to around 550°C. This wide temperature range associated with the weight loss profile of lignin is due to presence of many aromatic rings and functional groups such as guaiacyl and syringyl units in lignin (Gu et al., 2013).

Another difference between lignin and the two other carbohydrate polymers is the amount of char remaining at 800°C. At 800°C, 34% of the lignin sample's original weight was retained, which is around 3 times higher for the material remaining in cellulose and hemicellulose samples at this temperature. This is due to the condensation or relocation of lignin in addition to the presence of inorganic minerals together with ash (Hua et al., 2016; Wang et al., 2009).

TGA of CCs before and after alkaline extraction are shown in Figure 5.16. The weight loss curve for CC before alkaline extraction actually shows the TGA of original (native) CC without any treatments applied. After the alkaline extraction to obtain hemicellulose and lignin polymers from CC, the remaining CC particles in the alkaline medium were filtered and successively washed with water in order to remove any remaining KOH in them. The weight loss curves in Figure 5.16 show that the onset temperature shifts from 256°C to 292°C for CCs following the extraction process. In other words, the temperature in which the degradation starts increases by around 36°C for CCs subjected to alkaline extraction compared to original CCs. As seen in Figure 5.15, degradation onset temperature of cellulose is much higher compared to that of hemicellulose. During alkaline extraction, hemicellulose and lignin is removed from CCs and the remaining CCs become enriched in cellulose content, which eventually shift the onset temperature to higher temperatures. The 1st derivative of the weight loss curve (%/min) also gives important clues related to the removal of hemicellulose from CCs during alkaline extraction. The 1st derivative of the weight loss curve has a peak with a doublet (two tips) at 293°C and 338°C for original CC where the doublet is most likely because of the presence of hemicellulose and cellulose in this sample. This peak shifts to a higher temperature of 365°C following the extraction and the doublet disappears, instead a shoulder is observed at around 320°C. This not only shows the enrichment of cellulose content in CCs following alkaline extraction but also the presence of some hemicellulose despite the alkaline extraction. In other words, not all the hemicellulose was extracted from CCs following the alkaline extraction according

to the TGA results, which is in complete agreement with the results obtained from FTIR spectra of the same materials.

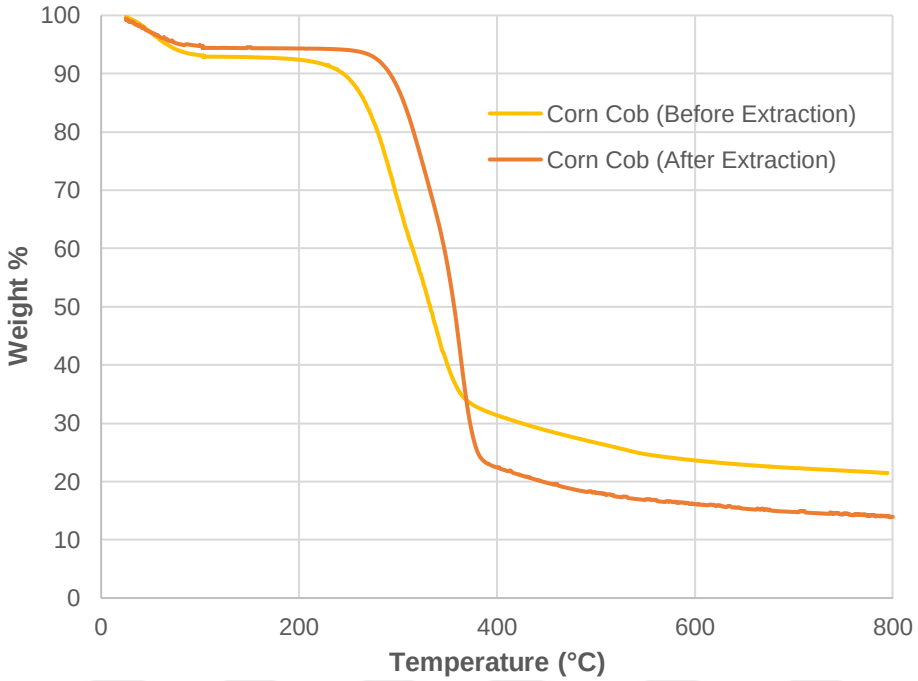


Figure 5.16 Weight loss curves for CC before and after alkaline extraction obtained by TGA.

Weight loss curve for the gel extracts together with the hemicellulosic paste is given in Figure 5.17. The first thing that can be noted here is that the weight loss curves for both specimens resemble each other where the decomposition takes place in a very broad temperature range. As mentioned in the discussion related to Figure 5.15, presence of lignin in both samples is responsible for this broad decomposition range. The onset temperatures for both samples are very close to each other with 247°C and 249°C for the gel extract and hemicellulosic paste, respectively. According to the peaks observed in the 1st derivative of the weight loss curve, both samples have two regions in which there was a rapid weight loss. The rate of weight lost (%/min) was highest for both samples at around 265°C, which is due to the decomposition of hemicellulose in the samples. The highest rate of weight loss was observed at 262°C and 278°C for the gel extract and the hemicellulosic paste. A second broader 1st

derivative weight peak with a smaller %/min value compared to the first one was also observed for both samples at around 450°C, which is related to lignin decomposition, further validating the presence of lignin in the samples in accordance with the FTIR results. This second peak related to lignin pyrolysis, which was discussed earlier related to alkaline lignin, appears at 445°C and 465°C for the gel extract and the hemicellulosic paste. One final important remark related to the TGA of these samples is related to the amount of material remaining at 800°C, which is around 40% for both samples. This is a result of the inorganic content in the samples although this inorganic content is different for the hemicellulosic paste and the extracts. While obtaining the paste, the polymers solubilized in KOH solution are precipitated by the addition of acetic acid and ethanol solution. Because of the acid base reaction during precipitation, KAc salt was produced, and it is retained together with the polymers to a certain extent. On the other hand, the inorganic content related to the gel extract is KOH since there is no precipitation stage in this process unlike the one carried out for the hemicellulosic paste.

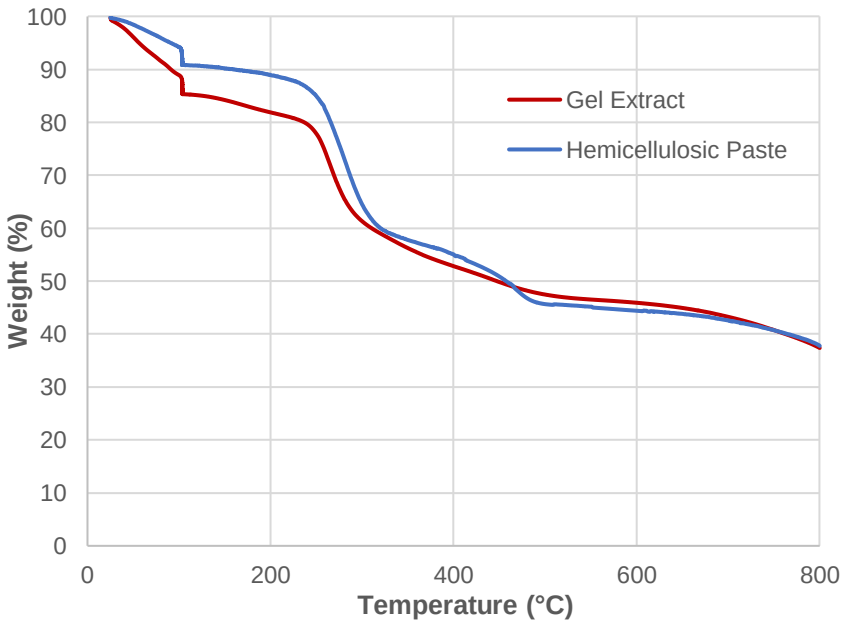


Figure 5.17 Weight loss curves for gel extracts and hemicellulosic paste obtained by TGA.

5.5 Mechanical properties of the CC extract

To understand the mechanical properties of materials printed from the gel extracts, dog bone shaped specimens were 3D printed. The dog bone shaped specimens were printed in a parallel direction to the dimension in which the force was applied during tensile testing to prevent any underestimation that might arise if the printed lines were misoriented to the direction in which the force was applied.

The gel extract based materials had relatively low eb values of 1.6 ± 0.4 %. Considering the hydrophilic nature of hemicellulose found in these materials together with the presence of KOH, a plasticization due to the absorbed water content could be expected but this does not seem to be taking place in these materials when this relatively low eb value is considered. The UTS and E values were 7.2 ± 2.0 MPa and 653.7 ± 154.4 MPa, respectively.

5.6 Rheological properties of CC extracts

Rheological properties of polymers are of major importance related to their 3D printability (Das et al., 2021). In order to show the influence of water content and temperature on the viscosity of the extracted samples from the CCs, both the steady-state flow and oscillation tests were planned for the samples. However, the steady-state flow mode measurements could not be conducted successfully since the samples pour out (overflow) of the measuring apparatus (co-axial cylinder) during the measurements especially at high shear rates. Therefore, only the oscillation tests were conducted to characterize the rheological behavior of the gel samples. As shown in complex viscosity against angular frequency results (Figure 5.18A), both the water content and temperature of the CC extracts had a significant influence on the complex viscosities of the samples.

The power law model given below is widely used to represent the relationship between apparent viscosity and shear rate. The complex viscosity (η^*) as a function of angular frequency (ω) can also be represented by the power law as follows:

$$\eta_{app} = k\,\dot{\gamma}^{n} \qquad (5.1)$$

$$\eta^{*} = k'\omega^{n'} \qquad (5.2)$$

where k′ can be considered as the flow consistency index and n′ as the flow behavior index. The values of k′, n′ and η* at 10 rad/s for the samples are given in Table 5.1. The R^2 values for the power law fitting are also included in Table 5.1. R^2 values ranging from 0.974-0.999 suggests that the power law model is an appropriate model to represent the measured complex viscosity values. Both the flow consistency index and the flow behavior index of the samples were influenced strongly with the water content of the samples and temperature. The comparison of k' at different n' values is not ideal, therefore, the complex viscosity values at an angular frequency of 10 rad/s was compared. The η* at 10 rad/s value of the sample with a water content of 68% at 35°C was about 15-fold higher than that of the sample with a water content of 83%. The difference between the η* at 10 rad/s values were increased further with increasing temperature and it became about 50-fold at 55°C as shown in Figure 5.18B.

Table 5.1 The values of k′, n′ and η* at 10 rad/s for the samples with a water content of 68% and 83% at various temperatures ranging from 35°C to 55°C.

	Water Content = 68%				*Water Content = 83%*			
T, °C	*k', Pa.s^n*	*n'*	*R^2*	*η* (Pa.s) (at 10 rad/s)*	*k', Pa.s^n*	*n'*	*R^2*	*η* (Pa.s) (at 10 rad/s)*
35	248.3	0.272	0.998	43.86	12.1	0.414	0.996	2.94
40	186.0	0.293	0.997	34.34	3.0	0.595	0.999	1.15
45	115.1	0.340	0.997	23.56	1.2	0.725	0.991	0.69
50	84.4	0.378	0.998	19.11	0.5	0.812	0.974	0.33
55	46.7	0.453	0.999	12.97	0.4	0.828	0.976	0.26

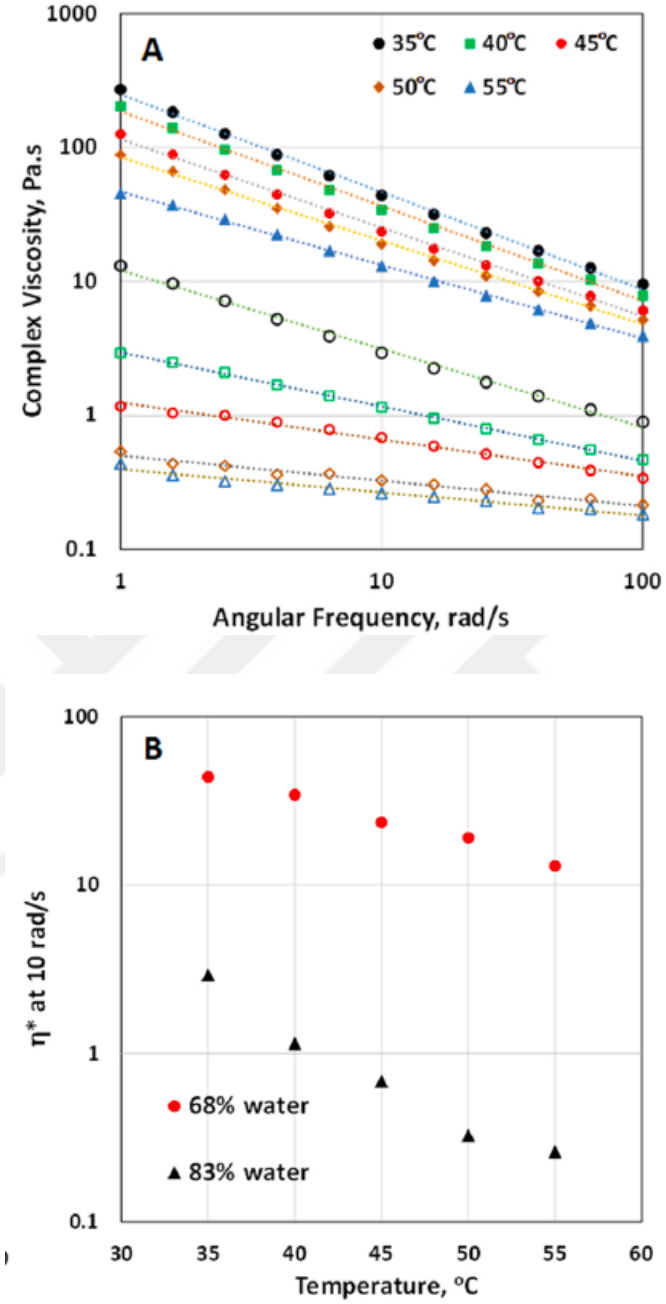


Figure 5.18 (A) Complex viscosity against frequency for the CC extract gel samples containing 68% and 83% water at various temperatures ranging from 35°C to 55°C. Solid symbols represent the results for 68% water content and open symbols represent results for 83% water content. (B) Complex viscosity at 10 rad/s against temperature for the gel samples containing 68% and 83% water.

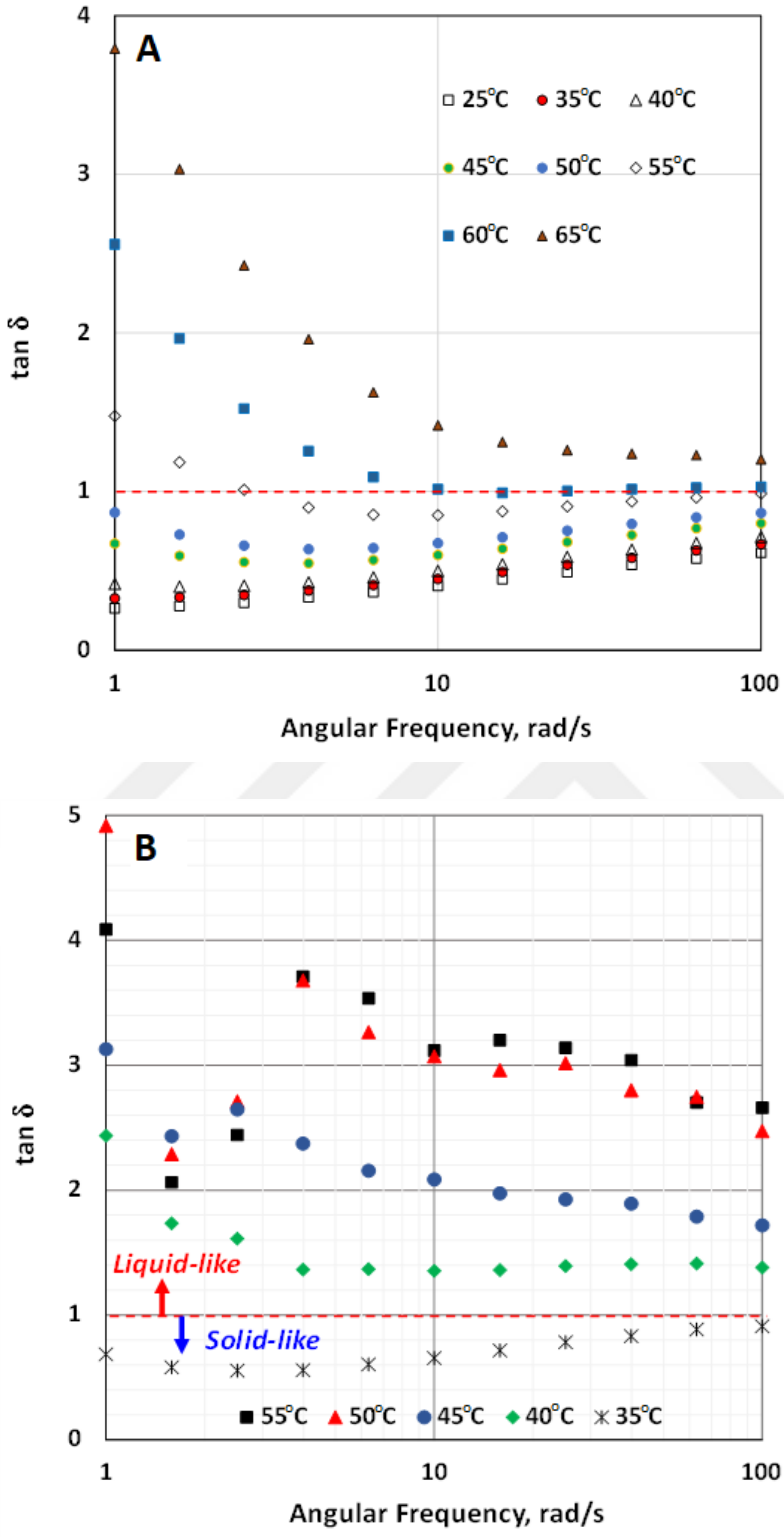


Figure 5.19 tan δ versus frequency for the CC extract gel samples at various temperatures containing (A) 68% water and (B) 83% water.

The tan δ versus frequency curves for the extract samples with the water contents of 68% and 83% at various temperatures are shown in Figure 5.19. tan δ value increases with increasing temperature for both samples containing 68% and 83% water, suggesting that the samples became more liquid-like (viscous) materials as the temperature was increased since the tan δ is defined as the ratio of loss modulus (G'') to storage modulus (G'). For the samples with 68% and 83% water contents, the tan δ values were greater than 1 at temperatures above 55°C and 35°C, respectively, suggesting that these samples transform from a gel-like structure with predominantly elastic behavior to a liquid-like material with predominantly viscous behavior when their temperatures were increased. The rheological properties of the CC extract samples suggest that they are thermoreversible gels in accordance with the observations made during the 3D printing experiments.

5.7 SEM analysis of the 3D printed models from CC extract

The appearance of the models, which were printed from the CC extract with a water content of 83% at 4 different temperatures, following the immersion to the ethanol bath and drying at ambient conditions for 24 hours are shown in Figure 5.20. Upon drying all the printed models shrunk approximately by 30%. This value was calculated by measuring the three dimensions of the models with a micrometer upon their drying and comparing the final volume with the initial volume of the models. This change in the dimensions of the models is because of their significant water loss. The models were printed from a gel with a water content of 83% but the water content of the dry models was approximately 14% following the immersion to the ethanol bath and subsequent drying steps. The model printed at 45°C had the best overall structural integrity among the dry models.

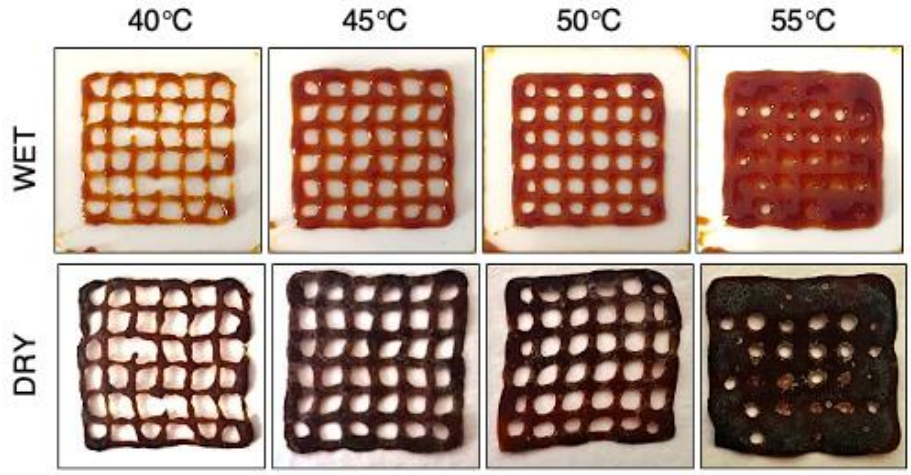


Figure 5.20 Appearance of the wet and dry models 3D printed from the CC gel extract with a water content of 83% at four different printing temperatures.

Figure 5.21 shows the SEM images of the dry grid model printed from the CC extracts at 45°C. The cross-section of the model appears homogeneous and rather defect-free without any obvious imperfections (Figures 5.21A, B). The grid model consisted of 4 layers, but these layers were not visible in SEM most likely because the CC extract was in the form of a highly viscous liquid rather than a gel at 45°C as it was deposited onto the previously built layer. Another feature related to the cross-section SEM images of the grid model is the crystal deposits that can be observed on the surfaces on the model. As shown in Figures 5.21C, D, the surface of the grid model is completely covered with these crystals, which might be related to the potassium content of the models due to the presence of KOH. The presence of KOH crystals might be undesired for certain applications of this 3D printing strategy such as the printing of scaffolds for biomaterial applications. In this context, removal of KOH from the surface of the samples might be possible by washing the printed samples with ethanol upon their drying since KOH is soluble in ethanol.

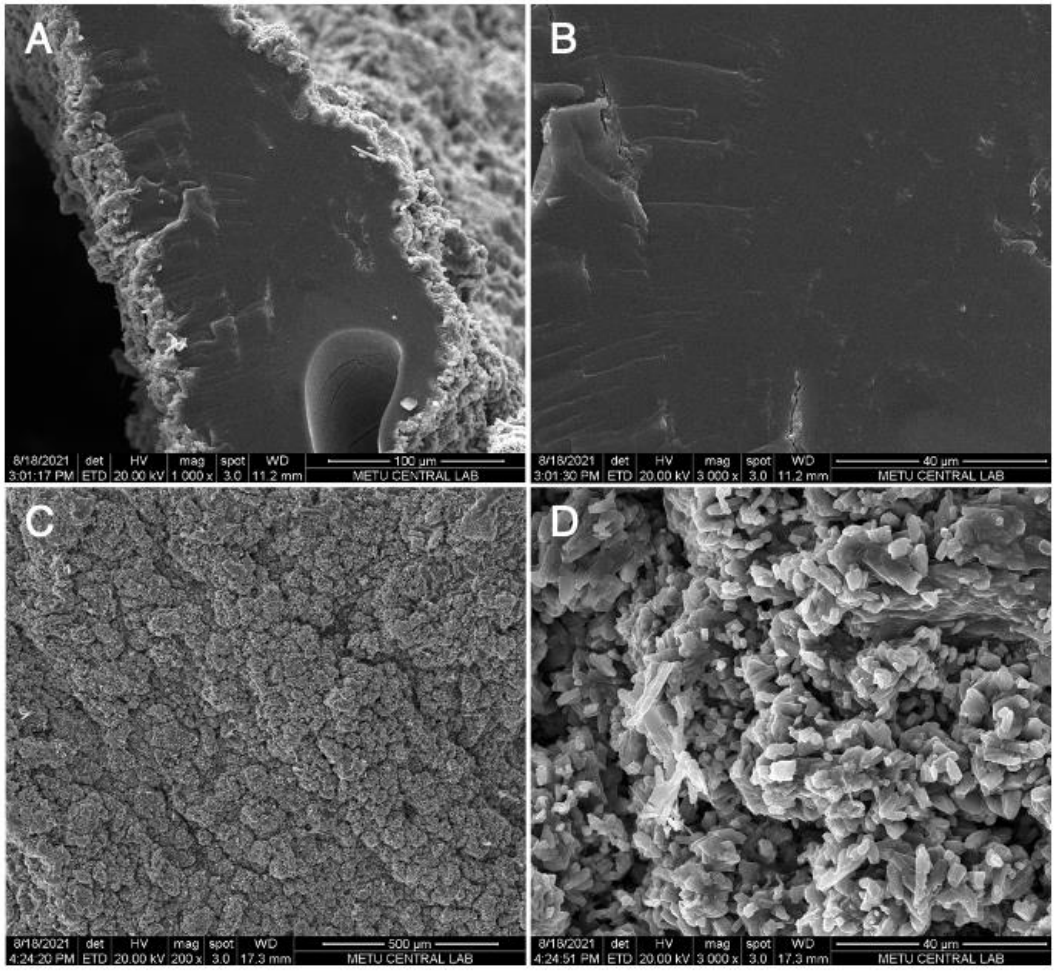


Figure 5.21 (A, B) Cross-section and (C, D) surface SEM images of the dried grid model printed at 45°C.

CHAPTER 6

3D PRINTING OF FILAMENTS OBTAINED FROM HEMICELLULOSIC PASTES AND CC EXTRACTS TOGETHER WITH PVA

Different than the previous phases of the thesis study, which focused on the 3D printing of pastes and gel extracts, the current chapter covers the 3D printing of filaments obtained from blending the hemicellulose and lignin biopolymers with PVA. As a water-soluble thermoplastic polymer, PVA is an ideal candidate to be mixed with hemicellulose and lignin and its non-toxic and biodegradable properties make it a perfect match for the approach followed so far in the thesis study. A capillary rheometer was used to obtain the filaments from the blends containing hemicellulosic pastes, extracts and PVA at different concentration at temperatures around 170°C – 200°C depending on the formulation of the blends. Several formulations were prepared and tested for their 3D printability including blends that contain 15% - 50% hemicellulose and lignin-based biopolymers in addition to PVA.

Despite the different approach presented in this chapter, which relies on the 3D printing of filaments, the approach here also relies on the information generated in the previous chapters since hemicellulose and lignin containing pastes and extracts were still obtained from CCs by alkaline extraction and they are blended with PVA. There are various reasons for choosing PVA among many available polymers for blending with the pastes and the extracts. First of all, PVA is a water-soluble polymer, and this enables better mixing with the pastes and the extracts. Second, PVA is a biodegradable polymer, and this perfectly fits with the approach of the thesis study since using a polymer which is not biodegradable would contradict with one of the most important aspects of the materials developed in the study, which is being environmentally friendly. PVA was also chosen from a processing point of view since it is a thermoplastic polymer unlike hemicellulose and lignin and using

PVA enables having a thermoplastic blend. This is obviously very important if you want to obtain filaments and use these filaments in 3D printing.

6.1 Preparation of blends containing hemicellulosic pastes and CC extracts together with PVA

Blends prepared in this phase of the thesis study can be divided into 2 groups. The first group consists of hemicellulosic pastes (HP), which were the biopolymers used in the earlier (initial) stages of the thesis study, blended with PVA at different fractions. There are 2 different types of HP that are blended with PVA. The first type denoted as HP contains KAc salts, which are formed because of the alkaline extraction and the subsequent precipitation step. The second type of hemicellulosic paste used for blending with PVA is washed with a solution of ethanol and water to remove the KAc salts prior to blending with PVA, which is named as desalted hemicellulosic pastes (d-HP).

The second group of biopolymers blended with PVA is the CC extract, which was used in the later stages of the thesis study for 3D printing. As discussed in the previous chapters, the extract is basically a concentrated form of the alkaline solution obtained from the extraction of CCs and there are no precipitation stages involved with it and thus it does not contain KAc salts. The extract also has a higher lignin content, and it is thus darker in color compared to HP again because the precipitation stage is by-passed during the procedure used to obtain the extract.

Blending the HP or the extract with PVA was simply conducted by mixing the polymers separately and then adding the mixtures to the same beaker. During the mixing experiments, the temperature was set to 60°C. Once the mixing was completed the mixtures were poured into petri dishes with a diameter of 9 cm and dried at 40°C for 2-3 days until films were formed. In other words, solvent casting technique was used to obtain films from the blends, which worked fine for both the HP and CC extract containing films as shown in Figures 6.1 and 6.2. Blending CC

extract with PVA instead of HP resulted in the formation of stiffer films, which was most likely due to the presence of additional lignin compared to the HP since it was previously shown that increasing the amount of lignin in hemicellulose-based films had a significant impact on mechanical properties by decreasing the % elongation at break and increasing the elastic modulus (Bahcegul et al., 2012). The films were cut into smaller pieces and fed to the capillary rheometer and filaments were obtained, which were used to 3D print various shapes.

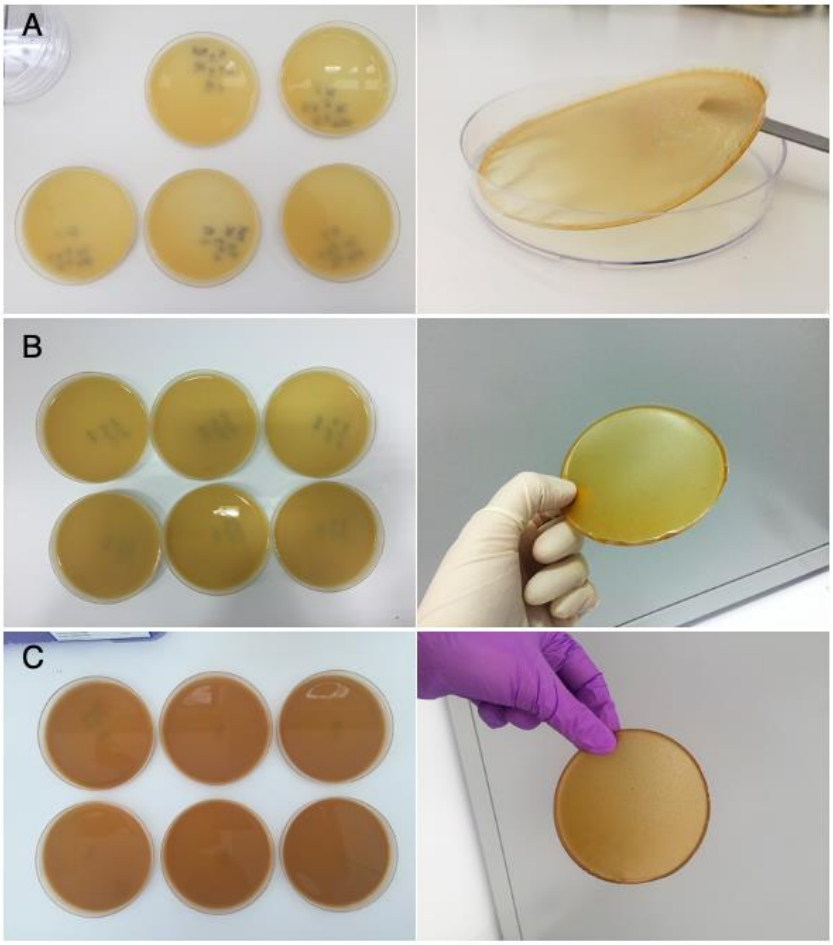


Figure 6.1 HP/PVA films with 15% (A), 25% (B) and 40% (C) HP concentrations.

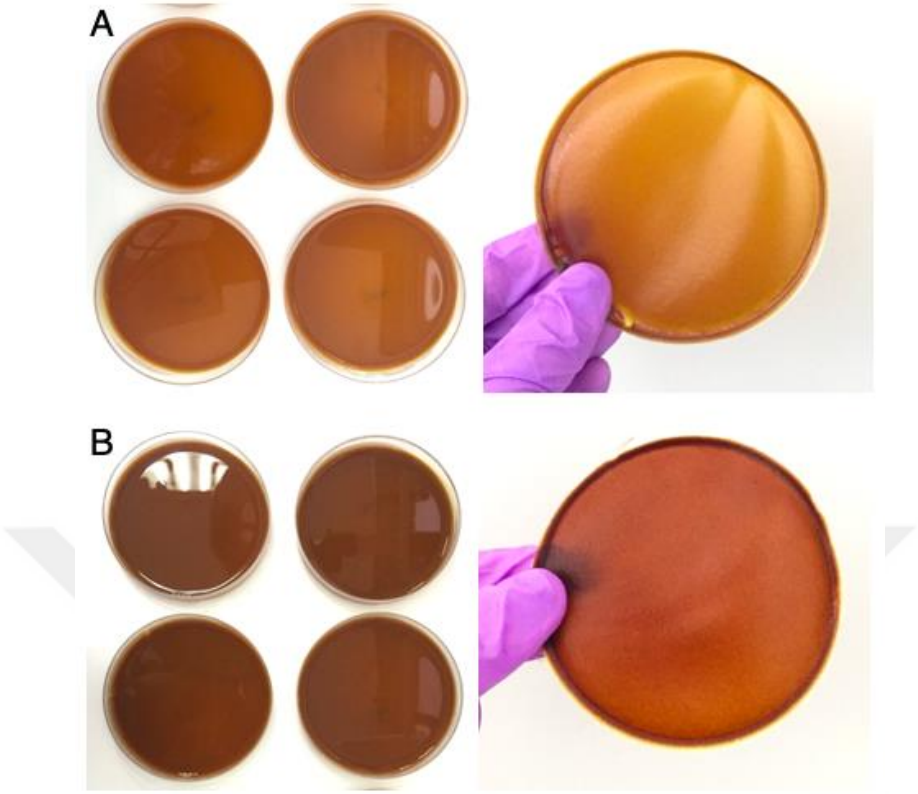


Figure 6.2 CC extract/PVA films with 25% (A) and 40% (B) extract concentration.

In addition to films containing HP and CC extract together with PVA, films containing d-HP were also prepared. As mentioned earlier, the HP contains the salt KAc that form during the precipitation (neutralization) step. In order to understand if the presence of this salt might have any adverse effects during the filament fabrication and 3D printing steps, this salt was removed from the paste by consecutive washing steps and a desalted hemicellulosic paste (d-HP) was obtained and mixed with PVA to obtain films, just like it was done with HP and CC extracts.

As shown in Figure 6.3, homogeneous intact films were formed when d-HP was blended with PVA with a d-HP content of 25%. However, when the desalted paste ratio was increased to 40%, films with a fragmented structure that resemble islands were obtained. Such a fragmented structure was not the case for the salted films with the same (40%) hemicellulosic paste content.



Figure 6.3 Appearance of dry 25% d-HP/PVA, 40% d-HP/PVA and 40% HP/PVA films.

In order to avoid the discontinuous appearance with fragmentation upon drying in 40% d-HP/PVA films, the fragmented films were dissolved again water and the blend was further concentrated by reducing its water content by 50%. This time, 40% d-HP/PVA was poured into petri dishes as a high-viscosity solution and this approach led to a continuous film as shown in Figure 6.4B instead of the fragmented film (Figure 6.4A), which was obtained with a lower viscosity film forming solution.

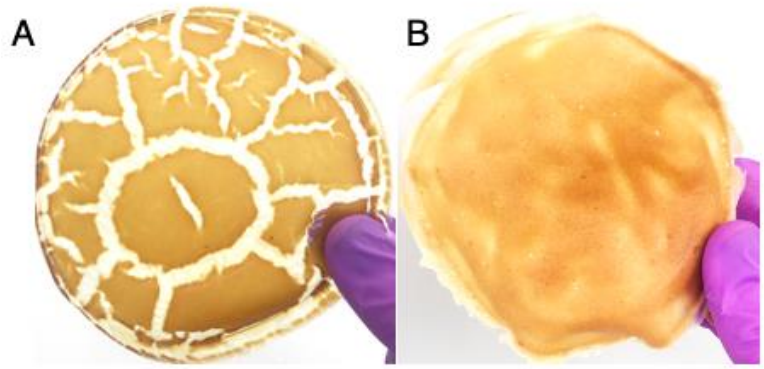


Figure 6.4 Films obtained from low viscosity (A) and high viscosity (B) d-HP/PVA solutions containing 40% d-HP.

6.2 Fabrication of filaments used in 3D printing

Once the solvent casted films described in the previous section were obtained, they were chopped into smaller pieces and fed to a capillary rheometer in order to obtain filaments to be used during 3D printing. This approach mainly relies on forcing the material through a die with a certain speed so that filaments within a specific diameter range suitable to work with the 3D printer can be obtained.

The preliminary trials in the early stages of the filament fabrication experiments involved using films that contain HP at different concentration together with PVA. The filament containing 15% HP had an inhomogeneous structure with bumps and roughness (Figure 6.5A). This might be a result of the recycling performed with this filament since this roughness was not observed at a higher concentration of 25% HP obtained in a single run. The recycling was made in order to determine if better filament fabrication parameters could be employed during the experiments.

25% HP/PVA blend filament was smooth and had a homogeneous structure (Figure 6.5B) while the filament with 40 wt.% HP had a rough surface full of bubble-like structures and the filament diameter varied considerably (Figure 6.5C). This filament was also much softer compared to filaments containing 15 and 25% HP.

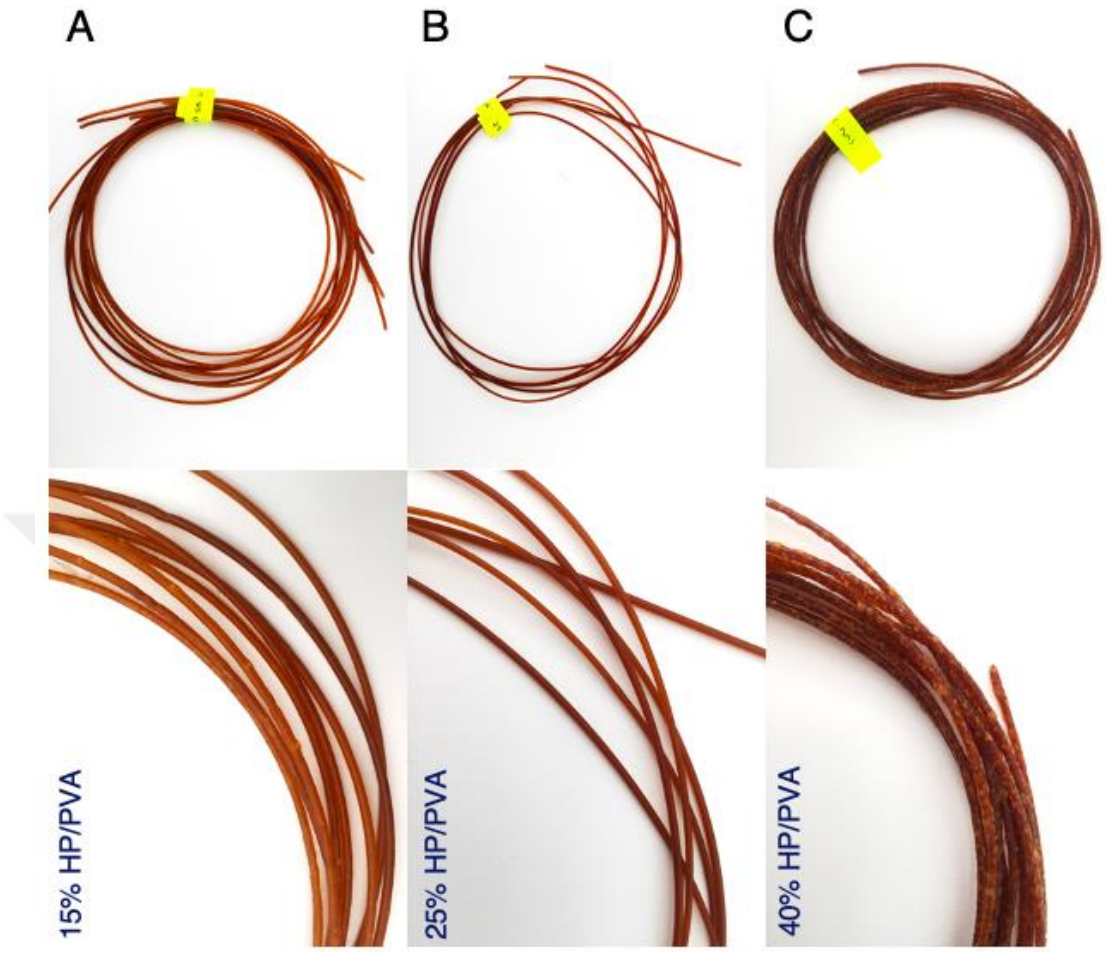


Figure 6.5 Appearance of HP/PVA filaments with 15% (A), 25% (B) and 40% (C) HP concentrations.

Since the 40% HP/PVA filament had a rough and inhomogeneous surface, filament fabrication experiment was repeated by doubling the amount of water in which the HP was dispersed and increasing the basicity of the hemicellulosic solution to improve the HP-PVA blending by increasing the solubility of HP. However, extruded filaments were like the previously fabricated ones as they still had a rough and bulbous structure (Figure 6.6A). Light-colored bubbles were observed on the filament surface as can be seen in Figure 6.6B and when the filament was cut from these parts, it was observed that the inner part was empty (Figure 6.6C). Hence, these bulbous structures are considered to be air bubbles which was formed when the water

remaining in the sample suddenly evaporated at the filament formation temperature, which was 170°C, as it exits the die of the capillary rheometer. The retained water in blend formulation might be released at a higher temperature if a chemical relationship rather than a physical one is established between the polymers. Therefore, this water content may not be detected at 120°C at which the moisture content measurement was made. It was also observed that the filaments became smoother as they were kept in the rheometer for a while with temperature since their water content decreases. Based on these findings, a drying step at a temperature higher than 120°C was added to the process that takes place just before the filament fabrication to understand whether the problems in the filament structure were due to the poor mixing of the polymers or the water retained in the blends.

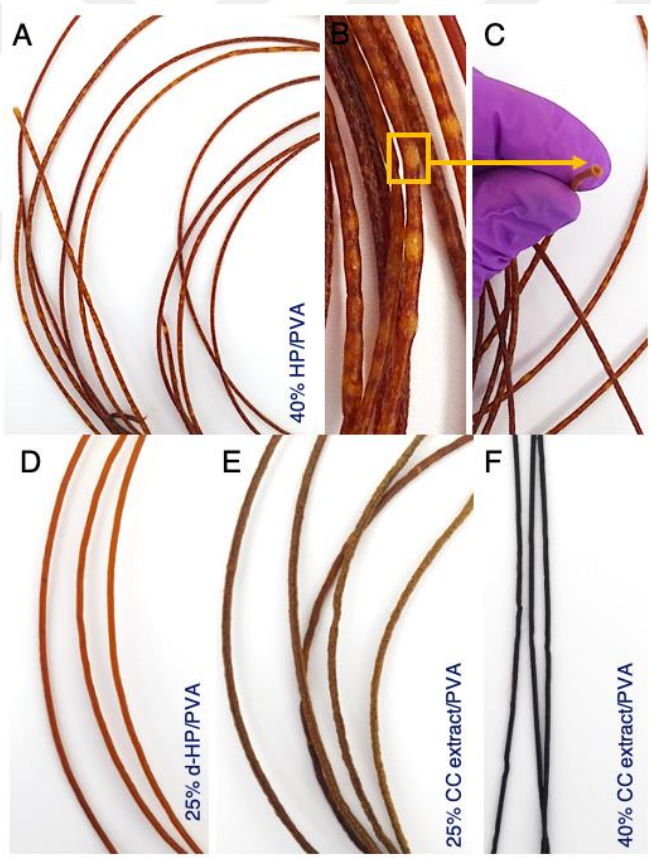


Figure 6.6 Appearance of 40% HP/PVA filament (A), defects and bulbous structures on the filament surface (B), voids inside the filament (C). 25% d-HP/PVA filament (D), 25% CC extract/PVA filament (E), 40% CC extract/PVA filament (F).

As mentioned earlier, desalting of HP was performed in order to understand if removing the salts can cease the formation of the undesired bulbous structure obtained with the salt containing HP. Compared to the HP containing blends that also included the salt KAc, d-HP containing blends had a higher viscosity and the temperature during the filament fabrication experiments increased due to this reason so that the material could be extruded out of the rheometer's die. Overall, the 25% d-HP/PVA filament was homogeneous and smooth (Figure 6.6D).

In addition to HP and d-HP containing filaments CC extract containing filaments were also fabricated following the same approach. As shown in Figure 6.6E, the surface of 25% CC extract/PVA filaments looked spongy and rough. It was observed that this filament swelled much more as it leaves the rheometer's die compared to paste containing filaments and thus a filament with a much thicker diameter than intended was obtained. Piston speed was reduced to 10-11 mm/min from 27-28 mm/min to decrease the filament diameter. Reducing the speed led to a filament with a smaller diameter as intended while the filament's structure was still the same with an undesired roughness.

As this spongy/rough filament structure might be caused by the water content of the material, 40% CC extract/PVA blend was subjected to drying at 170°C for 20 minutes just before the filament fabrication experiment. This drying strategy led to a smooth filament as shown Figure 6.6F.

The softness and rough structure of filaments containing 25% extract is probably due to the fact that these filaments are much more porous than filaments containing 40% extract as there was about 30% difference between the densities of both filaments, which was determined by measuring the filament's weights and calculating their volume. The density of the filaments containing 25% extract was lower than that of filaments containing 40% extract.

Based on the observations related to the preliminary experiments discussed above, it was determined that a drying step performed at an elevated temperature of 170°C, which is a temperature close to the processing of the polymers inside the capillary

rheometer, was essential in order to obtain filaments without any major defects. In this sense, all the filaments were fabricated with this approach. In other words, chopped films were heat treated in an oven at 170°C for 20 minutes before they were placed into the barrel of the capillary rheometer for the fabrication of filaments that will be used in 3D printing. As shown in Figure 6.7, this approach leads to the fabrication of defect free filaments, which was not possible when the heat treatment step was missing as it was observed with the filaments containing 25% CC extract or 40% HP together with PVA. With this strategy, filaments containing up to 50% HP could be produced successfully. Based on these results, it is apparent that the heat treatment applied to the polymer blends performed at an elevated temperature prior to the fabrication of filaments removes the undesired effects of the water trapped inside the polymers. In addition to heat treatment, slightly higher temperatures were employed during the filament fabrication to prevent the wavy appearance of the filaments. The higher filament fabrication temperatures translate into less pressure requirement from the capillary rheometer, reducing this wavy appearance.

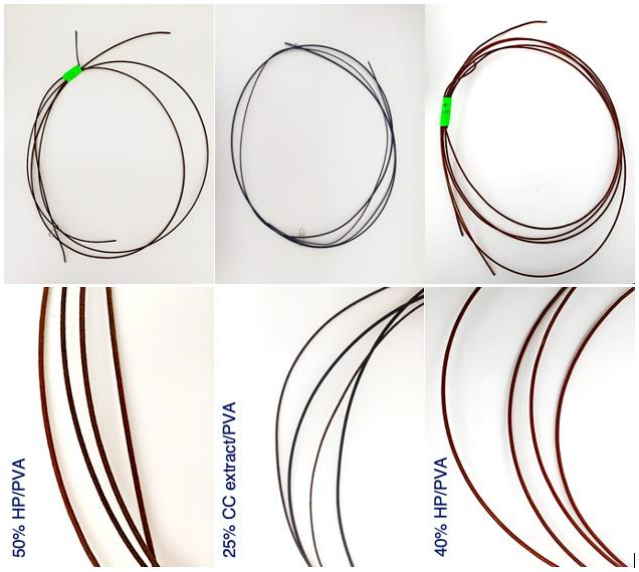


Figure 6.7 Appearance of filaments containing HP and CC extract fabricated with a drying step performed at 170°C for 20 minutes prior to processing with the capillary rheometer.

The intended filament diameter during the filament fabrication experiments was 1.75 ± 0.05 mm. Considering the expansion of the polymers in our study, a capillary rheometer die with a diameter of 1.524 mm was selected. Indeed, as shown in Table 6.1, considerable expansion of the polymers took place as they exit the die and some differences in the filament diameters took place. An important reason for the differences in the filament diameters was that the filament fabrication process was conducted manually.

Table 6.1 Diameters of filaments fabricated from different blends.

Blend Formulation	*Filament Diameter (mm)*
15% HP/PVA	1.65 ± 0.07
25% HP/PVA	1.66 ± 0.05
40% HP/PVA	1.64 ± 0.02
50% HP/PVA	1.77 ± 0.08
25% d-HP/PVA	1.60 ± 0.02
40% d-HP/PVA	1.59 ± 0.03
25% CC extract/PVA	1.88 ± 0.09
40% CC extract/PVA	1.75 ± 0.03

6.2.1 Viscosities of samples used for filament fabrication

In order to show the influence of water content on the viscosity, 25% HP/PVA blends with various water contents were prepared. As shown in Figure 6.8, the apparent viscosity at a shear rate of 10 s^{-1} decreases by around 6-fold with increasing water content from around 1% to 8% as expected. PVA, 25% HP/PVA and 40% d-HP/PVA blends had similar water contents, which were < 2% following the conditioning at the same environment and the different apparent viscosities of these samples clearly show that increasing the hemicellulose content of the blends also increases their viscosity since pure PVA samples had the lowest viscosity while samples with 40%

desalted HP had the highest among all the blends. Having 25% HP together with PVA increases the apparent viscosity by around 3-fold while further increasing the HP content to 40% by using the desalted samples further increases the viscosity by approximately 5-fold compared to samples containing only PVA. When desalting was not applied and blends containing KAc was used, which was the case for the 40% HP/PVA, a higher equilibrium water content of around 6% compared to the other three blends was obtained as expected due to the presence of the KAc salt, which is very hygroscopic. This higher water content eventually led to a lower apparent viscosity compared to the desalted blends that had the same paste content of 40%.

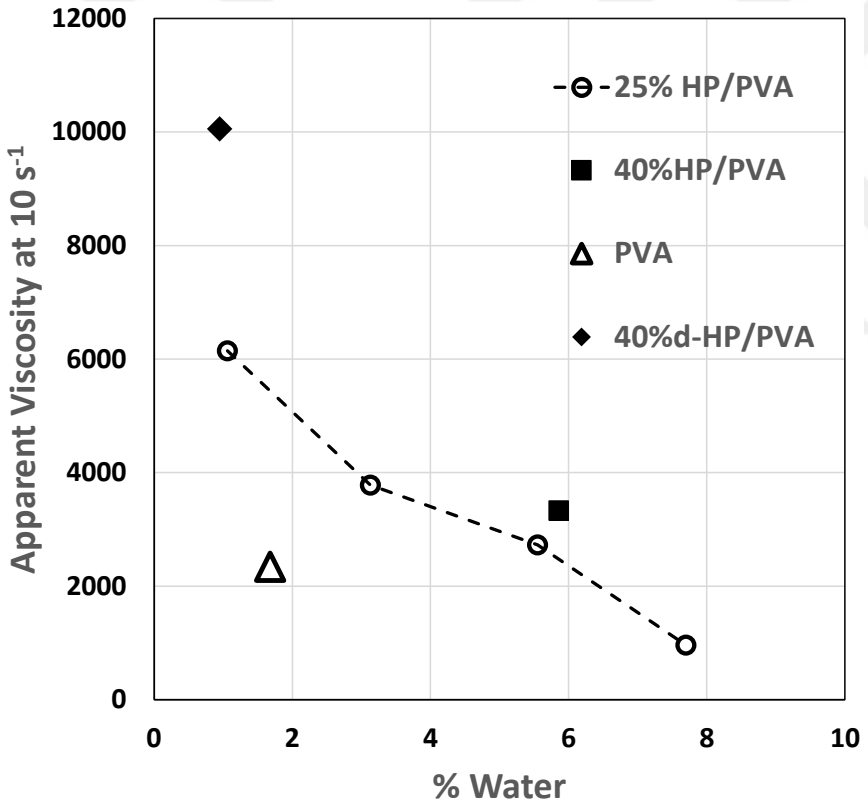


Figure 6.8 Apparent viscosity at a shear rate of 10 s^{-1} against water content for PVA and HP/PVA filament materials.

6.3 3D printing of filaments

Instead of the stainless-steel syringe printing head, which was used to print the pastes and the gels obtained from the hemicellulosic paste and the CC extract, respectively, the standard extruder head of the 3D printer was used in 3D printing studies of all the filaments. To evaluate the printability of different blends, grid models were printed with the printing parameters provided in the Table 6.2. Since thermoplastic behavior is the major concern related to printing of filaments, the ideal printing temperature of the thermoplastic polymer PVA was considered, which is around 200°C. In this sense, printing temperatures between 170 to 200°C were used during the 3D printing experiments. In addition to printing temperature, another important parameter is the temperature of the build platform related to the adhesion of the first layer of the model to be printed. Glass build platform was heated to 75°C during the printing experiments.

Table 6.2 3D printing parameters of the paste and the extract containing filaments.

Extruder	
Nozzle diameter (mm)	0.40
Layer height (mm)	0.20
Extrusion multiplier	1
Retraction	Off
Speed	
Print speed (mm/min)	1000
XY axes movement speed (mm/min)	6000
Z axis movement speed (mm/min)	1000
Temperature	
Extruder temperature (°C)	170-200
Build platform temperature (°C)	75

Figure 6.9 shows the appearance of grid models printed from different filaments that contain various amounts of HP and d-HP together with PVA. For all the four temperatures tested between 170°C to 200°C, all filaments that contain hemicellulosic pastes together with KAc could be successfully printed without any major differences. It was possible to print filaments that contain up to 50% hemicellulosic paste when KAc salt was present in the samples.

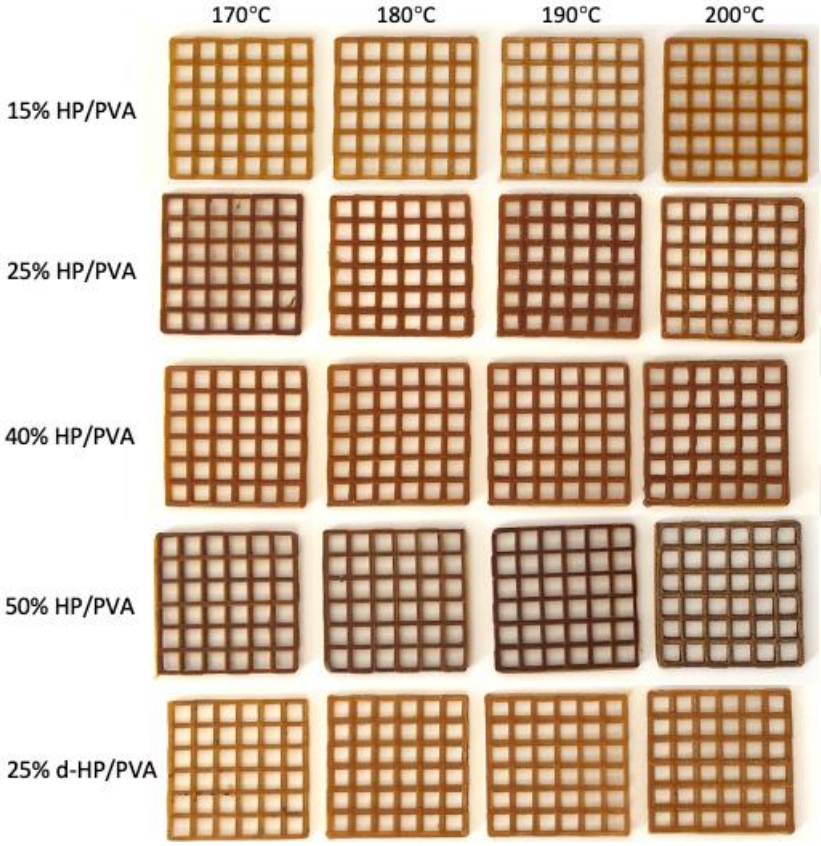


Figure 6.9 Five layered grid models printed from different HP/PVA and d-HP/PVA filaments.

On the other hand, when the samples were desalted, only the filaments that contain 25% hemicellulosic paste could be printed since the filaments containing 40% desalted hemicelulosic paste were too brittle to be successfully 3D printed. The problem here was related to the way in which the filament was forced through the hot end to the nozzle by the 3D printer. As shown in Figure 6.10, the filament is

pressed between two gears, one of which rotates in counter-clockwise direction in order to push the filament to the nozzle through the hot end. When the filament is too brittle, as was the case with the 40% d-HP filament, it breaks right at this point making the further movement of the filament to the nozzle impossible.

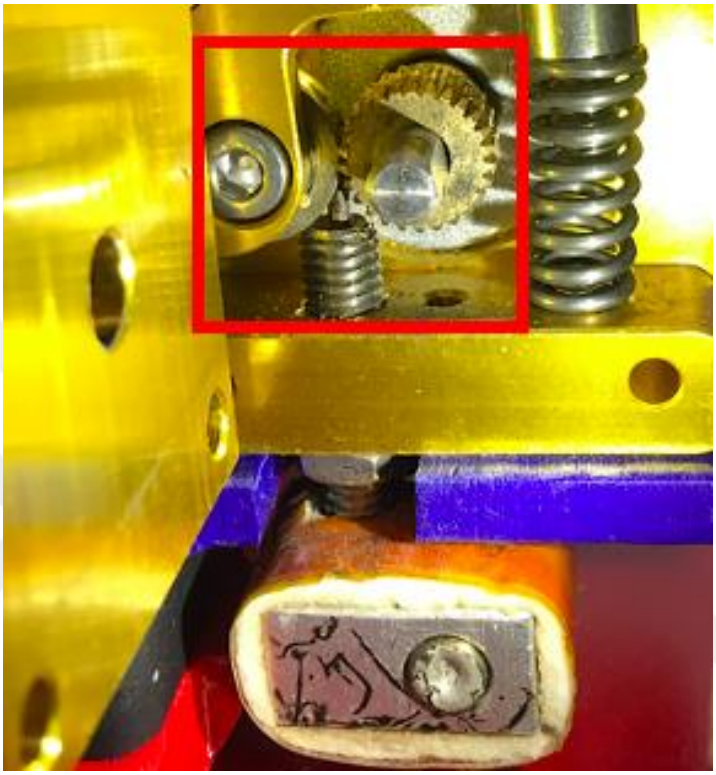


Figure 6.10 Inside view of the 3D printer's extruder head that shows a broken filament in contact with the gear that forces the filament into the hot end up to the nozzle.

The reason for the above-mentioned brittleness is related to the low moisture uptake of this filament. As shown in Table 6.3, filament containing desalted hemicellulosic pastes had a much lower moisture uptake of around 2 - 3% when compared with other filaments that either contained KAc or KOH depending on whether they were obtained from pastes or extracts. The filaments had a stable weight at the end of the 14-day period during which they were conditioned at a RH of 37% ± 3% at 22°C for 14 days to understand their moisture uptake behavior (Figure 6.11). Since water acts as a plasticizer for these hydrophilic polymers, its absence leads to an undesired

brittleness that prevents a successful 3D printing process from taking place. On the other hand, it is also worth mentioning that despite having a lower moisture uptake than d-HP 40%, d-HP 25% was 3D printable. The reason for this is the presence of a higher amount of PVA in this formulation (75% PVA) compared to lower amount of PVA (60%) in the formulation containing 40% desalted hemicellulosic paste. Presence of a higher amount of PVA imparts an increased thermoplastic behavior to the blend, making it printable even at lower water contents. This also evident from the fact that PVA itself, without any other polymers, was 3D printable despite it had the lowest moisture uptake among all the 3D printed samples.

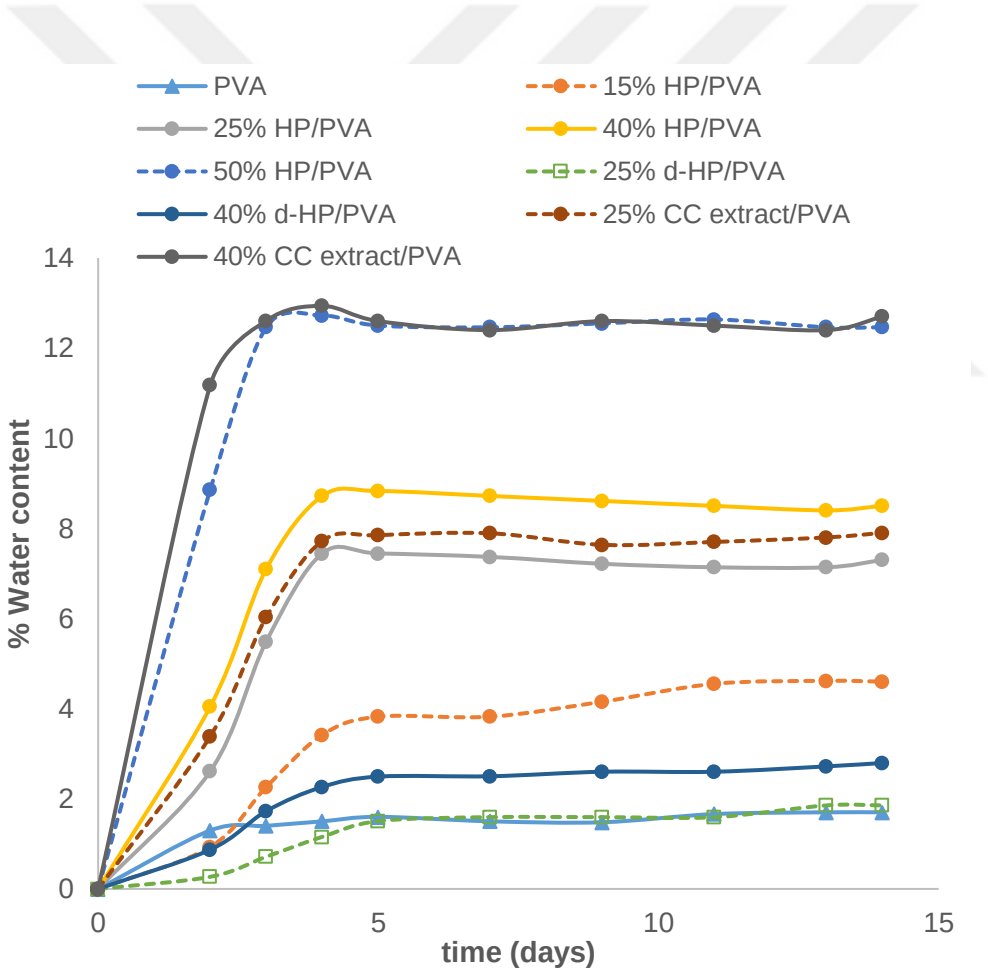


Figure 6.11 Water contents of different filaments with respect to time as they were conditioned at a RH of 37 ± 3% at 22°C for 14 days.

Table 6.3 Moisture uptake values of different filaments conditioned at a RH of 37 ± 3% at 22°C for 14 days.

Sample	*% Moisture Uptake*
PVA	1.70
15% HP/PVA	4.60
25% HP/PVA	7.30
40% HP/PVA	8.50
50% HP/PVA	12.46
25% d-HP/PVA	1.85
40% d-HP/PVA	2.80
25% CC extract/PVA	7.90
40% CC extract/PVA	12.70

Other than brittleness, being too soft might also adversely impact the 3D printability of the filaments. Typically, the filaments were stored in silica gel filled boxes that had a RH value of 15%. However, when exposed to the ambient humidity for prolonged periods of time, filaments became softer due to the plasticization induced by water, and they jammed the extruder again at the site in which the gear forces the filament to the nozzle through the hot end. In other words, filaments that lack the sufficient rigidity could not be printed since these filaments, as they were forced by the gear, were twisted to a spring like form and jammed the extruder (Figure 6.12) after a while since they could not be extruded out of the hot end.

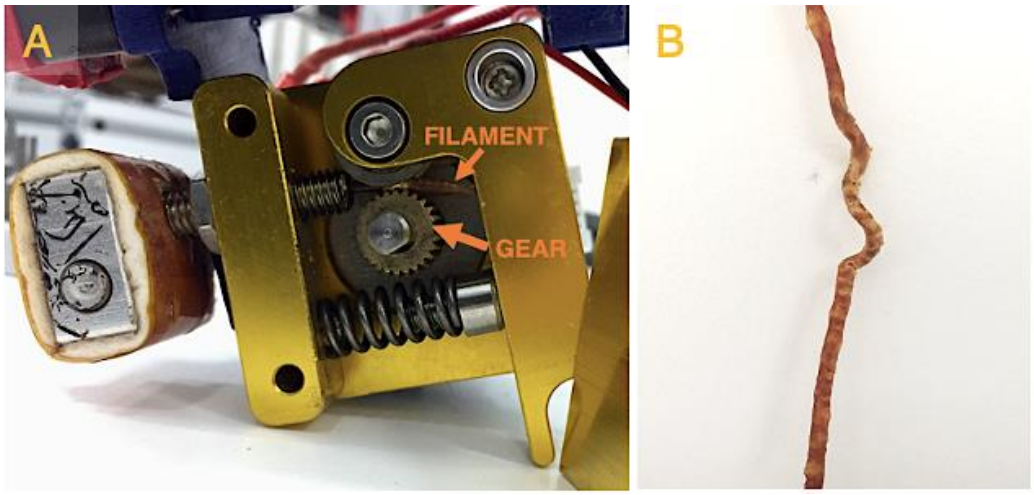


Figure 6.12 Nozzle jam (A) and twisted, spring like filament removed from the jammed nozzle (B).

Other than the paste containing filaments, CC extract containing filaments were also successfully 3D printed as shown in Figure 6.13. Even though these filaments had a diameter up to 1.88 mm, they could still be printed, showing that the process had a rather high diameter tolerance, especially when it is considered that the ideal filament diameter is 1.75 mm.

3D printing experiments of 25% and 40% CC extract/PVA were performed at 190°C and 200°C since these blends could be extruded into filaments at a higher temperature (185 - 190°C) compared to paste containing filaments because of their higher viscosity.

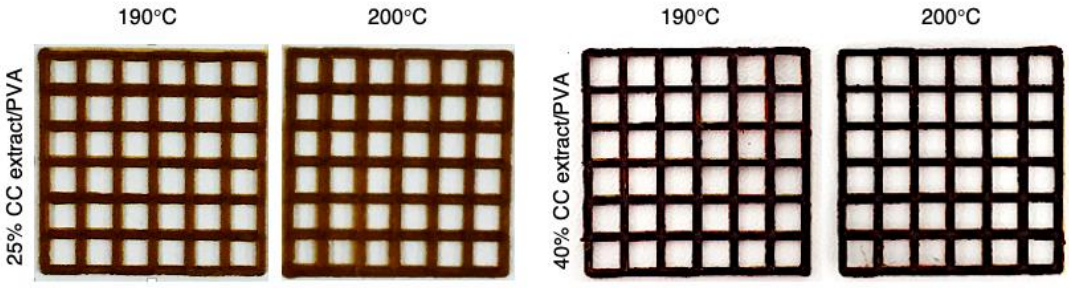


Figure 6.13 Appearance of grid models printed from filaments that contain CC extract together with PVA.

One of the reasons for the selection of grid shapes models was that these enable the calculation of the 3D printability value. 3D printability was calculated for three of the grid shaped models, which had the highest printable HP, d-HP and CC extract contents in addition to pure PVA, since this would give a basis for comparison in terms of the printability value. From another perspective, the most challenging models to print were the models that were printed by using the filaments that that the highest concentration of biopolymers and this was the reason why these three formulations were chosen for the calculation of printability values. As shown in Table 6.4, grid models printed from pure PVA had a printability of 1.044. Taking this as a reference, it can be seen that the other three samples had printability values of 1.072, 0.984 and 9.989 for 25% d-HP/PVA, 50% HP/PVA and 40 CC-extract/PVA, respectively, all of which were inside the printable range of 0.9 – 1.1. These results thus show that all three formulations can be regarded as being 3D printable.

Table 6.4 Printability values calculated from the gird models 3D printed from different blends.

	Average area of a single cell (mm^2)	*% Target (ideal) area*	*Printability*
PVA	5.69 ± 0.26	73.0	1.044 ± 0.062
25% d-HP/PVA	7.28 ± 0.41	69.2	1.072 ± 0.041
50% HP/PVA	6.65 ± 0.46	88.6	0.984 ± 0.033
40% CC extract	6.00 ± 0.51	80.9	0.989 ± 0.031

In addition to the grid models shown above various models with different shapes were also 3D printed in order to demonstrate that it was possible to print complex shapes with this blending approach. In this context a recycling symbol was 3D printed from filaments containing 15% HP at 180°C as shown in Figure 6.14.

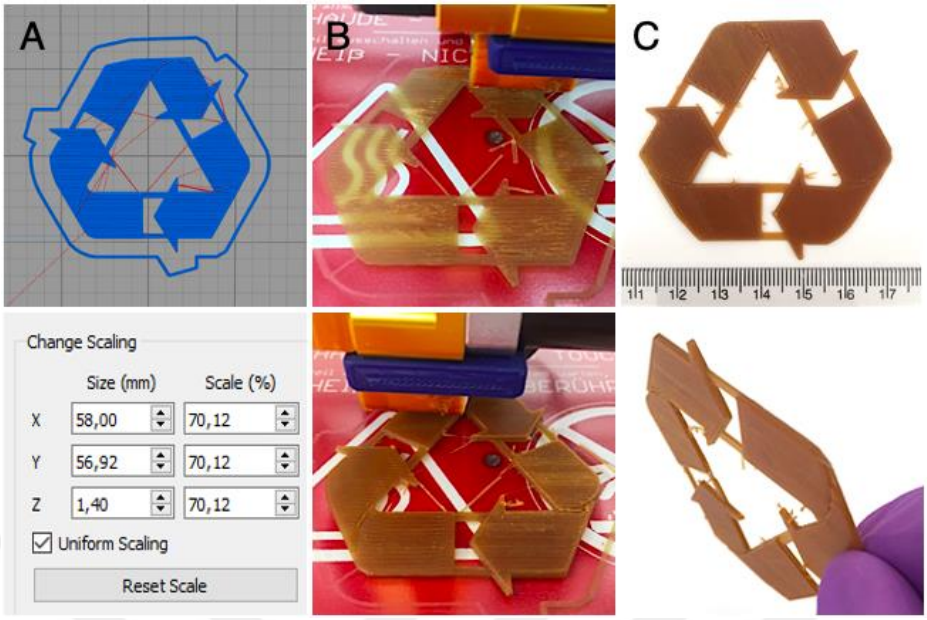


Figure 6.14 Print preview and intended dimensions (A), printing process (B) and printed recycling symbol (C) printed with 15% HP/PVA at 180°C (C).

Another demonstration was made with the 25% d-HP/PVA filament and this time a daisy model consisting of 20 layers was 3D printed as shown in Figure 6.15.

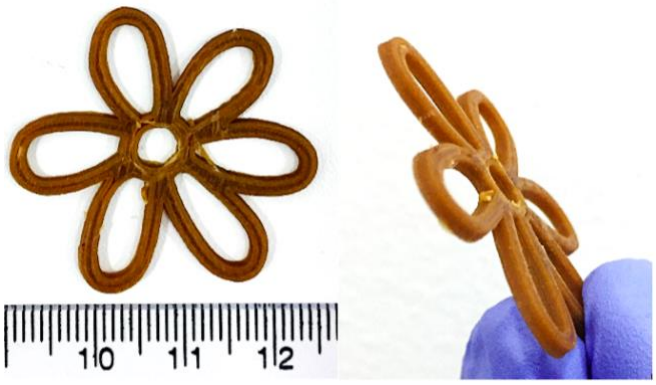


Figure 6.15 A daisy model consisting of 20 layers printed at 180°C with 25% d-HP/PVA filament.

3D printing trials involving more complex models with significantly higher heights (or more layers) were also made. As shown in Figure 6.16, a 75 layered hollow

cylinder, a 98 layered pyramid and a 108 layered polyhedron was printed at a temperature of 180°C from the 25% d-HP/PVA filament.

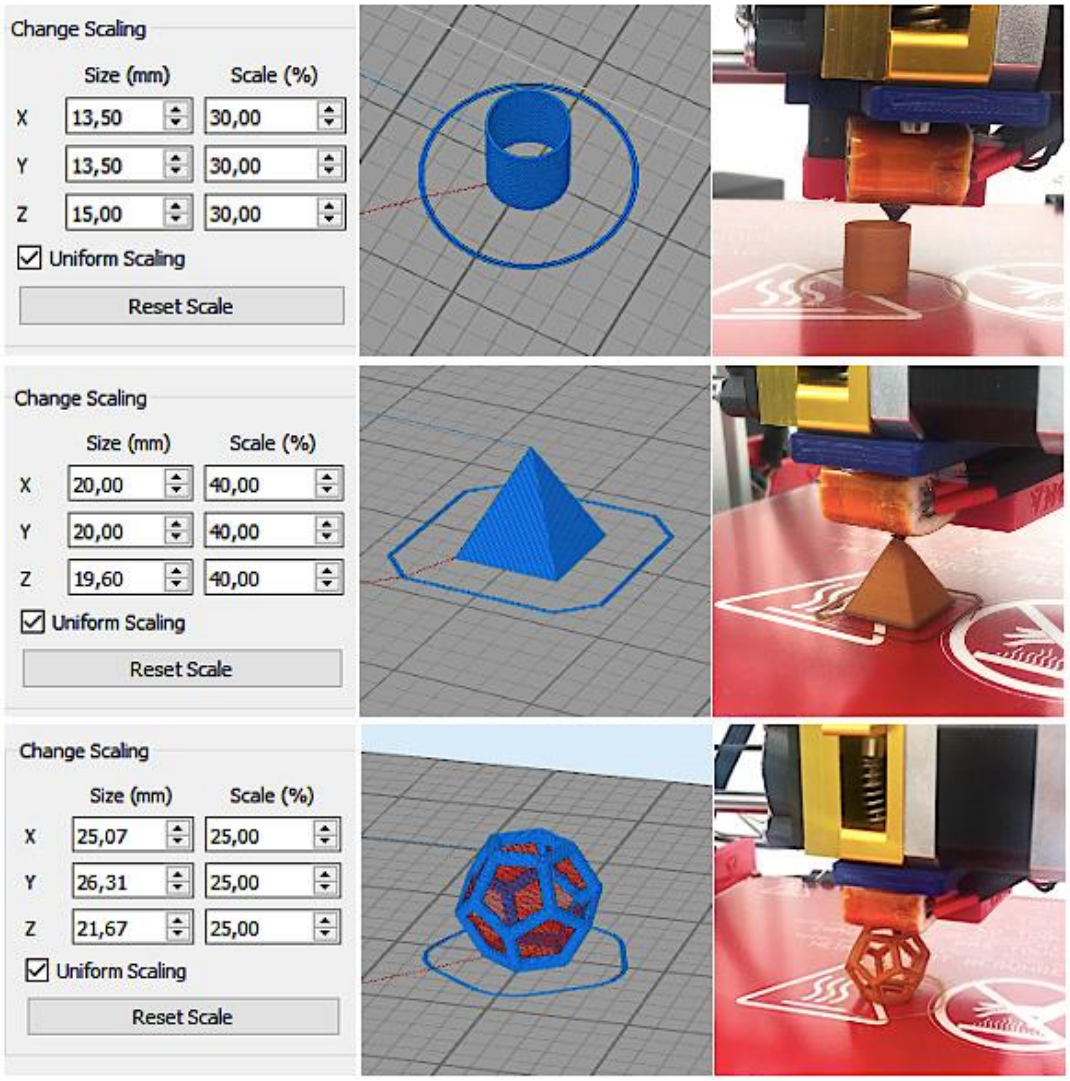


Figure 6.16 Left to right: intended model dimensions, print preview of the models to be printed and 3D models printed with 25% d-HP/PVA filament at 180°C.

6.4 Mechanical properties of 3D printed and solvent cast dog bone shaped samples with different water contents

In order to determine the effect of different blends on the mechanical properties of 3D printed models, dog bone shaped samples were 3D printed from different blends that eventually had different formulations. Solvent cast films were also prepared by dissolving the polymers in water and following the evaporation of water, films were obtained, and dog bone shaped specimens were cut from these films. An essential element related to the determination of mechanical properties was measuring the water content of the samples so that the effect of water content on the mechanical properties of the materials could be observed. This is a very important issue especially with water soluble polymers such as hemicellulose and PVA, which can be highly sensitive to changes in the surrounding humidity since this might dynamically impact their water content. Water acts as a plasticizer for these polymers and the plasticizing effect induced by water can have a dramatic impact on the mechanical properties of these materials such as E, eb and TS. For this purpose, both 3D printed samples and the films were conditioned at three different environments, which led to three different water contents for the same material. In this context, the materials were conditioned for 24 h at a RH of 47 ± 3% and 15 ± 1%. The materials were also dried in an oven for 24 h at a temperature of 40°C. This way materials with three different water contents could be obtained.

Table 6.5 shows the mechanical properties of 3D printed and solvent cast dog bone shaped specimens obtained following the conditioning of the samples at a RH of 47 ± 3% for 24 h. For this RH, increasing the amount of HP in the blends increases the water content of both the 3D printed and solvent cast materials as expected since increasing KAc leads to increasing moisture absorption from the surroundings. This is also true for materials containing CC extracts since KOH can also be responsible for moisture absorption for the CC extracts. Conditioning at a RH of 47% gave materials with water content of 11.8% on average, which was 6.7% for materials 3D printed from pure PVA without any hemicellulose and lignin-based polymers. The

influence of water content on the mechanical properties of the 3D printed materials (PVA and HP/PVA blends) can be clearly seen in Figure A1 (in Appendix A). These figures clearly show that the water content strongly influences the mechanical properties of the samples. TS and E values of the samples were decreased with the increasing water content and the eb values of the samples were increased with the increasing of water content as expected. Figures 6.17, 6.18 and 6.19 show the TS, E, and eb of the samples (PVA and HP/PVA blends) as a function water content so that the influences of HP content on the mechanical properties of HP/PVA blends can be seen properly.

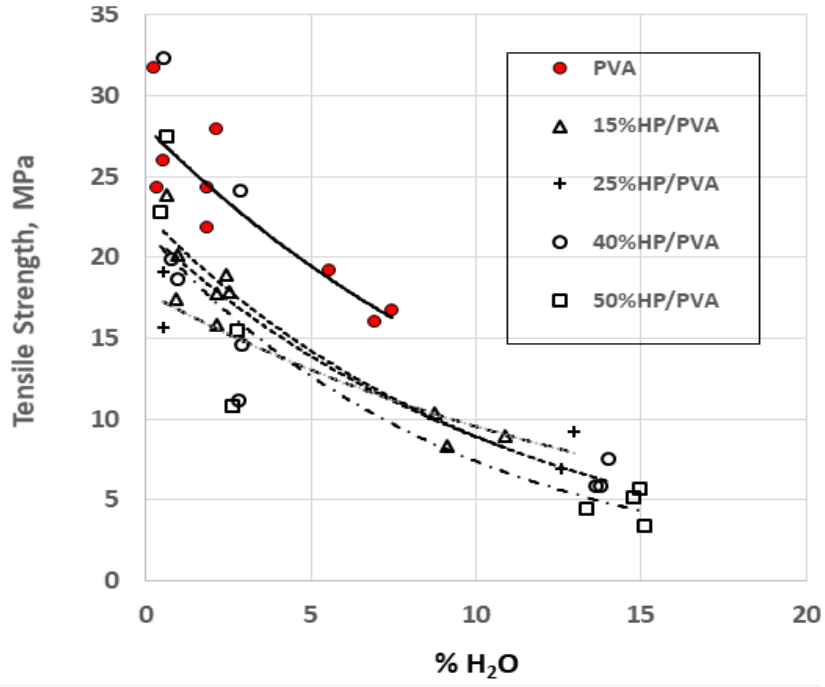


Figure 6.17 Tensile strength of 3D printed samples from PVA and HP/PVA blends with respect to different water contents. Lines represents power law fittings.

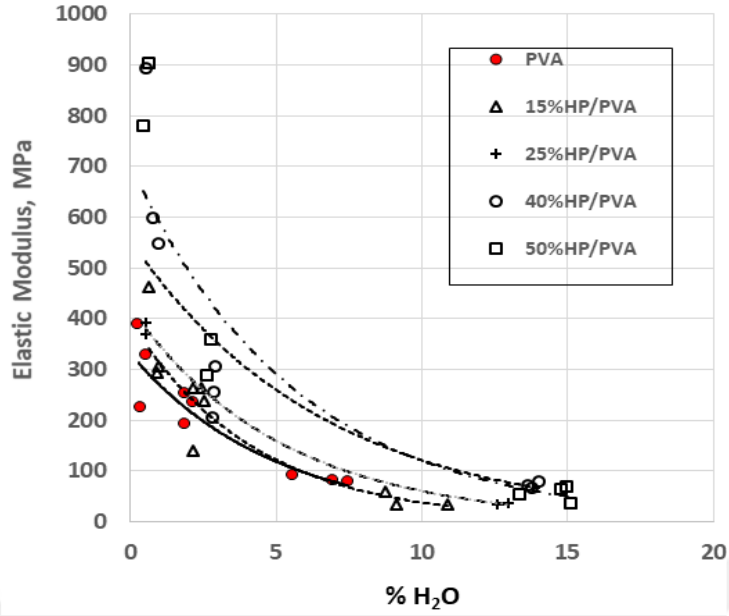


Figure 6.18 Elastic modulus of 3D printed samples from PVA and HP/PVA blends with respect to different water contents. Lines represents power law fittings.

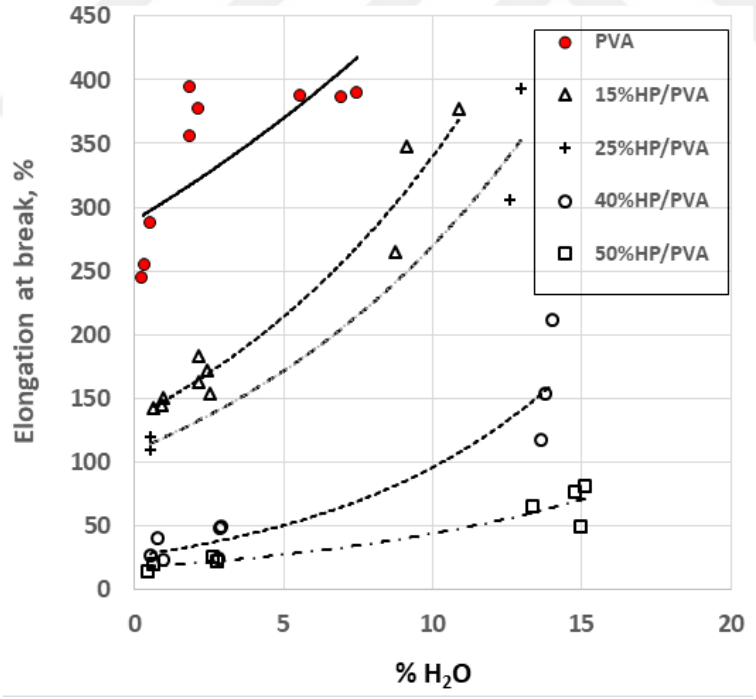


Figure 6.19 Elongation at break values of 3D printed samples from PVA and HP/PVA blends with respect to different water contents. Lines represents power law fittings.

As shown in Figure 6.17, the TS of the samples decreases with the addition of HP. However, no clear trend was observed for the TS of samples with different HP contents. Figure 6.18 suggests that the E of samples tends to increase with the addition of HP since the E of HP containing samples is higher than that of PVA (please see Tables 6.5 and 6.6).

The eb values of the samples is not only influenced by the water content but also by their HP content as shown in Figure 6.19. The eb values of the samples were reduced with the increasing of HP content since PVA is a much more ductile polymer compared to hemicellulose.

Desalting the HP prior to mixing it with PVA appears to have a major impact on the mechanical properties since KAc was removed from the sample. In addition to HP, CC extracts were also mixed with PVA, and the mechanical properties of these 3D printed materials were also determined. Materials containing CC extracts also had water contents greater than 10% since this time instead of KAc, KOH is found in these materials, which is also a highly moisture absorbing compound like KAc.

Figures 6.20, 6.21 and 6.22 compares the influence of adding different materials (HP, d-HP, and CC extract) to PVA on TS, E and eb, respectively.

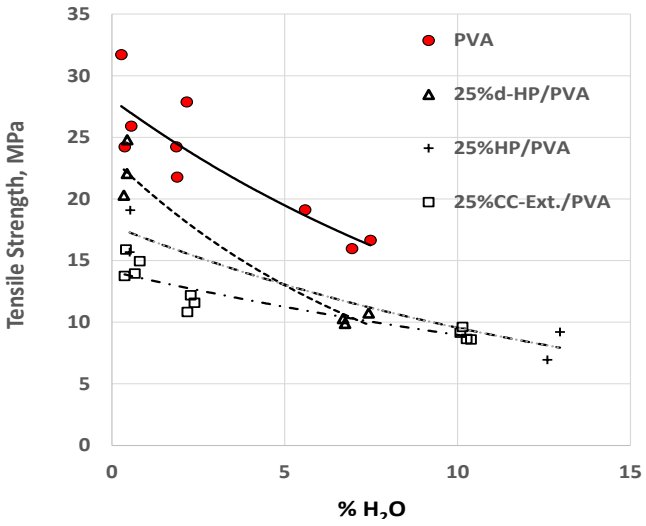


Figure 6.20 The tensile strength of PVA and HP/PVA blends with respect to different water contents.

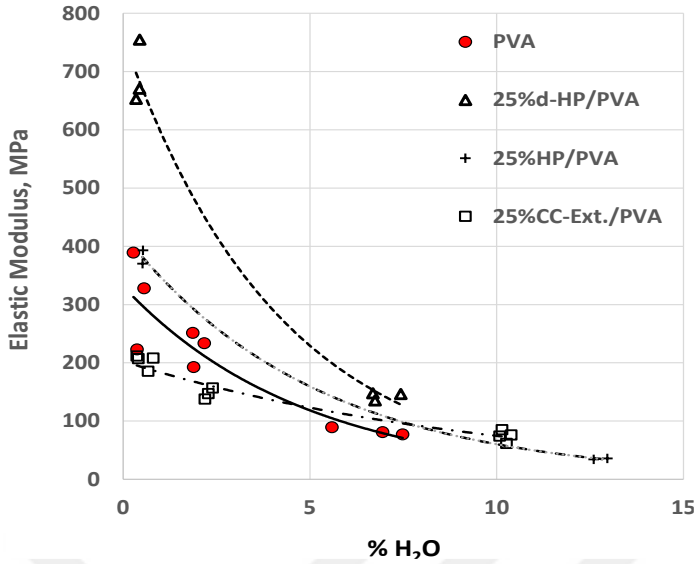


Figure 6.21 The elastic modulus of PVA and HP/PVA blends with respect to different water contents.

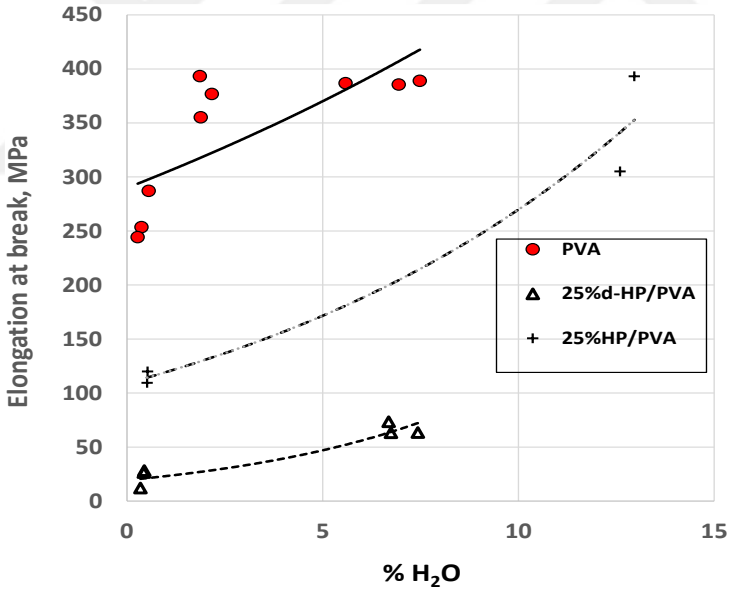


Figure 6.22 The elongation at break of PVA and HP/PVA blends with respect to different water contents.

The TS of the samples were reduced with the addition of HP, d-HP, and CC extract (Figure 6.20). Despite having a higher water content than the desalted 3D printed material 25% d-HP/PVA (10.2% vs. 7%), materials containing 25% CC extract had

similar mechanical properties compared to the materials containing 25% d-HP. A possible explanation here is the different compositions of the extract and the paste where the former contains significant amounts of lignin unlike the latter because as explained in the previous chapters of this study, there is no precipitation stage associated with obtaining extracts unlike the case with the pastes. Since there is no polymer precipitation at the end of the alkaline extraction process performed for obtaining the CC extracts, all the lignin solubilized in the alkaline medium finds its way into the 3D printed materials in this case, which leads to a different formulation compared to the pastes, which were obtained by the precipitation of the polymers solubilized in the alkaline medium with a solution of ethanol and acetic acid at the end of the extraction process. Increasing the concentration of the extract from 25% to 40% in the 3D printed materials leads to a dramatic increase in the water content of these materials from 10.2 to 14.9. This increase in water content reduces the TS while increasing the eb as expected (Table 6.5).

As shown in Figure 6.21, the highest E values were obtained for the d-HP/PVA blends since the d-HP/PVA samples do not contain KAc. KAc not only promotes water absorption but also acts as a plasticizer. As shown in Figure 6.22, the lowest eb values were obtained for the samples prepared with the addition of d-HP emphasizing the aforementioned observation.

Figures 6.17 - 6.22 enable a better understanding of the effect of conditioning environments (and thus the relevant water contents of the materials) on the mechanical properties of the materials in terms of E, TS, and eb. As discussed previously, it is clear that the relative humidity of the environment in which the 3D printed materials were conditioned has a huge impact on all the mechanical properties of the samples.

The results summarized in Table 6.5 suggest that when the eb values of the 3D printed and the solvent cast samples are compared, for the same formulation, the eb values of the 3D printed materials are almost always much higher than their solvent cast counter parts. The reason for this is obviously related to different processing

techniques, one of which relies on softening/melting the polymer and the other on solubilizing it. However, it is also worth mentioning that while 3D printing the dog bone shaped specimens, the lines that make up the layers in the model were printed in the parallel direction in which the load was going to be applied to the dog bone shaped samples during tensile testing. If the lines were printed in a perpendicular direction, totally different and likely inferior mechanical properties could be obtained.

Table 6.5 Mechanical properties of 3D printed, and solvent cast dog bone shaped specimens obtained following the conditioning of the samples at a RH of 47 ± 3%.

	Specimen id	*Elastic modulus (MPa)*	*Tensile strength (MPa)*	*Elongation at break (%)*	*Water content (%)*
3D Printed	PVA	82.6±6.3	17.3±1.7	387.2±1.8	6.7±1.0
	15% HP/PVA	43.5±11.0	9.0±1.0	327.7±48.0	9.5±1.0
	25% HP/PVA	35.0±1.2	8.1±1.6	349.2±62.2	12.8±0.3
	40% HP/PVA	72.4±5.3	6.4±1.0	160.7±47.6	13.8±0.2
	50% HP/PVA	56.5±14.6	4.7±1.0	68.3±14.1	14.5±0.8
	25% d-HP/PVA	143.2±6.8	10.3±0.4	66.7±5.8	7.0±0.4
	25% CC extract/PVA	74.4±9.6	9.0±0.5	67.3±9.1	10.2±0.1
	40 % CC extract/PVA	117.6±13.7	6.5±1.5	94.0±34.6	14.9±0.4
Solvent Cast	PVA	93.4±5.9	16.2±1.3	177.8±32.8	11.8±0.4
	Hemicellulose	689.9±112.5	15.7±2.4	14.0±2.3	10.9±1.4
	15% HP/PVA	103.1±10.8	9.1±1.3	70.7±29.1	6.6±0.1
	25% HP/PVA	86.4±9.1	7.7±0.3	68.2±12.4	7.9±0.6
	40% HP/PVA	64.9±5.9	5.3±0.3	29.1±0.1	10.7±0.2
	50% HP/PVA	205.8±27.2	10.8±1.3	33.9±1.9	9.5±0.7
	25% d-HP/PVA	363.4±19.0	15.3±0.6	38.9±7.5	6.2±0.1
	40% d-HP/PVA	292.2±29.5	6.6±1.0	5.4±1.1	6.2±0.2
	25% CC extract/PVA	88.2±1.3	9.2±0.4	166.8±14.9	8.6±0.5
	40% CC extract/PVA	60.2±9.1	3.9±0.5	27.3±2.4	11.1±0.4

Table 6.6 shows the mechanical test results obtained from samples, which were conditioned at 15% RH and eventually had much lower water contents than the previously discussed samples that were conditioned at 47% RH. As a result, the eb values of these samples with lower water contents are considerably lower but nevertheless they are still reasonable values. For example, the 3D printed 50% HP/PVA sample, which is the sample that had the highest biopolymer content overall, had a TS of 13.1 MPa and stiffness of 323.6 MPa, which were 3 and 6 times higher than the case in which the same material was conditioned at 47% RH to a water content of 14.5%, while also having a reasonable elongation of about 24%.

Unlike the case with conditioning at 47% RH, increasing the HP content for 3D printed samples does not cause any major changes in the E and TS values, which are around 250 MPa and 15 MPa, respectively. Increasing the HP content does increase the KAc content but this time there is not enough humidity in the surroundings to make a dramatic impact on the water content and thus on the mechanical properties of the materials since all HP containing 3D printed materials had similar water contents of around 2.5%. The eb, on the other hand, decreases but this is because of the reduction of PVA content as the HP in the formulation increases. As discussed previously and as it can also be seen from the solvent casting results given in Table 6.6, pure PVA based samples are much more ductile under these conditions as they were in the previous case since PVA samples elongate almost 25 times more compared to pure hemicellulosic polymer-based samples.

For the same formulation, 3D printed samples continue to display better elongation values compared to solvent casted ones just like the case with the higher water contents. As discussed earlier, this also suggests the importance of the processing method on the elongation at break values and also the importance of choosing the correct pattern during the 3D printing of the models.

Table 6.6 Mechanical properties of 3D printed, and solvent cast dog bone shaped specimens obtained following the conditioning of the samples at a RH of 15 ± 1%.

	Specimen id	*Elastic modulus (MPa)*	*Tensile strength (MPa)*	*Elongation at break (%)*	*Water content (%)*
3D Printed	PVA	225.90±30.07	24.63±3.07	375.13±19.11	2.0±0.2
	15% HP/PVA	225.83±58.95	17.63±1.27	167.93±12.46	2.3±0.2
	40% HP/PVA	256.27±49.70	16.64±6.71	40.22±14.09	2.9±0.05
	50% HP/PVA	323.60±51.05	13.13±3.32	23.79±2.62	2.7±0.08
	25% CC extract/PVA	147.27±9.45	11.53±0.68	165.97±14.70	2.3±0.1
Solvent Cast	PVA	374.87±55.24	26.28±2.58	162.43±7.03	3.8±0.3
	Hemicellulose	2134.00±233.71	47.19±6.53	6.58±2.78	1.5±0.9
	15% HP/PVA	387.70±17.66	19.33±1.23	95.90±27.53	2.7±0.2
	25% HP/PVA	331.97±40.00	18.97±3.14	59.40±11.03	1.5±0.04
	40% HP/PVA	227.35±27.84	13.80±3.05	47.77±9.70	3.0±0.6
	50% HP/PVA	813.63±238.36	21.29±7.61	13.26±7.69	3.4±0.5
	25% d-HP/PVA	1248.50±194.24	30.22±3.67	11.78±5.48	3.4±0.5
	40% d-HP/PVA	999.13±82.91	14.58±4.66	1.88±0.37	1.5±0.1
	25% CC extract/PVA	397.73±57.33	17.16±1.18	54.53±15.05	1.2±0.4
	40% CC extract/PVA	304.25±31.75	11.33±0.40	32.76±13.97	0.8±0.2

To further reduce the water content of the samples, samples were dried in an oven at 40°C for 24h. By doing so, the water contents of the samples were indeed further reduced to around 0.5% from 2.5% in the previous case. As shown in Table 6.6, both the stiffness and the TS values are further increased by the reduction in the water content while only a minor reduction was noted in the elongation values of the 3D printed samples. For example, the 3D printed sample 50% HP/PVA had E, TS and eb values of 842 MPa, 25.1 MPa and 17%, respectively for the current case while the same values were 324 MPa, 13 MPa and 24% for the case in which the samples were conditioned at 15% RH. This trend is also the same for the majority of other

samples showing that these materials perform better in term of their mechanical properties when they have the lowest water content possible, which can be obtained at very low RH conditions.

Different than the two previous cases that had higher water contents, increasing the amount of HP in the formulation of 3D printed samples appears to be beneficial in terms of increasing the stiffness. While the 3D printed samples from pure PVA had a stiffness of 313 MPa, this was increased to 680 MPa for 40% HP/PVA samples and further to 842 MPa for the 50% HP/PVA. These results were expected since under the same conditions for solvent cast samples, samples prepared from 100% hemicellulosic paste had a stiffness of 2555 MPa while samples from PVA alone had a stiffness of only 1190 MPa.

Just like the two previous cases with higher water contents, the eb values for 3D printed materials are again higher compared to their solvent cast counterparts, which can be regarded as an evidence of the role of processing conditions and printing patterns on elongation. As shown in Table 6.7 solvent cast and 3D printed samples had similar water contents following the drying period in the oven. Despite similar water contents, 3D printed samples still had much higher elongation values compared to solvent cast ones. For example, while the solvent cast 25% HP/PVA had an eb value of 44%, eb increases to 115% when the same formulation is processed with 3D printing. This trend is also similar for desalted sample. While solvent cast 25% d-HP/PVA had an %eb of 11, the %eb of the same polymer formulation increased to 22% when 3D printed.

Incorporation of CC extract instead of the paste generally leads to lower stiffness and TS values together with a higher eb values, at least when the concentration of the extract inside the blend is 25%. While the 3D printed 25% CC extract/PVA had E, TS and eb values of 203 MPa, 15 MPa and 173%, respectively, further increasing the CC extract concentration to 40% gave 3D printed samples with E, TS and eb values of 250 MPa, 12 MPa and 36% showing that CC extract concentration higher than 25% had an undesired effect on the mechanical properties unlike the pastes

where up to 50% hemicellulosic pastes could be pretty well tolerated in the 3D printed samples considering that increasing the paste content did not have any significant adverse effects on the mechanical properties of the 3D printed materials.

Table 6.7 Mechanical properties of 3D printed, and solvent cast dog bone shaped specimens obtained following the conditioning of the samples at in the oven at 40°C.

	Specimen id	*E (MPa)*	*TS (MPa)*	*eb (%)*	*Water content (%)*
3D Printed	PVA	313.40±83.99	27.29±3.93	261.77±22.51	0.4±0.1
	15% HP/PVA	354.47±94.61	20.50±3.24	145.87±3.94	0.8±0.2
	25% HP/PVA	381.70±16.12	17.39±2.40	114.70±7.50	0.5±0.01
	40% HP/PVA	679.63±186.63	23.65±7.53	29.94±8.98	0.8±0.2
	50% HP/PVA	842.00±88.53	25.13±3.28	16.94±3.77	0.6±0.2
	25% d-HP/PVA	692.73±54.30	22.39±2.27	22.25±8.85	0.4±0.05
	25% CC extract/PVA	203.25±11.94	14.64±0.99	173.63±18.12	0.6±0.2
	40% CC extract/PVA	250.30±77.62	11.50±3.30	35.58±8.30	1.1±0.1
Solvent Cast	PVA	1190.33±194.16	30.54±1.03	84.13±30.38	0.5±0.1
	Hemicellulose	2555.00±845.86	66.30±8.70	3.99±0.53	0.9±0.07
	15% HP/PVA	1125.67±63.44	26.77±1.03	32.41±8.41	0.5±0.2
	25% HP/PVA	899.53±361.62	25.70±4.96	43.57±18.51	0.4±0.09
	40% HP/PVA	780.75±250.72	22.56±4.17	29.36±7.99	0.5±0.04
	50% HP/PVA	994.23±546.43	27.16±12.58	8.46±1.82	0.9±0.09
	25% d-HP/PVA	1541.50±173.49	41.60±3.47	10.99±2.87	0.6±0.07
	40% d-HP/PVA	991.83±59.31	15.67±0.59	1.75±0.16	0.4±0.1
	25% CC extract/PVA	558.93±45.72	19.82±0.83	47.87±10.50	0.3±0.09
	40% CC extract/PVA	422.57±57.73	12.38±1.69	21.31±12.16	0.6±0.06

6.5 Thermogravimetric analysis of filaments with different formulations

Filaments that were used in 3D printing were also subjected to a thermogravimetric analysis to understand their thermal behaviors regarding their degradation profiles. As shown in Figure 6.23, there are two temperature regions in which major degradations take place and these follow a similar pattern to the weight loss profile of PVA as expected since all the samples contain at least 50% PVA and up to 85% PVA can be found in the samples depending on the formulation. The thermal degradation of PVA mostly involves a two-step-degradation (Peng and Kong, 2007). The first major degradation takes place over a relatively narrow temperature range compared to the second one where all the samples lost more than half of their original dry weight between approximately 220°C to 320°C. The degradation onset temperature for PVA in this initial degradation phase is 265°C and all other samples had lower degradation onset temperatures. This makes sense since as shown Figure 6.24, the degradation onset temperature of pure hemicellulose is at 228°C, which is around 40°C lower than that of PVA. All three types of filaments that contain HP, d-HP and CC extract have hemicellulose contents and the degradation onset temperatures for these samples are between 221°C to 237°C. In other words, mixing hemicellulose with PVA shifts the initial degradation onset to lower temperatures because of the lower thermal stability of hemicellulose compared to PVA. This trend is also the same for the second major weight loss region, which occurs between 370°C - 500°C for pure PVA filaments. Presence of hemicellulose in the blends also lowers the onset temperature for this region, however lignin also plays an important role here. As mentioned earlier lignin is a complex aromatic polymer with a much higher temperature stability compared to the polysaccharide polymer hemicellulose. As shown in Figure 6.24, most of the weight loss for lignin takes place between 300°C - 500°C, which intersects with the second weight loss region of PVA. Considering that all the samples excluding the pure PVA filament also contain lignin, weight loss due to the degradation of lignin and PVA intertwine, broadening the temperature range in which the second major weight loss takes place. In other words,

while the presence of hemicellulose shifts the onset temperature to lower values, presence of lignin broadens the second major weight loss region compared to filaments obtained from PVA alone. Another important effect due to the presence of lignin related to this region is on the weight retention of the filaments at this temperature range. There are major differences with respect to the remaining weight of the filament samples at 500°C and increased lignin content of the samples appears to be responsible for this difference. At this temperature, two samples with the highest lignin content among others including 50% HP/PVA and 40% CC extract/PVA have a much higher weight retention, which was around 33%. On the other hand, all other samples, which had lower lignin contents had a weight retention of around 25% at the same temperature while pure PVA filaments had a much lower weight retention of only 10%. The most likely reason for this different weight retention values is due to the fact that lignin is a highly thermally stable biopolymer, which is also used as a biopolymeric flame retardant in various polymer matrices (Chollet et al., 2019). The 1st derivative weight graphs with respect to temperature for filaments with different formulations are provided in Appendix B. In order to have an idea about the inorganic content of the filaments due to the presence of KAc in the pastes and KOH in the extracts, at the end of the TGA measurement at 900°C, nitrogen was evacuated from the test chamber and samples were treated at 900°C under ambient atmosphere in the presence of oxygen to measure the remaining weight under these conditions. Indeed, it was the 40% CC extract/PVA and the 50% HP/PVA samples, which were the filaments with the highest content of biopolymers and thus the inorganic contents, that had the highest remaining weight under these conditions. Under ambient atmosphere at 900°C, the remaining weight for 50% HP/PVA and 40% CC extract/PVA were 9.87% and 8.92%, respectively where this value was only 3.23% for the pure PVA filament.

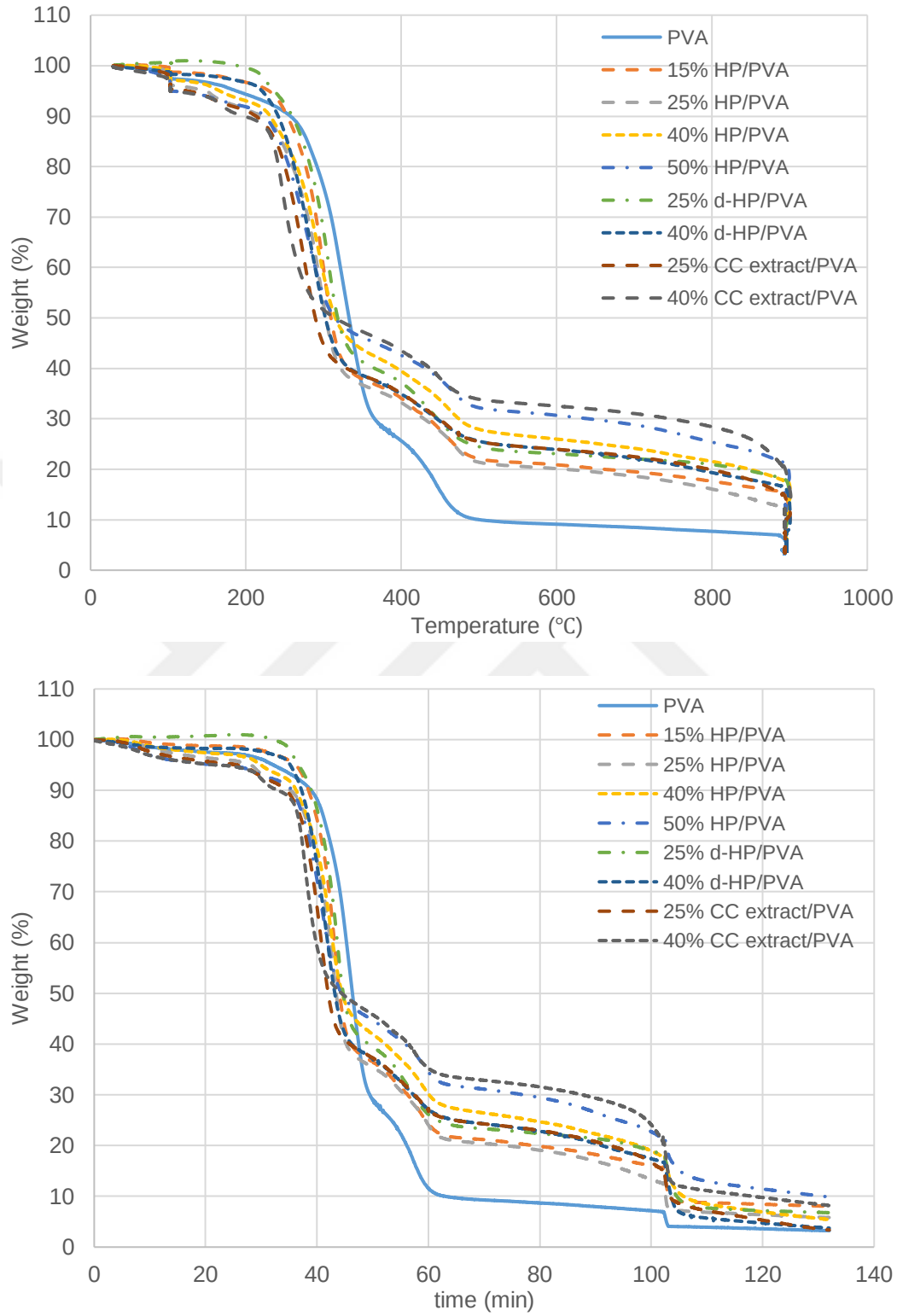


Figure 6.23 Thermograms with respect to temperature and time for filaments with different formulations.

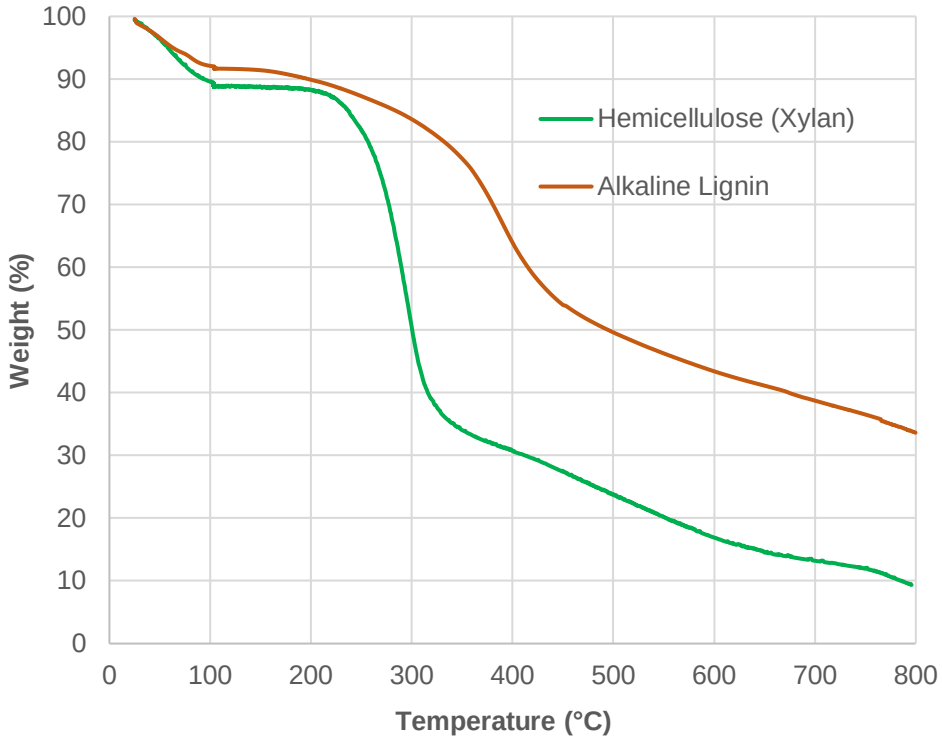


Figure 6.24 Thermograms for pure hemicellulose (xylan from birchwood) and alkali lignin.

CHAPTER 7

CONCLUSIONS

Three novel 3D printing strategies were developed for biopolymers extracted from a lignocellulosic agricultural waste, corn cob, by using hemicellulosic pastes, extracts containing lignin together with hemicellulose and filaments that contain PVA together with hemicellulose and lignin.

Conclusions on the 3D printing of pastes and extracts containing hemicellulose and lignin

3D printing of biopolymers based on hemicellulose, one of the most abundant biopolymers on earth after cellulose with a surprisingly low utilization despite its abundance, was made possible for the first time without applying any chemical modifications and without using any additives or auxiliary polymers. A formulation was developed for the hemicellulosic paste and the paste's water content together with its NaOH content was found to be the key for rendering lignocellulosic biomass based hemicellulosic pastes 3D printable when coupled to the correct 3D printing parameters. To achieve 3D printability, a large set of 3D printing parameters were studied in addition to the paste formulation including 10 different extrusion multipliers between 1.0 - 3.0, 5 different layer heights from 0.60 mm to 0.81 mm, 6 different printing speeds from 100 mm/min up to 4000 mm/min and 5 different 3D printing temperatures between 50°C - 90°C (in addition to room temperature). The best results were achieved with a water content of 65% at 80°C printing temperature with an extrusion multiplier of 1.5 at a printing speed of 1000 mm/min. Successful 3D printing of hemicellulosic pastes can only be achieved in a very narrow window regarding the paste formulation and 3D printing parameters since even the slightest changes in the water content of the pastes has a dramatic effect on the 3D printability of the polymers, which was shown to be related to the viscosity changes of the pastes

by complex and capillary viscometry measurements performed using parallel plate and capillary rheometers, respectively. Models printed with hemicellulosic pastes had sufficient printability values between 0.88 – 0.92 in addition to achieving 87% of the ideal cell area. A hollow cube consisting of 15 layers in addition to a flower (a daisy) shaped 3D model was printed to demonstrate that the models printed from hemicellulosic polymers could retain their integrity and withstand their own weight. The TS, %eb and E values for the dog-bone shaped specimens printed from the pastes were determined as 11 MPa, 7% and 545 MPa, respectively. A scaffold prototype was also printed from the hemicellulosic paste and the volume of the printed scaffold was found to decrease by 53% upon drying at ambient conditions due to the loss of some of its water content. Investigation of the 3D printed models by SEM revealed mostly a homogeneous cross-section while the presence of KAc salts was found at the surface of the specimens as verified by EDX, which was also in accordance with the FTIR spectrum of the hemicellulosic paste showing characteristic transmittance at wavenumbers specific to KAc.

Following the studies on the hemicellulosic paste, a procedure that enables for the first time the 3D printing of the entire alkaline soluble phase of a lignocellulosic biomass, which contain hemicellulose and lignin, was developed by using the alkaline extract in its crude for without any purification, chemical modification or additives. Compared to the paste-based approach, this procedure by-passes the polymer precipitation step, which involves successive steps such as using a solution of acetic acid and ethanol in addition to filtration. The extract obtained at the end of the alkaline extraction process was concentrated upon the evaporation of around 60% of its water content, which led to the formation of a gel upon cooling to room temperature. This thermoreversible cold-setting gel could be obtained at 5% KOH concentration during extraction and a lower KOH concentration of 3% did not lead to the formation of a gel, which was essential for the printing process since the cold-setting property of the gel enables it to retain the intended structure once the extract is deposited onto the build platform from the nozzle, cooling to room temperature. On the other hand, the thermoreversible property of the gel enables it to have the

desired flow when heated to mild temperatures around 45°C. This thermoreversible cold-setting property of the gel was further validated by complex viscosity measurements showing that the corn cob extract turns from a liquid like material (tan $\delta > 1$) to a solid like one (tan $\delta < 1$) based on the tan δ versus angular frequency curves obtained at different temperatures for different water contents. The most likely reason for this gelation might be the presence of arabinose groups attached to the xylan backbone, acting as structure breakers, and thus enabling the formation of multiple junction zones due to intermolecular hydrogen bonding. To optimize the process, corn cob extracts were printed with numerous parameters related not only to the corn cob extract formulation but also to the printing parameters. Changes as little as 5% in the water content of the extracts were found to dramatically impact their printability together with the changes in the printing temperature, providing a very narrow window that enables the successful printing of the corn cob extracts. The most ideal conditions for 3D printing the extracts were a water content of 83%, which was around 30% higher than the ideal water content of the hemicellulosic pastes, together with a printing temperature of 45-50°C, which was approximately 30°C lower compared to the ideal printing temperature of the pastes. FTIR spectrum of the corn cob extract indicates the presence of phenolic and aromatic groups related to lignin, which were mostly absent in the FTIR spectrum of the hemicellulosic pastes, showing that the paste and the extract had different lignin contents as expected. Printed models were immediately immersed in a bath containing a solution of acetic acid and ethanol based on the conventional alkaline extraction process, but it was found that the presence of acetic acid in the bath was detrimental for the printed models and only ethanol was sufficient to obtain the printed models in a rigid form. Dog bone shaped specimens printed from the extracts had TS, %eb and E values of 7 MPa, 1.6% and 654 MPa, respectively, showing that these models had lower TS and %eb values compared to those 3D printed from the hemicellulosic pastes. SEM images revealed a homogeneous cross-section for the printed models while crystal accumulation was detected at the surface, which was most likely KOH based on the presence of high amounts of potassium according to the EDX analysis.

Conclusions on the 3D printing of filaments containing PVA together with biopolymers extracted from corn cobs

In addition to the 3D printing of the pastes and gel extracts, a new blending approach that involves mixing the thermoplastic and water-soluble polymer PVA with the biopolymers extracted from corn cob was developed in order to obtain filaments, which were used for 3D printing of various models via thermoplastic extrusion. Solvent cast films based on PVA blended with either the hemicellulosic pastes or the extracts were obtained, and film pieces were processed with a capillary rheometer to obtain filaments. The ideal temperature range to obtain filaments from the PVA/biopolymer blends was determined as 170°C – 200°C depending on the biopolymer content of the blends also on whether the pastes or the extracts were being used. Eight different formulations were prepared and tested for their 3D printability including blends containing 15%, 25%, 40% and 50% hemicellulosic pastes, blends containing 25% and 40% desalted hemicellulosic pastes (KAc was removed) and blends containing 25% and 40% corn cob extracts. Presence of residual water in the blends was found to be detrimental for obtaining rigid filaments suitable for 3D printing and a heat treatment applied at 170°C for 20 minutes right before the filament fabrication was applied to solve this problem. All 4 printing temperatures tested, which were between 170°C - 200°C, gave models with a good visual appearance. An ideal printability value of 0.984 could be achieved together with a % target area value of 89% even when the content of hemicellulosic paste in the blend was as high as 50%. The effect of water content of the models, which had a major impact on the mechanical properties, were measured by conditioning the 3D printed dog bone shaped samples at three different environments. For the models containing the highest amount of biopolymers obtained from corn cobs together with PVA, which were the samples that contained 50% hemicellulosic paste, reducing the water content from around 3% to 1% led to a dramatic increase in elastic modulus from 324 MPa to 842 MPa while also increasing the TS by around 2 fold from 13 MPa to 25 MPa showing even very small changes in the water content of these material have huge impacts on the mechanical properties. Increasing the water

content from around 3% to 15% for the same material led to an increased plasticization resulting to an increase in the %eb value from 24% to 68% while reducing the TS from 13 MPa to 5 MPa. The reduction in stiffness was the most dramatic one with increasing water content for the same case since it was reduced by almost 6-fold from 324 MPa to 57 MPa following the increase in the water content from 3% to 15%. Other formulations also displayed similar trends with the changing water content in terms of their mechanical properties. Based on the TGA results, blends having 40% extract or 50% paste in their formulation have higher weight retention at 500°C compared to other samples most likely due to the presence of higher amounts of lignin in these samples, which is a complex polymer with high temperature stability. On the other hand, compared to filament obtained from PVA only, all the biopolymer containing filaments have lower initial degradation onset temperatures because of the presence of hemicellulose since compared to PVA, initial degradation onset temperature for hemicellulose is around 40°C lower. In addition to grid models, more complex shapes compared to those printed from the pastes and the gel extract, could be 3D printed with this strategy such as a polyhedron. Considering that up to 50% hemicellulosic paste can be utilized together with PVA, it can be considered that hemicellulosic polymers can be used in the formulation of support materials during the 3D printing of complex shapes to replace some of the PVA with a renewable bio-based alternative.

CHAPTER 8

FUTURE STUDIES

Regarding the future studies that can be performed related to the work presented here, a promising approach would be developing wound dressings and scaffolds for medical applications. In this context, the first step would be to perform cytotoxicity assays to the biopolymers (hemicellulose and lignin) and to the materials 3D printed from the polymers. Some formulations might have to be altered based on the results of these cytotoxicity assays. Another important study related to these applications should include drug release experiments. Some model compounds to simulate the drugs and some active pharmaceutical ingredients can be loaded to the printed materials either before the printing process (by including the compounds in the pastes or the extracts) or after the printing process by the absorption of the compounds to the printed materials in a liquid medium with a specific concentration of the active compound. An important advantage here might be the relatively low 3D printing temperature, which is especially valid for the extracts since this could enable the inclusion of heat sensitive substances to the printing formulation. By changing the die design of the extruder in the 3D printer, core/shell filaments enabling the 3D printing of channel structures can be obtained.

In addition to PVA, hemicellulose and lignin-based polymers extracted from corn cobs or other types of lignocellulosic biomass can also be blended with other polymers including engineering thermoplastics. Compatibilizers might be needed in this case and alternative blending methods such as extrusion would be required to blend the biopolymers with the synthetic ones. If successful blending of biopolymers with synthetic polymers such as polyamide, ABS and polycarbonate could be achieved, this approach could then be used to produce various components such as automotive and aviation parts and household appliances, among many others.

REFERENCES

Äkräs, L. (2019). 3D bioprinting inks based on cellulose nanofibrils and colloidal lignin particles. Chemical, Biochemical and Materials Engineering, Aalto University, Master's Thesis.

Anderson, C., & Simsek, S. (2018). What are the characteristics of arabinoxylan gels?. Food and Nutrition Sciences, 9(07), 818.

Aruldass, S., Mathivanan, V., Mohamed, A. R., & Tye, C. T. (2019). Factors affecting hydrolysis of polyvinyl acetate to polyvinyl alcohol. Journal of Environmental Chemical Engineering, 7(5), 103238.

Bahcegul, E., Akinalan, B., Toraman, H. E., Erdemir, D., Ozkan, N., & Bakir, U. (2013). Extrusion of xylans extracted from CCs into biodegradable polymeric materials. Bioresource technology, 149, 582-585.

Bahcegul, E., Toraman, H. E., Erdemir, D., Akinalan, B., Ozkan, N., & Bakir, U. (2014). An unconventional approach for improving the integrity and mechanical properties of xylan type hemicellulose based films. RSC Advances, 4(64), 34117-34126.

Béguin, P., & Aubert, J. P. (1994). The biological degradation of cellulose. FEMS microbiology reviews, 13(1), 25-58.

Bezzi, F., Fabbri, P., Magnani, G., Salernitano, E., Scafè, M., & Strafella, A. (2022). Aqueous aluminium titanate paste for the liquid deposition modelling. Open Ceramics, 9, 100224.

Bian, J., Peng, F., Peng, X. P., Xu, F., Sun, R. C., & Kennedy, J. F. (2012). Isolation of hemicelluloses from sugarcane bagasse at different temperatures: structure and properties. Carbohydrate polymers, 88(2), 638-645.

Boeriu, C. G., Bravo, D., Gosselink, R. J., & van Dam, J. E. (2004). Characterisation of structure-dependent functional properties of lignin with infrared spectroscopy. Industrial crops and products, 20(2), 205-218.

Busse-Wicher, M., Gomes, T. C., Tryfona, T., Nikolovski, N., Stott, K., Grantham, N. J., ... & Dupree, P. (2014). The pattern of xylan acetylation suggests xylan may interact with cellulose microfibrils as a twofold helical screw in the secondary plant cell wall of Arabidopsis thaliana. The Plant Journal, 79(3), 492-506.

Chai, X., Chai, H., Wang, X., Yang, J., Li, J., Zhao, Y., ... & Xiang, X. (2017). Fused deposition modeling (FDM) 3D printed tablets for intragastric floating delivery of domperidone. Scientific reports, 7(1), 2829.

Chen, H. (2014). Chemical composition and structure of natural lignocellulose. In Biotechnology of lignocellulose (pp. 25-71). Springer, Dordrecht.

Chen, Z., Li, Z., Li, J., Liu, C., Lao, C., Fu, Y., ... & He, Y. (2019). 3D printing of ceramics: A review. Journal of the European Ceramic Society, 39(4), 661-687.

Chinga-Carrasco, G. (2018). Potential and limitations of nanocelluloses as components in biocomposite inks for three-dimensional bioprinting and for biomedical devices. Biomacromolecules, 19(3), 701-711.

Chinga-Carrasco, G., Yu, Y., & Diserud, O. (2011). Quantitative electron microscopy of cellulose nanofibril structures from Eucalyptus and Pinus radiata kraft pulp fibers. Microscopy and microanalysis, 17(4), 563-571.

Chollet, B., Lopez-Cuesta, J. M., Laoutid, F., & Ferry, L. (2019). Lignin nanoparticles as a promising way for enhancing lignin flame retardant effect in polylactide. Materials, 12(13), 2132.

Chundawat, S. P., Beckham, G. T., Himmel, M. E., & Dale, B. E. (2011). Deconstruction of lignocellulosic biomass to fuels and chemicals. Annu Rev Chem Biomol Eng, 2(1), 121-145.

Cui, S. W. (2005). Food carbohydrates: chemistry, physical properties, and applications. CRC press.

Das, A., Gilmer, E. L., Biria, S., & Bortner, M. J. (2021). Importance of polymer rheology on material extrusion additive manufacturing: Correlating process physics to print properties. ACS Applied Polymer Materials, 3(3), 1218-1249.

de Vries, R. P., & Visser, J. A. A. P. (2001). Aspergillus enzymes involved in degradation of plant cell wall polysaccharides. Microbiology and molecular biology reviews, 65(4), 497-522.

Domínguez-Robles, J., Martin, N. K., Fong, M. L., Stewart, S. A., Irwin, N. J., Rial-Hermida, M. I., ... & Larrañeta, E. (2019). Antioxidant PLA composites containing lignin for 3D printing applications: a potential material for healthcare applications. Pharmaceutics, 11(4), 165.

Ebers, L. S., & Laborie, M. P. (2020). Direct ink writing of fully bio-based liquid crystalline lignin/hydroxypropyl cellulose aqueous inks: optimization of formulations and printing parameters. ACS Applied Bio Materials, 3(10), 6897-6907.

Ecker, J. V., Haider, A., Burzic, I., Huber, A., Eder, G., & Hild, S. (2019). Mechanical properties and water absorption behaviour of PLA and PLA/wood composites prepared by 3D printing and injection moulding. Rapid Prototyping Journal, 25(4), 672-678.

Feng, X., Yang, Z., Chmely, S., Wang, Q., Wang, S., & Xie, Y. (2017). Lignin-coated cellulose nanocrystal filled methacrylate composites prepared via 3D stereolithography printing: Mechanical reinforcement and thermal stabilization. Carbohydrate polymers, 169, 272-281

Fincher, G. B., & Stone, B. A. (1986). Cell walls and their components in cereal grain technology. Advances in cereal science and technology, 8, 207-295.

Fukuzumi, H., Saito, T., & Isogai, A. (2013). Influence of TEMPO-oxidized cellulose nanofibril length on film properties. Carbohydrate Polymers, 93(1), 172-177.

Gibson, L. J. (2012). The hierarchical structure and mechanics of plant materials. Journal of the royal society interface, 9(76), 2749-2766.

Giummarella, N., Pu, Y., Ragauskas, A. J., & Lawoko, M. (2019). A critical review on the analysis of lignin carbohydrate bonds. Green Chemistry, 21(7), 1573-1595.

Gkartzou, E., Koumoulos, E. P., & Charitidis, C. A. (2017). Production and 3D printing processing of bio-based thermoplastic filament. Manufacturing Review, 4, 1.

Gleuwitz, F. R., Sivasankarapillai, G., Siqueira, G., Friedrich, C., & Laborie, M. P. G. (2020). Lignin in bio-based liquid crystalline network material with potential for direct ink writing. ACS Applied Bio Materials, 3(9), 6049-6058.

Gu, X., Ma, X., Li, L., Liu, C., Cheng, K., & Li, Z. (2013). Pyrolysis of poplar wood sawdust by TG-FTIR and Py–GC/MS. Journal of Analytical and Applied Pyrolysis, 102, 16-23.

Henke, K., & Treml, S. (2013). Wood based bulk material in 3D printing processes for applications in construction. European Journal of Wood and Wood Products, 71(1), 139-141.

Henke, K., Talke, D., Bunzel, F., Buschmann, B., & Asshoff, C. (2021). Individual layer fabrication (ILF): A novel approach to additive manufacturing by the use of wood. European Journal of Wood and Wood Products, 79(3), 745-748.

Hofmann, M. (2014). 3D printing gets a boost and opportunities with polymer materials. ACS Macro Letters, 3, 4, 382–386

Hong, S. H., Park, J. H., Kim, O. Y., & Hwang, S. H. (2021). Preparation of chemically modified lignin-reinforced PLA biocomposites and their 3D printing performance. Polymers, 13(4), 667.

https://formlabs.com/blog/3d-printing-materials/, last visited on July 2022. Guide to 3D Printing Materials: Types, Applications, and Properties.

https://webbook.nist.gov/. NIST Chemistry WebBook, last visited on May 2021.

https://www.3dhubs.com/blog/fully-functional-3dprinted-jet-engine-built-by-students-to-create-next-level-in aerospace/, last visited on October 2018

https://www.3dhubs.com/knowledge-base/additive-manufacturing-process, last visited on October 2018 What is additive manufacturing? Get started with 3D printing.

https://www.3dhubs.com/materialindex#?page=1&sortby=popularity&order=des, last visited on October 2018

https://www.3dprintingmedia.network/additive-manufacturing/am-technologies/what-is-liquid-deposition-modeling/, last visited on June 2022

https://www.alma.edu/ddsc/resources/technology/3d-printing/the-3d-printing-process.php, last visited on July 2022. The 3D Printing Process

https://www.core77.com/posts/71172/How-to-Select-the-Right-DPrintingProcess, last visited on October 2018 How to Select the Right 3D Printing Process.

https://www.rsc.org/suppdata/ra/c2/c2ra20916k/c2ra20916k.pdf, last visited on April 2022. Electronic Supplementary Material (ESI) for RSC Advances.

https://www.techbriefs.com/component/content/article/tb/pub/features/articles/33589, last visited on July 2022 3D Printing: The Impact of Post-Processing

Hua, W., Liu, C., Wu, S. B., & Li, X. H. (2016). Analysis of structural units and their influence on thermal degradation of alkali lignins. BioResources, 11(1), 1959-1970.

Ibrahim, F., Mohan, D., Sajab, M. S., Bakarudin, S. B., & Kaco, H. (2019). Evaluation of the compatibility of organosolv lignin-graphene nanoplatelets with photo-curable polyurethane in stereolithography 3D printing. Polymers, 11(10), 1544.

Jeffries, T. W. (1994). Biodegradation of lignin and hemicelluloses. Biochemistry of microbial degradation, 233-277.

Ji, A., Zhang, S., Bhagia, S., Yoo, C. G., & Ragauskas, A. J. (2020). 3D printing of biomass-derived composites: application and characterization approaches. RSC advances, 10(37), 21698-21723.

Jiang, B., Yao, Y., Liang, Z., Gao, J., Chen, G., Xia, Q., ... & Hu, L. (2020). Lignin-Based Direct Ink Printed Structural Scaffolds. Small, 16(31), 1907212.

Kam, D., Chasnitsky, M., Nowogrodski, C., Braslavsky, I., Abitbol, T., Magdassi, S., & Shoseyov, O. (2019). Direct CRYO writing of aerogels via 3D Printing of aligned cellulose nanocrystals inspired by the plant cell wall. Colloids and Interfaces, 3(2), 46.

Kam, D., Layani, M., BarkaiMinerbi, S., Orbaum, D., Abrahami BenHarush, S., Shoseyov, O., & Magdassi, S. (2019). Additive manufacturing of 3D structures composed of wood materials. Advanced Materials Technologies, 4(9), 1900158.

Kariz, M., Sernek, M., & Kuzman, M. K. (2016). Use of wood powder and adhesive as a mixture for 3D printing. European journal of wood and wood products, 74(1), 123-126.

Kariz, M., Sernek, M., & Kuzman, M. K. (2018). Effect of humidity on 3D-printed specimens from wood-PLA filaments. Wood Res, 63(5), 917-922.

Kariz, M., Sernek, M., Obućina, M., & Kuzman, M. K. (2018). Effect of wood content in FDM filament on properties of 3D printed parts. Materials Today Communications, 14, 135-140.

Kearns, A., Farahbakhsh, N., Venditti, R., & Jur, J. (2016). Cotton fibers in 3d printing. In Solid Freeform Fabrication 2016: Proceedings of the 26th annual international solid freeform fabrication symposium—an additive manufacturing conference(pp. 899-905).

Kim, J. S., Lee, Y. Y., & Kim, T. H. (2016). A review on alkaline pretreatment technology for bioconversion of lignocellulosic biomass. Bioresource Technology, 199, 42-48.

Kiszonas, A. M., Fuerst, E. P., & Morris, C. F. (2013). Wheat arabinoxylan structure provides insight into function. Cereal Chemistry, 90(4), 387-395.

Le Duigou, A., Castro, M., Bevan, R., & Martin, N. (2016). 3D printing of wood fibre biocomposites: From mechanical to actuation functionality. Materials & Design, 96, 106-114.

Li, J., Wu, C., Chu, P. K., & Gelinsky, M. (2020). 3D printing of hydrogels: Rational design strategies and emerging biomedical applications. Materials Science and Engineering: R: Reports, 140, 100543.

Ligon, S. C., Liska, R., Stampfl, J., Gurr, M., & Mülhaupt, R. (2017). Polymers for 3D printing and customized additive manufacturing. Chemical reviews, 117(15), 10212-10290.

Liu, L., Lin, M., Xu, Z., & Lin, M. (2019). Polylactic acid-based wood-plastic 3D printing composite and its properties. BioResources, 14(4), 8484-8498.

Liu, Z., Bhandari, B., Prakash, S., Mantihal, S., & Zhang, M. (2019). Linking rheology and printability of a multicomponent gel system of carrageenan-xanthan-starch in extrusion based additive manufacturing. Food hydrocolloids, 87, 413-424.

Maitan-Alfenas, G. P., Visser, E. M., & Guimarães, V. M. (2015). Enzymatic hydrolysis of lignocellulosic biomass: converting food waste in valuable products. Current Opinion in Food Science, 1, 44-49.

Marcia, M. D. O. (2009). Feruloylation in grasses: current and future perspectives. Molecular plant, 2(5), 861-872.

Markstedt, K., Escalante, A., Toriz, G., & Gatenholm, P. (2017). Biomimetic inks based on cellulose nanofibrils and cross-linkable xylans for 3D printing. ACS applied materials & interfaces, 9(46), 40878-40886.

Markstedt, K., Håkansson, K., Toriz, G., & Gatenholm, P. (2019). Materials from trees assembled by 3D printing–Wood tissue beyond nature limits. Applied Materials Today, 15, 280-285.

Marriott, P. E., Gómez, L. D., & McQueen-Mason, S. J. (2016). Unlocking the potential of lignocellulosic biomass through plant science. New phytologist, 209(4), 1366-1381.

McMillan, J. D. (1997). Bioethanol production: status and prospects. Renewable energy, 10(2-3), 295-302.

Mimini, V., Sykacek, E., Syed Hashim, S. N. A., Holzweber, J., Hettegger, H., Fackler, K., ... & Rosenau, T. (2019). Compatibility of kraft lignin, organosolv lignin and lignosulfonate with PLA in 3D printing. Journal of Wood Chemistry and Technology, 39(1), 14-30.

Moberg, T., Sahlin, K., Yao, K., Geng, S., Westman, G., Zhou, Q., ... & Rigdahl, M. (2017). Rheological properties of nanocellulose suspensions: effects of fibril/particle dimensions and surface characteristics. Cellulose, 24(6), 2499-2510.

Moghaddam, L., Rencoret, J., Maliger, V. R., Rackemann, D. W., Harrison, M. D., Gutiérrez, A., ... & Doherty, W. O. (2017). Structural characteristics of bagasse furfural residue and its lignin component. An NMR, Py-GC/MS, and FTIR study. ACS Sustainable Chemistry & Engineering, 5(6), 4846-4855.

Mohan, D., Bakir, A. N., Sajab, M. S., Bakarudin, S. B., Mansor, N. N., Roslan, R., & Kaco, H. (2021). Homogeneous distribution of lignin/graphene fillers with enhanced interlayer adhesion for 3D printing filament. Polymer Composites, 42(5), 2408-2421.

Morales-Burgos, A. M., Carvajal-Millan, E., López-Franco, Y. L., Rascón-Chu, A., Lizardi-Mendoza, J., Sotelo-Cruz, N., ... & Pedroza-Montero, M. (2017). Syneresis in gels of highly ferulated arabinoxylans: characterization of covalent cross-linking, rheology, and microstructure. Polymers, 9(5), 164.

Negi, S., Dhiman, S., & Sharma, R. K. (2013). Basics, applications and future of additive manufacturing technologies: A review. Journal of Manufacturing Technology Research, 5(1/2), 75.

Nguyen, N. A., Bowland, C. C., & Naskar, A. K. (2018). Mechanical, thermal, morphological, and rheological characteristics of high performance 3D-printing lignin-based composites for additive manufacturing applications. Data in brief, 19, 936-950.

Niño-Medina, G., Carvajal-Millán, E., Lizardi, J., Rascon-Chu, A., Marquez-Escalante, J. A., Gardea, A., ... & Guerrero, V. (2009). Maize processing waste water arabinoxylans: Gelling capability and cross-linking content. Food Chemistry, 115(4), 1286-1290.

Okolie, J. A., Nanda, S., Dalai, A. K., & Kozinski, J. A. (2021). Chemistry and specialty industrial applications of lignocellulosic biomass. Waste and Biomass Valorization, 12(5), 2145-2169.

Ouyang, L., Highley, C. B., Rodell, C. B., Sun, W., & Burdick, J. A. (2016). 3D printing of shear-thinning hyaluronic acid hydrogels with secondary cross-linking. ACS Biomaterials Science & Engineering, 2(10), 1743-1751.

Paxton, N., Smolan, W., Böck, T., Melchels, F., Groll, J., & Jungst, T. (2017). Proposal to assess printability of bioinks for extrusion-based bioprinting and evaluation of rheological properties governing bioprintability. Biofabrication, 9(4), 044107.

Peng, Z., & Kong, L. X. (2007). A thermal degradation mechanism of polyvinyl alcohol/silica nanocomposites. Polymer Degradation and Stability, 92(6), 1061-1071.

Perez, A. R. T., Roberson, D. A., & Wicker, R. B. (2014). Fracture surface analysis of 3Dprinted tensile specimens of novel ABS-based materials. Journal of Failure Analysis and Prevention, 14(3), 343-353.

Pérez, J., Munoz-Dorado, J., De la Rubia, T. D. L. R., & Martinez, J. (2002). Biodegradation and biological treatments of cellulose, hemicellulose and lignin: an overview. International microbiology, 5(2), 53-63.

Popescu, C. M., Popescu, M. C., Singurel, G., Vasile, C., Argyropoulos, D. S., & Willfor, S. (2007). Spectral characterization of eucalyptus wood. Applied spectroscopy, 61(11), 1168-1177.

Postiglione, G., Natale, G., Griffini, G., Levi, M., & Turri, S. (2015). Conductive 3D microstructures by direct 3D printing of polymer/carbon nanotube nanocomposites via liquid deposition modeling. Composites Part A: Applied Science and Manufacturing, 76, 110-114.

Pratima, B. (2016). Pretreatment of Lignocellulosic Biomass for Biofuel Production. India, Springer Nature Press.

Priya, M. S., Naresh, K., Jayaganthan, R., & Velmurugan, R. (2019). A comparative study between in-house 3D printed and injection molded ABS and PLA polymers for low-frequency applications. Materials Research Express, 6(8), 085345.

Rashid, T., Kait, C. F., & Murugesan, T. (2016). A "Fourier Transformed infrared" compound study of lignin recovered from a formic acid process. Procedia engineering, 148, 1312-1319.

Rosenthal, M., Henneberger, C., Gutkes, A., & Bues, C. T. (2018). Liquid Deposition Modeling: A promising approach for 3D printing of wood. European journal of wood and wood products, 76(2), 797-799.

Saadi, M. A. S. R., Maguire, A., Pottackal, N. T., Thakur, M. S. H., Ikram, M. M., Hart, A. J., ... & Rahman, M. M. (2022). Direct Ink Writing: A 3D Printing Technology for Diverse Materials. Advanced Materials, 2108855.

Saha, D., & Bhattacharya, S. (2010). Hydrocolloids as thickening and gelling agents in food: a critical review. Journal of food science and technology, 47(6), 587-597.

Sammons, R. J., Harper, D. P., Labbé, N., Bozell, J. J., Elder, T., & Rials, T. G. (2013). Characterization of organosolv lignins using thermal and FT-IR spectroscopic analysis. BioResources 8 (2): 2752-2767, 8(2), 2752-2767.

Sathitsuksanoh, N., Zhu, Z., Templeton, N., Rollin, J. A., Harvey, S. P., & Zhang, Y. P. (2009). Saccharification of a potential bioenergy crop, Phragmites australis (common reed), by lignocellulose fractionation followed by enzymatic hydrolysis at decreased cellulase loadings. Industrial & Engineering Chemistry Research, 48(13), 6441-6447

Sharma, A., Nain, V., Tiwari, R., Singh, S., Adak, A., Nain, P. K. S., & Nain, L. (2017). Simultaneous saccharification and fermentation of alkali-pretreated corncob under optimized conditions using cold-tolerant indigenous holocellulase. Korean Journal of Chemical Engineering, 34(3), 773-780.

Shavandi, A., Hosseini, S., Okoro, O. V., Nie, L., Eghbali Babadi, F., & Melchels, F. (2020). 3D bioprinting of lignocellulosic biomaterials. Advanced Healthcare Materials, 9(24), 2001472.

Sim, S. F., Mohamed, M., Lu, N. A. L. M. I., Sarman, N. S. P., & Samsudin, S. N. S. (2012). Computer-assisted analysis of fourier transform infrared (FTIR) spectra for characterization of various treated and untreated agriculture biomass. BioResources, 7(4), 5367-5380.

Sinha, A. K., Kumar, V., Makkar, H. P., De Boeck, G., & Becker, K. (2011). Non-starch polysaccharides and their role in fish nutrition–A review. Food Chemistry, 127(4), 1409-1426.

Sørensen, H. R., Pedersen, S., & Meyer, A. S. (2007). Characterization of solubilized arabinoxylo-oligosaccharides by MALDI-TOF MS analysis to unravel and direct enzyme catalyzed hydrolysis of insoluble wheat arabinoxylan. Enzyme and Microbial Technology, 41(1-2), 103-110.

Spyropoulos, F., Lazidis, A., & Norton, I. (Eds.). (2019). Handbook of Food Structure Development. Royal Society of Chemistry.

Sun, X. F., Sun, R., Fowler, P., & Baird, M. S. (2005). Extraction and characterization of original lignin and hemicelluloses from wheat straw. Journal of Agricultural and Food Chemistry, 53(4), 860-870.

Sutton, J. T., Rajan, K., Harper, D. P., & Chmely, S. C. (2018). Lignin-containing photoactive resins for 3D printing by stereolithography. ACS applied materials & interfaces, 10(42), 36456-36463.

Tanase-Opedal, M., Espinosa, E., Rodríguez, A., & Chinga-Carrasco, G. (2019). Lignin: A biopolymer from forestry biomass for biocomposites and 3D printing. Materials, 12(18), 3006.

Tarasov, D., Leitch, M., & Fatehi, P. (2018). Lignin–carbohydrate complexes: properties, applications, analyses, and methods of extraction: a review. Biotechnology for biofuels, 11(1), 1-28.

Torre, P., Aliakbarian, B., Rivas, B., Domínguez, J. M., & Converti, A. (2008). Release of ferulic acid from corn cobs by alkaline hydrolysis. Biochemical Engineering Journal, 40(3), 500-506.

Vaidya, A. A., Collet, C., Gaugler, M., & Lloyd-Jones, G. (2019). Integrating softwood biorefinery lignin into polyhydroxybutyrate composites and application in 3D printing. Materials Today Communications, 19, 286-296.

Valent, B. S., & Albersheim, P. (1974). The structure of plant cell walls: V. On the binding of xyloglucan to cellulose fibers. Plant Physiology, 54(1), 105-108.

Vorndran, E., Moseke, C., & Gbureck, U. (2015). 3D printing of ceramic implants. Mrs Bulletin, 40(2), 127-136.

Wang, Q., Sun, J., Yao, Q., Ji, C., Liu, J., & Zhu, Q. (2018). 3D printing with cellulose materials. Cellulose, 25(8), 4275-4301.

Wang, S., Wang, K., Liu, Q., Gu, Y., Luo, Z., Cen, K., & Fransson, T. (2009). Comparison of the pyrolysis behavior of lignins from different tree species. Biotechnology Advances, 27(5), 562-3.

Wang, X., Jiang, M., Zhou, Z., Gou, J., & Hui, D. (2017). 3D printing of polymer matrix composites: A review and prospective. Composites Part B: Engineering, 110, 442-458.

Wang, Z., Xu, J., Lu, Y., Hu, L., Fan, Y., Ma, J., & Zhou, X. (2017). Preparation of 3D printable micro/nanocellulose-polylactic acid (MNC/PLA) composite wire rods with high MNC constitution. Industrial crops and products, 109, 889-896.

Wasti, S., Triggs, E., Farag, R., Auad, M., Adhikari, S., Bajwa, D., ... & Ragauskas, A. J. (2021). Influence of plasticizers on thermal and mechanical properties of biocomposite filaments made from lignin and polylactic acid for 3D printing. Composites Part B: Engineering, 205, 108483.

Xiao, B., Sun, X., & Sun, R. (2001). Chemical, structural, and thermal characterizations of alkali-soluble lignins and hemicelluloses, and cellulose from maize stems, rye straw, and rice straw. Polymer degradation and stability, 74(2), 307-319.

Xie, G., Zhang, Y., & Lin, W. (2017). Plasticizer combinations and performance of wood flour–poly (lactic acid) 3D printing filaments. BioResources, 12(3), 6736-6748.

Xu, F., Yu, J., Tesso, T., Dowell, F., & Wang, D. (2013). Qualitative and quantitative analysis of lignocellulosic biomass using infrared techniques: a mini-review. Applied energy, 104, 801-809.

Xu, W., Pranovich, A., Uppstu, P., Wang, X., Kronlund, D., Hemming, J., ... & Xu, C. (2018). Novel biorenewable composite of wood polysaccharide and polylactic acid for three dimensional printing. Carbohydrate polymers, 187, 51-58.

Xu, W., Zhang, X., Yang, P., Långvik, O., Wang, X., Zhang, Y., ... & Xu, C. (2019). Surface engineered biomimetic inks based on UV cross-linkable wood biopolymers for 3D printing. ACS applied materials & interfaces, 11(13), 12389-12400.

Yao, J., Odelius, K., & Hakkarainen, M. (2021). Microwave Hydrophobized Lignin with Antioxidant Activity for Fused Filament Fabrication. ACS Applied Polymer Materials, 3(7), 3538-3548.

Zander, N. E., Park, J. H., Boelter, Z. R., & Gillan, M. A. (2019). Recycled cellulose polypropylene composite feedstocks for material extrusion additive manufacturing. ACS omega, 4(9), 13879-13888.

Zhang, B., Cristescu, R., Chrisey, D. B., & Narayan, R. J. (2020). Solvent-based Extrusion 3D Printing for the Fabrication of Tissue Engineering Scaffolds. International Journal of Bioprinting, 6(1).

Zhang, S., Li, M., Hao, N., & Ragauskas, A. J. (2019). Stereolithography 3D printing of lignin-reinforced composites with enhanced mechanical properties. ACS omega, 4(23), 20197-20204.

Zhang, X., Morits, M., Jonkergouw, C., Ora, A., Valle-Delgado, J. J., Farooq, M., ... & Österberg, M. (2020). Three-dimensional printed cell culture model based on spherical colloidal lignin particles and cellulose nanofibril-alginate hydrogel. Biomacromolecules, 21(5), 1875-1885.

Zhao, X., Tekinalp, H., Meng, X., Ker, D., Benson, B., Pu, Y., ... & Ozcan, S. (2019). Poplar as biofiber reinforcement in composites for large-scale 3D printing. ACS Applied Bio Materials, 2(10), 4557-4570.

Zhou, G., Taylor, G., & Polle, A. (2011). FTIR-ATR-based prediction and modelling of lignin and energy contents reveals independent intra-specific variation of these traits in bioenergy poplars. Plant methods, 7(1), 1-10.

Zhou, L. Y., Fu, J., & He, Y. (2020). A review of 3D printing technologies for soft polymer materials. Advanced Functional Materials, 30(28), 2000187.

Zilliox, C., & Debeire, P. (1998). Hydrolysis of wheat straw by a thermostable endoxylanase: adsorption and kinetic studies. Enzyme and Microbial technology, 22(1), 58-63.

Zoghlami, A., & Paës, G. (2019). Lignocellulosic biomass: understanding recalcitrance and predicting hydrolysis. Frontiers in chemistry, 7, 874.

APPENDICES

A. Mechanical properties of 3D printed HP/PVA, d-HP/PVA and CC extract/PVA blends

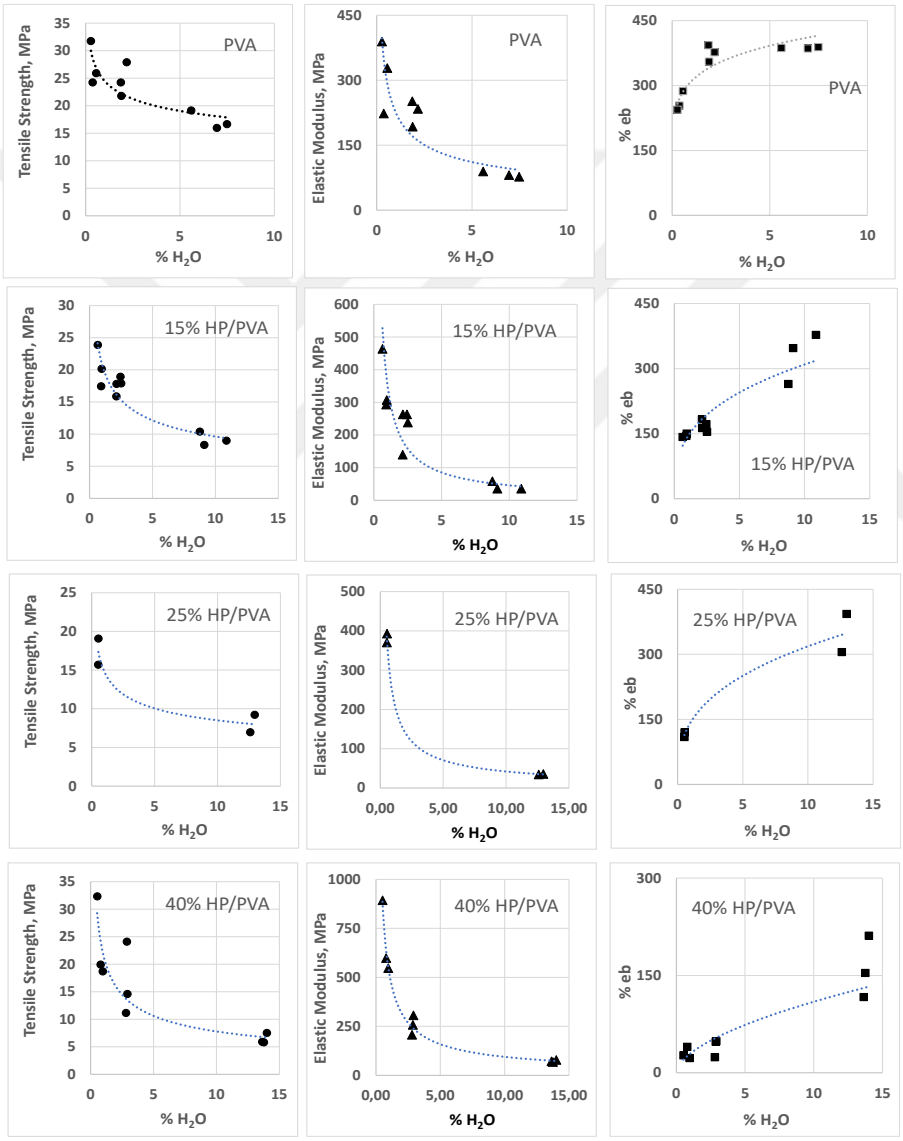


Figure A1 Mechanical properties of 3D printed samples from PVA, 15% HP/PVA, 25% HP/PVA, 40% HP/PVA at various water contents.

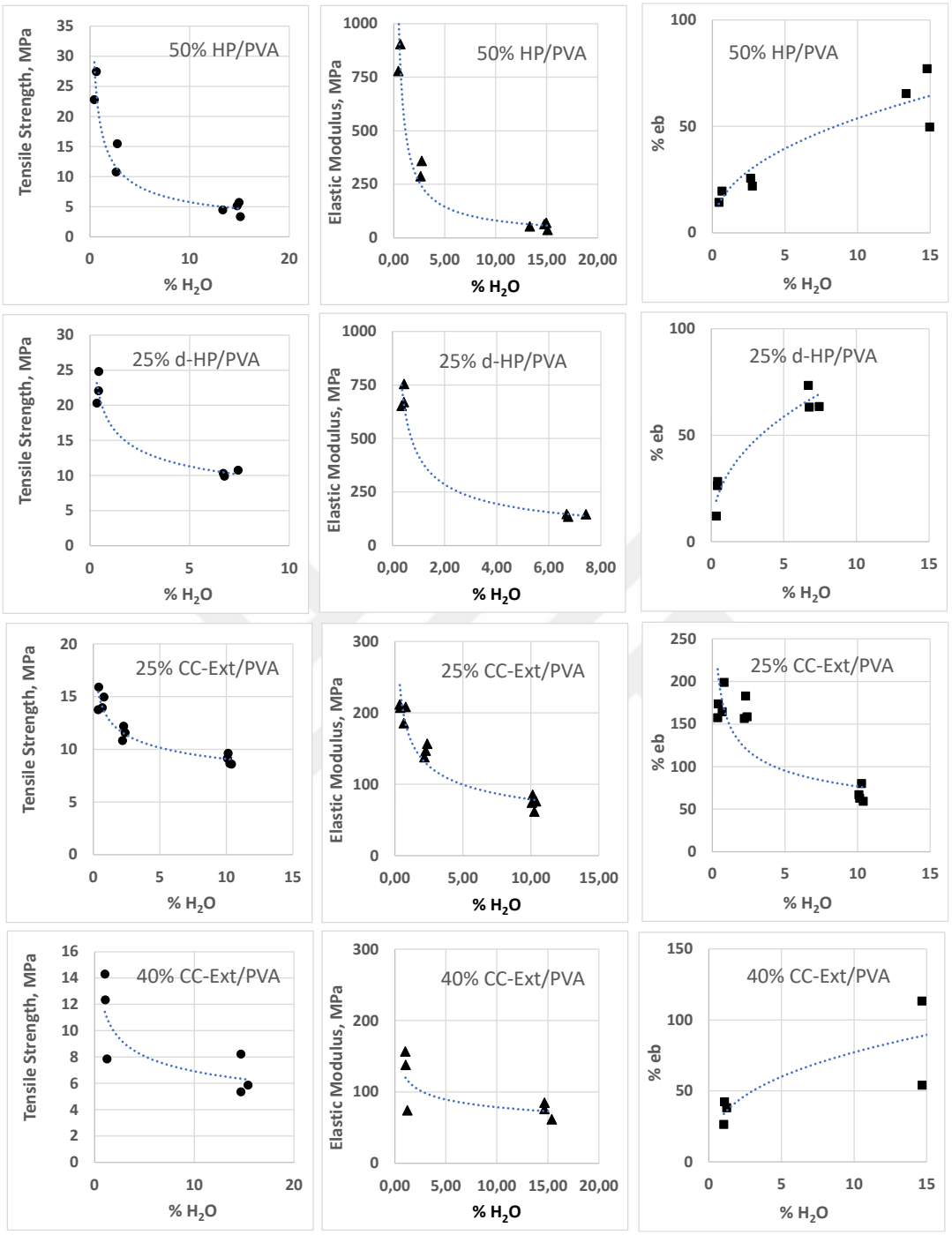


Figure A1 (continued) Mechanical properties of 3D printed samples from 50% HP/PVA, 25% d-HP/PVA, 25% CC extract/PVA, 40% CC extract/PVA at various water contents.

B. 1st derivative weight graphs for filaments with different formulations

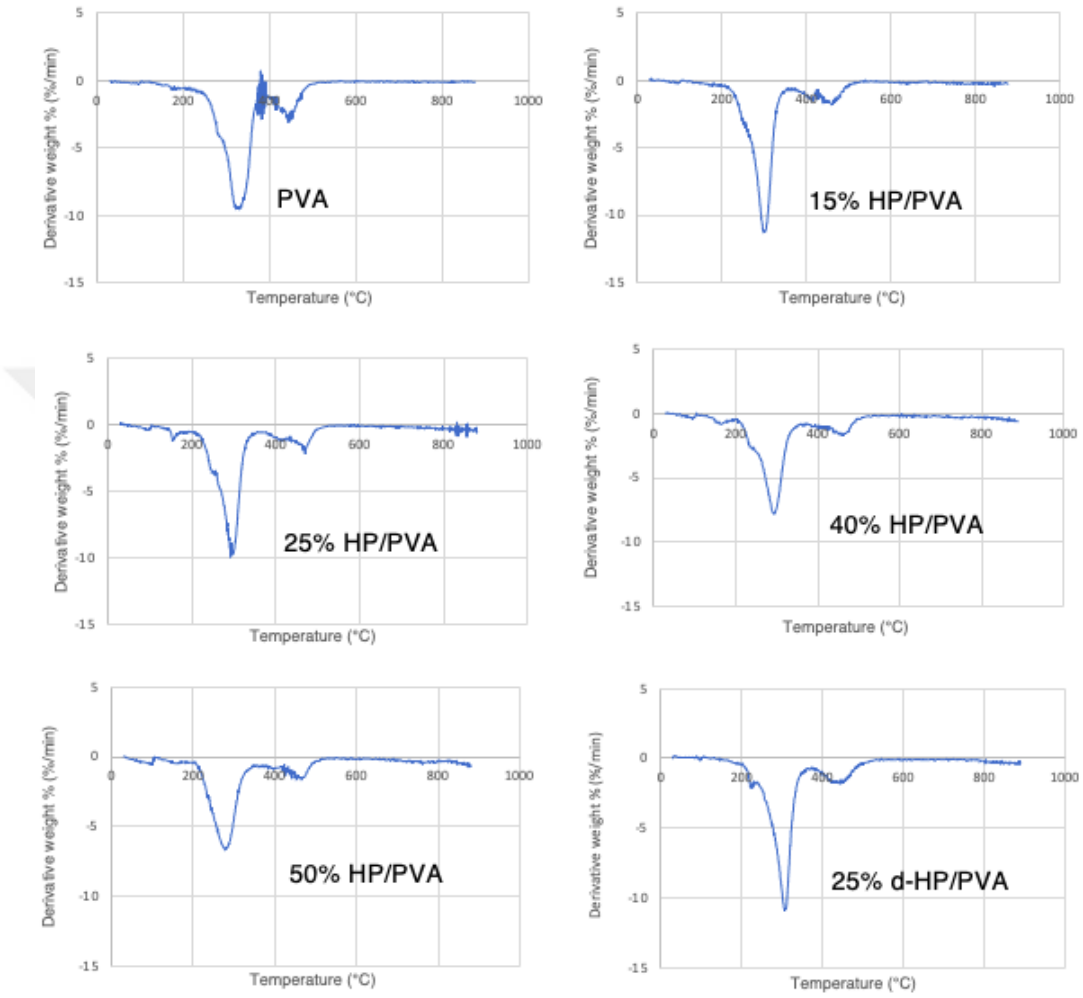


Figure B1 1st derivative weight graphs with respect to temperature for filaments with different formulations.

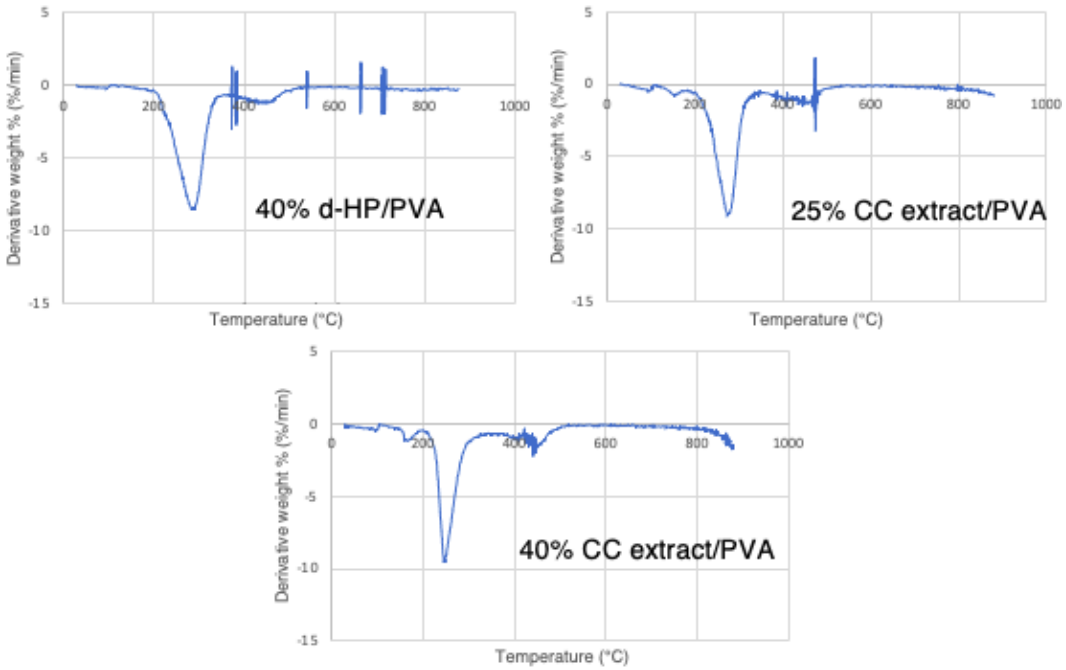


Figure B1 (continued) 1st derivative weight graphs with respect to temperature for filaments with different formulations.

CURRICULUM VITAE

Surname, Name: Bahçegül, E. Gökçe

EDUCATION

Degree	Institution	Year of Graduation
MS	METU Chemical Engineering	2014
BS	METU NCC Chemical Engineering	2011

FOREIGN LANGUAGES

Advanced English

PUBLICATIONS

1. Bahcegul, E. G., Bahcegul, E., & Ozkan, N. (2020). 3D printing of hemicellulosic biopolymers extracted from lignocellulosic agricultural wastes. ACS Applied Polymer Materials, 2(7), 2622-2632.

2. Bahcegul, E. G., Bahcegul, E., & Ozkan, N. (2022). 3D printing of crude lignocellulosic biomass extracts containing hemicellulose and lignin. Industrial Crops and Products, 186, 115234.